이학박사 학위논문

Controlled Synthesis and Biosensing, Bioimaging and Therapeutic Applications of Plasmonic Nano-Bio Hybrid Probes

(플라즈모닉 나노-바이오 하이브리드 프로브의 합성 조절,

바이오센싱, 바이오이미징 및 치료에의 응용)

2014 년 8 월

서울대학교 대학원

화학부 무기화학

Sumit Kumar

Controlled Synthesis and Biosensing, Bioimaging and Therapeutic Applications of Plasmonic Nano-Bio Hybrid Probes

(플라즈모닉 나노-바이오 하이브리드 프로브의 합성 조절, 바이오센싱, 바이오이미징 및 치료에의 응용)

지도교수 남 좌 민

이 논문을 이학박사 학위논문으로 제출함

2014 년 8 월

서울대학교 대학원

화학부 무기화학

Sumit Kumar

수밋 쿠마르 의 박사학위논문을 인준함

2014 년 8 월

위 원 장 이진규 (인)

부 위 원 장 남좌민 (인)

위 원 오문현 (인)

위 원 김지환 (인)

위 원 이연 (인)

Abstract

Controlled Synthesis and Biosensing, Bioimaging and Therapeutic Applications of Plasmonic Nano-Bio Hybrid Probes

Sumit kumar

Department of Chemistry

The Graduate School

Seoul National University

Nanomaterials-based diagnostic and therapeutic platforms have offered significant advantages over conventional systems with regard to high sensitivity, selectivity and low cost. Among various nanomaterials, gold nanoparticles (AuNPs) possess a plethora of unique features such as size- and shape-dependent optical and electronic properties, a high surface area to volume ratio, and versatile surface-chemistry readily modifiable with ligands (including biomolecules) containing a variety of functional groups; and therefore such plasmonic nanostructures have established a centerstage amongst diverse scientific communities involving chemists, physicists, biologists and material scientists. Intelligent design and synthesis of plasmonic nanostructures and their hybrids is crucial to tune their localized surface plasmon resonance (LSPR)-

based properties such as optical signaling, surface-enhanced-Raman scattering (SERS), photocatalysis and photothermal transduction, useful in biomedical applications. In spite of the proliferative growth of nanoscience in last two decades, potential real-life applications of biosensing/bioimaging/therapeutic plasmonic nanoprobes in biological systems suffer several design challenges to address the important issues such as biocompatibility (no toxicity), efficient nano-bio interfacing, sensitive signaling response and benign but effective therapeutic action.

In the present thesis, we have designed and synthesized new plasmonic nanostructures/nanoassemblies which show tunable optical, SERS, enzymetic, photothermal and photocatalytic properties. We successfully demonstrated that our new nano-bio hybrid probes have potential to distinguish normal and cancer cells based on their sensitive, selective and quantitative monitoring/imaging of cellular oxidative and nitrosative stress in living cells (by optical and SERS based signaling), biodetection of glucose with clinical urinalysis trial (colorimetric/UV-Vis signaling), and organic photosensitizer-free bimodal photothermal and photodynamic therapeutic effect for cancer cells destruction.

Reactive oxygen species (ROS) and reactive nitrogen species (RNS) are chemically reactive intermediates naturally produced in the living systems as the consequence of complex endogenous and exogenous biochemical reactions. Overproduction of ROS/RNS, so-called 'the state of oxidative-stress' is a hallmark for the pathogenesis of many diseases such as cardiovascular diseases, cancer, and neurodegenerative diseases. In chapter 1, we developed a straightforward, sensitive, and quantitative assay for the colorimetric and spectroscopic detection of various ROS and RNS such as H_2O_2, ·OH, $^{-}$OCl, NO,

and O_2^- using glutathione-modified gold nanoparticles (GSH-AuNPs). A basic principle here is that the GSHs on the AuNP surface can be readily detached via the formation of glutathione disulfides upon the addition of ROS and RNS, and destabilized particles can aggregate to generate the plasmonic couplings between plasmonic AuNPs that trigger the red shift in UV–vis spectrum and solution color change. For nonradical species such as H_2O_2, this process can be more efficiently achieved by converting them into radical species via the Fenton reaction. Using this strategy, we were able to rapidly and quantitatively distinguish among cancerous and normal cells based on ROS and RNS production.

Simultaneous and distinguishable quantitative monitoring of ROS and RNS in living cells is important for understanding their independent and interdependent biological roles; eventually useful in solving bio-signalling mechanistic puzzles. In chapter 2, we design a plasmonic 'core-satellite' nanoassembly bioprobe for SERS-based distinguishable multiplex quantitative monitoring of H_2O_2 and NO in living cells. We have strategically conjugated myoglobin as the dual-responsive Raman reporter in the electromagnetic 'hot-zones' of gold core-satellite nanoassemblies with the help of biocompatible polydopamine interface/spacer. ROS/RNS detection principle is based on the structural changes in Raman reporter heme prosthetic group of SERS bioprobe, distinctly and quantitatively monitored in living normal and cancer cells by SERS measurements upon reaction with intracellular H_2O_2 and NO.

Metal nanostructures with highly branched morphologies are an interesting and useful new class of nanomaterials due to their plasmonically enhanced optical properties, large surface area and potential as catalytic substrates, sensing probes and building blocks for nanoscale devices. In

particular, surface plasmon-derived photo-induced therapeutic effect and catalysis are highly dependent on their surface nanostructures, but the control of their branching structures is challenging. In chapter 3, we introduce a strategy for the controlled synthesis of plasmonic core-petal nanostructures (CPNs) with highly branched morphologies. The fine nanostructural engineering of CPNs was facilitated by gold chloride-induced oxidative disassembly of polydopamine corona around spherical Au nanoparticles and successive anisotropic growth of Au nanopetals. We show that CPNs can act as multifunctional nanoreactors that induce photodynamic and photothermal dual therapeutic effects and generate ROS. Near-infrared laser-activated CPNs can be used to induce the effective destruction of cancer cells via the synergistic combination of benign plasmonic hyperthermia (~42 °C) and ROS-mediated oxidative intracellular damage. It was also shown that CPNs exhibit very strong surface-enhanced Raman scattering signals, and this allows for post-mortem probing of ROS-mediated oxidative structural modifications of DNA that could be responsible for the apoptotic fate of cancer cells.

Hybrid nanobiosensors working on enzyme-mimetic mechanisms are always desired to amalgamate best features of natural and synthetic systems. In chapter 4, we report a hybridized three component enzyme-mimetic glutathione-Au@Pt core-shell nanoprobe for recognition and colorimetric signaling of glucose. Unlike conventional glucose sensors based on natural enzymes, our nanoprobe is robust enough to operate in a wide pH range and even at high temperatures. In the biomimetic design, nanopockets present between Au core and porous Pt shell interfaced with glutathione ligand provide an optimal hydrophobic and hydrogen bonding environment for the efficient recognition of host sugar molecule as suggested from NMR spectroscopy and DFT calculations. GSH-Au@Pt catalyzes efficient oxidation of glucose to

corresponding gluconic acids and co-produced H_2O_2 triggers dimerization of interfacial glutathione ligands resulting aggregation-induced plasmonic coupling between Au cores, exhibiting a visual colour change. Finally, clinical test with urine samples collected from diabetic patients were performed with very high degree of accuracy and almost no sensitivity towards common interfering urine ingredients such as ascorbic acid, proteins and cysteine.

Keywords: Plasmonic sensors, Colorimetric sensors, Surface-enhanced Raman Scattering, Bioimaging, Biosensing, Reactive oxygen species, reactive nitrogen species, oxidative stress, Cancer diagnosis, Core-shell, Enzyme-mimetic, Photothermal therapy, Photodynamic Therapy, Core-satellites, Plasmonic Assembly, Branched Nanostructure, Polydopamine, Glutathione, Glucose detection, Urinalysis test.

Student Number: 2008-31095

Contents

List of Figures and Scheme.

Chapter 1.

Figure 1.6. ESI-MS spectra of a) aggregated AuNPs with GSSGs (in H_2O) and b) GSH-AuNPs (in H_2O)

Figure 1.7. ^1H NMR (500 MHz) spectra of a) aggregated AuNPs with GSSGs (in D_2O) and b) GSH-AuNPs (in D_2O).

Figure 1.8. (a) Plots of reaction kinetics for change in ΔA_{525} as a function of (a) ROS/RNS concentration upon the treatment with the GSH-AuNPs for 2 h or (b) reaction progress (min) for various ROS/RNS at a constant concentration (1.29 mM) upon the reaction with the GSH-AuNPs.

Figure 1.9. The zeta potentials and hydrodynamic radii of the GSH-AuNPs at 25 °C and 37 °C, respectively

Figure 1.10. Comparison of GSH-AuNPs with other thiolated ligands for H_2O_2 detection: (a) The chemical structures of non-GSH thiolated ligands; (b) ΔA_{525} values for differently functionalized AuNPs upon the treatment with 12.9 mM H_2O_2.

Figure 1.11. The corresponding UV-Vis Absorption spectra of GSH-AuNPs solution after addition of 12.9 mM various type of ROS including H_2O_2, $^{\cdot}OH$, ^{-}OCl, NO and O_2^{-}.

Figure 1.12. GSH-AuNPs with cells. (a) The GSH-AuNP probes are internalized into both normal and cancerous cells. Up taken probes were characterized by the TEM after cell fixation. (b) The cell viability results obtained using the Cell Counting Kit after 2-day incubation with varying concentrations of GSH-AuNP probes. The error bars represent the standard deviations based on three independent measurements.

Figure 2.5. Comparison of characteristic Raman peaks of Mb with and without the use of pdop spacer.

Figure 2.6. (a) Schematic representation for expected structural changes in heme group present in core-satellite nanoprobe upon reaction with H_2O_2 and NO. (b-c) Raman spectra obtained after exposure of core-satellite nanoprobe with different concentrations of H_2O_2 and NO. (d) Plots of changes in intensities of Raman peaks at 1386 cm^{-1} and 596 cm^{-1} after exposing core-satellite nanoprobes with different concentrations of H_2O_2, NO and their equimolar mixtures. (e) Plots of changes in intensities of Raman peaks at 1386 cm^{-1} and 596 cm^{-1} after exposing core-satellite nanoprobes with H_2O_2, NO and their equimolar mixtures at different times.

Figure 2.7. UV/Vis spectra of Mb-core satellite nanoprobe before and after addition of H_2O_2 and NO.

Figure 2.8. TEM image of core satellite structures without pdop.

Figure 2.9. Core-satellite nanoprobes with cells. (a) TEM images of normal and cancer cells after core-satellite nanoprobe internalization followed by cell fixation. (b) Schematic for estimation of gold amount by ICP-AES after core-satellite internalization. (c) % cellular uptake of core-satellite nanoprobes calculated from ICP-AES data for all cells. (d) Cell viability results for all four different cells obtained using the cell counting kit after 2-day incubation with varying concentrations of core-satellite AuNP probes. The error bars represent the standard deviations based on three independent measurements.

Figure 2.10. a) Schematic representation for ROS/RNS monitoring using core-satellite nanoprobes. b) dark-field image, bright-field image, Raman mapping image corresponding to the band at 1386 cm^{-1} for ROS measurement and Raman mapping image corresponding to the band at 596 cm^{-1} for RNS

measurement in normal and cancer cells (left to right). c) Change in Raman intensities at 1386 cm^{-1} and 596 cm^{-1} for normal and cancerous cells. d) Contour Raman maps corresponding to bands at 1386 and 596 cm^{-1} as the representation of total amount of ROS and RNS in normal and cancerous cells.

Figure 2.11. Total ROS/RNS estimated from commercial assay in different cell lines before and after experiment

Chapter 3.

Figure 3.1. (a) Schematic representation for oxidative nanopeeling chemistry of pdop for the synthesis of CPN. (b) TEM image of pdop-AuNPs (80 nm core) with ~5 nm pdop coating. (c) SEM image of CPNs. (d) TEM image of CPNs. (e) Dark-field microscopy image of pdop-AuNPs. (f) Dark-field microscopy image of CPNs. (g) Comparison of scattering intensities and color spectrum obtained from CPNs and pdop-AuNPs. (h) UV/Vis spectra of AuNPs, pdop-AuNPs, CPN-1, CPN-2, CPN-3, CPN-4. (i) TEM images of AuNP, CPN-1, CPN-2, CPN-3, CPN-4 (from left to right).

Figure 3.2. The XPS analysis of pdop-AuNPs (80-nm core). (a) The XPS survey spectrum of pdop-AuNPs. (b) The deconvoluted high resolution C 1s peak. (c) The deconvoluted high resolution O 1s peak. (d) High resolution N 1s peak. (e) Comparison between Au 4f peaks in pdop-AuNPs and citrate-AuNPs.

Figure 3.3. Raman spectra (514 nm laser, 10 mW laser power) of pdop-AuNPs before (lower spectrum) and after (upper spectrum) $HAuCl_4$ treatment.

Figure 3.4. ^{13}C NMR (400 MHz in D_2O) of pdop-AuNPs before (lower spectrum) and after (upper spectrum) $HAuCl_4$ treatment.

Figure 3.5. (a) Schematic representation of laser-induced photothermal effect and ROS production in CPN. (b) Rise in temperature as the function of laser irradiation time for different gold nanoprobes. (c) Rise in temperature as the function of laser power for different gold nanoprobes. (d) Studies on reproducible photothermal performance of different gold nanoprobes in three successive cycle. (e) Increase in temperature as the function of time for different concentration of CPN-4. (f) Change in the absorbance of RNO molecules with respect to laser irradiation time as the measurement of laser-induced $^1O_2$ production for different Au nanoprobe aqueous solutions. (g) Change in the absorbance of RNO molecules with respect to laser power as the measurement of effect of laser power on $^1O_2$ production for different Au nanoprobe.

Figure 3.6. Luminescence spectra of CPN-4 solution in D_2O after laser irradiation (in black) and after N_2 gas purging (in red).

Figure 3.7. (a) Dark-field microscopy image of untreated HeLa cells. (b) Dark-field microscopy image of HeLa cells treated with CPN-4 particles. (c) Low (i) and high (ii) magnification TEM image of a section of fixed HeLa cell treated with CPN-4 probes, showing CPN-4 particles encapsulated in endosome. (d) Results of HeLa cell viability assay after treating with different amounts of CPN-4 probes under dark conditions. (e) Quantification of cell death upon PDT-PTT treatment of HeLa cells treated with AuNPs, CPN-1, CPN-2, CPN-3, CPN-4, in the presence and absence of laser irradiation. (f) Overlapped fluorescence images obtained from Live/dead cell assay of HeLa cells treated with AuNPs, CPN-1, CPN-2, CPN-3 and CPN-4. The green and red dots indicate healthy cells and dead cells, respectively.

Figure 3.8. Rise in temperature of cell-culture medium as the function of laser irradiation time for CPN-4 nanoprobes.

Figure 3.9. Dark-field microscopy image of healthy HeLa cell treated with CPN-4 particles (inset TEM image showing intact cellular membrane). (b) Dark-field microscopy image of dead HeLa cells treated with CPN-4 followed by PDT-PTT treatment (inset TEM image showing damaged cellular membrane). (c) Fluorescence intensities recorded from HeLa cell lysates after PDT-PTT treatment using AuNPs, CPN-1, CPN-2, CPN-3 and CPN-4 for estimation of total ROS using commercial ROS assay kit. (d) Schematic representation for genomic DNA isolation from dead HeLa cells after PDT-PTT treatment. (e) Raman spectra of DNA isolated from PDT-PTT treated HeLa cells after different time of laser irradiation in the case of CPN-4.

Chapter 4.

Figure 4.1. . Schematic representation for synthesis of GSH-Au@Pt (a). TEM image of GSH-Au@Pt in low magnification (b). TEM image of GSH-Au@Pt in high magnification (c). HRTEM image of Pt shell in GSH-Au@Pt (d). TEM images of GSH-AuNPs and GSH-Au@Pt synthesized using increasing amounts of K_2PtCl_4 (e-h). UV/Vis spectra of (i) GSH-AuNPs and (ii-v) GSH-Au@Pt corresponding to increasing thickness of Pt shell (i). XPS survey spectrum of GSH-Au@Pt (j). Au 4f, Pt 4f and S 2p high resolution XPS peaks for GSH-Au@Pt (j-m).

Figure 4.2. a) Thiolated ligands used in the control experiment for the synthesis of Au@Pt core-shell strucures and b) corresponding TEM images. **Figure 4.3.** Combined schematic representation for test of GSH-Au@Pt to show oxidase/peroxidase like activity (a). Plot of absorbance at 505 nm due to the formation of Fe(III)-hydroxamate complex vs glucose concentration used for the reaction without any catalyst (i), in the presence of GSH-AuNPs (ii) and GSH-Au@Pt (iii) (b). Plot of absorbance at 651 nm due to the formation of oxidized

TMB by H_2O_2 vs reaction time for the reaction without any catalyst (i), in the presence of GSH-AuNPs (ii) and GSH-Au@Pt (iii) (c).

Figure 4.4. Schematic representation for colorimetric detection of D-glucose using GSH-Au@Pt nanoprobe and mechanistic proposal for cascade enzyme-mimetic recognition and conversion of glucose to gluconic acid and H_2O_2 mediated dimerization of interfacial GSH ligands (a). Solution color images of the GSH-Au@Pt after addition of different concentrations of glucose (b). 3-D graphical representation for change in absorbance at 530 nm as the function of time and concentration of glucose (c). Raman spectra obtained from GSH-Au@Pt glucose (100 mM) assay mixture at different time interval.

Figure 4.5. Spectra of GSH-AuNPs and GSH-Au@Pt (a). Optimized minimum energy complex of S-methyl-GSH and D-glucose using DFT (B3LYP, 631-G) (b). ^1H NMR spectra of D-glucose, GSH and equimolar mixture of D-glucose and GSH in D_2O (c). Raman spectra of D-glucose, GSH-Au@Pt and mixture of D-glucose and GSH-Au@Pt (d).

.

Figure 4.6. Performance of GSH-Au@Pt nanoprobe at different pH and temperature (a) Change in absorbance at 525 nm for GSH-Au@Pt and at 505 nm for GOx (in gluconic acid specific detection assay) in the presence of 100 mM glucose (b). Change in absorbance at 530 nm for GSH-Au@Pt nanoprobe at different temperatures in the presence of different concentrations of glucose.

Figure 4.7. Performance of GSH-Au@Pt nanoprobe in comparison with commercial urinalysis platform (Multistix 10 SG by CLINITEK) using artificial urine samples having known concentrations of glucose (a). Measurement of

List of Tables.

Chapter 1.

Chapter 1

Glutathione dimerization-based plasmonic nanoswitch for biodetection of reactive oxygen and nitrogen species

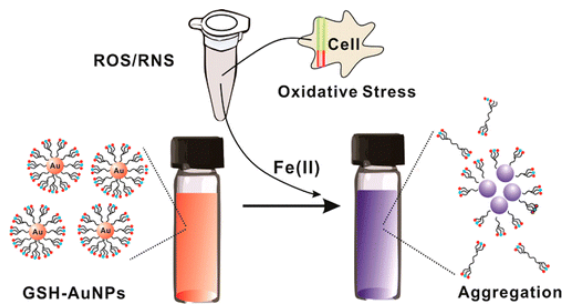

1.1 Introduction.

Reactive oxygen and nitrogen species (ROS/RNS) operate as signaling molecules under various physiological conditions and also provide host defense against bacterial and fungal pathogens.[1] These reactive species are normally generated at a low level by human spermatozoa in order to perform its physiological function, but the overproduction of ROS/RNS is involved in the pathogenesis of many diseases such as cardiovascular diseases, cancer, and neurodegenerative diseases.[2, 3] Further, the quantitative analysis of ROS/RNS has been used in evaluating the biological toxicity of nanomaterials.[4] Several methods for the detection of ROS/RNS have been developed using fluorophores, chromophores, luminophores,[5] polymer-DNA composites,[6, 7] and quantum dots.[8-11] However, these methods have several limitations including tedious operation, complicated setup, limited dynamic range, low sensitivity, use of expensive reagents, and the presence of serious matrix effects, and more rapid, quantitative, reliable, sensitive, and cost-effective detection methods for ROS/RNS have great demand in materials science, biology, and medicine. The plasmonic properties, biocompatibility, and availability of various surface modification chemistries through conjugation with different molecules make gold nanoparticles (AuNPs) excellent optical biosensing substrates.[12-26] Recently, a few papers have been published about the ROS detection using AuNPs, but the detection target was mainly limited to a specific type of ROS such as H_2O_2 in those reports.[27-31, 11]

Here, we report a method that utilizes glutathione(GSH)-modified plasmonic nanoparticles and their plasmonic couplings, induced by the ROS/RNS-activated dimerization of GSHs to GSH disulfides (GSSGs) and the Fenton reaction, to detect the subtle changes in the concentration of various

ROS/RNS in one solution (Scheme 1.1). It was shown this straightforward GSH-AuNP-based method can detect H_2O_2, ·OH, $^-$OCl, NO, and O_2^-. We further applied this method to the quantitative detection of oxidative stress from normal and cancerous cells. A major working principle for this method is that the ROS/RNS-based dimerization of GSH to GSSG on the AuNP surface induces the detachment of GSSGs and subsequent AuNP aggregation and plasmonic couplings between particles (Scheme 1.1). GSH has thiol, carboxyl, and amine groups and is water-soluble and biocompatible.[32-36] In our approach, the thiol group in GSH structure was used to stably conjugate GSHs to AuNPs to form the GSH-AuNPs. When the GSH-AuNPs are exposed to the ROS/RNS in radical forms, the GSH molecules, present on AuNPs, readily react with ROS/RNS to form GSSGs which are unable to coordinate to AuNPs because of steric hindrance caused by bulky groups around sulfur atoms of GSSGs.[37] The ROS/RNS-driven formation of GSSGs induces the detachment of these ligands from AuNPs, resulting in the destabilization of the GSH-AuNPs. This eventually induces AuNP aggregation and plasmonic couplings between plasmonic AuNPs[10] for solution color change and red shift in the UV–vis spectrum. In the case of nonradical species (H_2O_2 in this case), it is necessary to convert them into radical species for making them more reactive with GSHs in forming GSSGs. For this purpose, we used the Fenton reaction—$FeCl_2$-catalyzed decomposition of H_2O_2.[1, 38, 39] As shown in Figure 1.1, the Fenton reaction can readily convert H_2O_2 into ·OH, and a perfectly biocompatible water molecule is produced when the reaction is completed (Figure 1.1a). In cell experiments, we found that these GSH-AuNP probes can be readily internalized by cells and were distributed outside cell nucleus. Finally, we used these probes for

detecting total ROS/RNS levels from cell lysates and compared the results from six different cell lines (three normal and three cancerous cell lines).

1.2 Results and Discussion.

Synthesis of GSH-AuNPs.

GSH-AuNPs were prepared by a literature method in 10 mM phosphate buffer (PB, pH 7.4).[33] Synthesized probes were characterized by the UV–vis spectroscopy (Agilent UV–visible spectrophotometer G1103A), transmission electron microscopy (JEOL JEM-1400 transmission electron microscope (Figure 1.2), and dynamic light scattering and zeta potential measurements (Zetasizer Nano, Malvern Instruments Ltd., England) (please see the Experimental Section for details). The stability of our probes was tested under various pH conditions, and we confirmed that they are stable from pH 5.0 to pH 8.0 (Figure 1.3).

Detection of H_2O_2 by Using GSH-AuNPs with or without the Fenton Reaction.

First, in testing the Fenton reaction for GSH-AuNPs, a series of different concentrations of H_2O_2 were added to 47 nM GSH-AuNPs in 100 μL of PB (10 mM, pH = 7.4). After incubating these mixtures at 25 °C for 2 h, solution color was monitored and UV–vis spectra were recorded (Figure 1.1). When no $FeCl_2$ was added, the absorption intensity of the GSH-AuNPs at 525 nm gradually decreases with gradual increase in H_2O_2 concentration and solution color was changed from purple to blue (Figure 1.1b). The H_2O_2 detection range

was from 1.29 μM to 1.29 M. Importantly, when 10 mM $FeCl_2$ (10 μL) was added to the probe solution, assay sensitivity was dramatically increased and as low as 1.29 nM H_2O_2 was detected (Figure 1.1c). Interestingly, solution color was changed from purple to yellowish-brown due to AuNP aggregation and increase in Fe^{3+} ions as H_2O_2 concentration increases. In a control experiment, we found that the sole addition of Fe^{2+} to the GSH-AuNPs in the absence of ROS/RNS did not lead to aggregation of the GSH-AuNPs or any noticeable changes in the color or spectra of the resulting AuNPs (Figure 1.4).

To probe our proposed mechanism for ROS/RNS detection, we used the Raman spectroscopy in characterizing the glutathione molecules on the Au surface. The Raman spectroscopy is a technique that can characterize the vibrational modes of individual bonds and offer insight in chemical structure, and Raman signals can be easily detected in our case because of the surface-enhanced Raman scattering for the molecules on the plasmonic gold surface. In Figure 1.5a, hydroxyl radicals, generated from the Fenton reaction, react with GSH molecules present on the gold surface and form GSSGs, which are unable to coordinate to AuNPs because of the structural change and steric hindrance, caused by bulky groups around sulfur atoms of GSSGs. The Raman experiments (inVia Raman Microscope, Renishaw, Wotton-under-Edge, UK) were performed to follow the Fenton reaction-based GSSG formation (25 °C, Ar laser of 514.5 nm laser line with power 50 mW). In Figure 1.5b, the Raman spectra for GSH-AuNPs and final product, respectively, are shown. We observed the bands at 2579 cm^{-1} (S–H stretching), 678 cm^{-1} (C–S stretching), 1706 cm^{-1} (C═O stretching), 1632 cm^{-1} (amide stretching), and 2890 cm^{-1} (O–H stretching), respectively, for GSH-AuNPs. For the product, we observed the

bands at 511 cm^{-1}(S–S stretching), 679 cm^{-1} (C–S stretching), 1708 cm^{-1} (C═O stretching), 1640 cm^{-1} (amide stretching), and a broad band at 2881 cm^{-1} (O–H stretching). For the product case, we did not observe the thiol (S–H) peak, which indicates the GSH molecules on the gold surface were oxidized to GSSGs. Further, we performed an X-ray photoelectron spectroscopy (XPS) experiment (ThermoVG, UK) to characterize the number of ligands on each AuNP surface. By comparing the atomic ratios of sulfur to gold before and after the reaction between GSH-AuNPs and hydroxyl radicals, generated from the Fenton reaction, we observed the change in the number of ligands per particle. From the XPS results it was found that the atomic ratio (sulfur/gold) during the reaction decreased from 5.89 to 0.47. To test the long-term stability of the ligands on probes, we prolonged the reaction time up to 24 h. There is only negligible increase in the atomic ratio (sulfur/gold) to 0.51. All these results point out that the sulfur atoms in bulky GSSGs in solution did not coordinate back to AuNPs once they were released from particles. The formation of GSSG was further verified by the mass spectrometry (Finnigan MSQ Plus Surveyer MS system with photodiode array detector using electron spray ionization), where a molecular ion peak corresponding to GSSG appeared at m/z = 612.81 (Figure 1.6). Finally, the ^{1}H NMR (500 MHz) (Varian Inova-500, Varian Assoc., Palo Alto, USA) analysis of GSH-AuNPs before and after ROS/RNS addition confirmed the quantitative conversion of GSH to GSSG in the presence of ROS/RNS (Figure 1.7).

Detection and Quantification of Various ROS/RNS Using GSH-AuNP Probes.

Next, we used the GSH-AuNP probes for detection of many different kinds of biologically relevant ROS/RNS species including hypochlorite (ClO^{-}), nitric oxide (NO), superoxide (O_2^{-}), H_2O_2, and ·OH. In our experiments, NO was generated

from $NaNO_3$ and diethylammonium(Z)-1-(N,N-diethylamino)diazen-1-ium-1,2-diolate, and O_2^- was generated from xanthine oxidase and xanthine. NaOCl was used as the source of ClO^- (see the Experimental Section for more details). In each case, 10 μL of ROS/RNS was added to 90 μL of 47 nM GSH-AuNP solution, and the resulting solution was incubated on an orbital shaker at 25 °C for 2 h. It should be noted that ·OH was generated from H_2O_2 by the addition of $FeCl_2$ (Figure 1.1). The GSH-AuNPs showed good response to all these ROS/RNS with high detection sensitivity. Figure 1.8a shows the dependence of ΔA_{525} as a function of ROS/RNS concentration where ΔA_{525} is the difference between optical densities in the absence and presence of ROS/RNS at 525 nm, respectively. These results show a linear relationship between ΔA_{525} and ROS/RNS concentration with a wide dynamic range (R^2= 0.9288, 0.8439, 0.90687, 0.98729, and 0.95144 for H_2O_2, ·OH, O_2^-, NO, and ClO^-, respectively). The minimum detectable concentrations for O_2^-, NO, and ClO^- were found to be 1.29 mM, 129 μM, and 1.29 μM, respectively. The detection sensitivity of ROS using our method was comparable to a luminal-based assay.[40] It should be noted that, although O_2^- is a primary source of ROS/RNS in biological systems, this species is least reactive for our probe. Figure 1.8b shows the reaction kinetics results for each ROS/RNS, where corresponding ΔA_{525} values were plotted as a function of reaction time. For this study, the identical concentration for all the species (1.29 mM in 10 mM PB at pH = 7.4) was used, and the reaction progresses for each species were monitored up to 120 min at 25 °C. The results revealed that all the reactions were nearly completed at ~80 min. All the reactions did not progress any further after 100

min. More reactive ROS/RNS molecules (H_2O_2, ·OH, and ClO^-), which are relatively stronger oxidants than NO and O_2^-, showed faster kinetics and more changes in ΔA_{525} than NO and O_2^-, and these results validate the quantification capability of our assay. [1, 38]

Effect of Temperature on Reaction Kinetics of GSH-AuNPs with Hydrogen Peroxide.

Other than room temperature, the other relevant temperature is physiological temperature, 37 °C. Actually, we used our probes at 37 °C for cell assays. We compared probes with respect to solution color, surface charge (zeta potential), and particle size at room temperature and 37 °C, respectively. There was only a little change in the zeta potential and particle size with no solution color change and no particle aggregation when temperature was changed from 25 to 37 °C (Figure 1.9). Further, the cell assays with GSH-AuNPs were performed at 37 °C, and the results are shown in the latter part of this paper.

Comparison of GSH with Other Thiolated Ligands.

Next, we examined the specificity in the reaction between ROS/RNS and GSH on AuNP surface by interacting other thiolated group-modified AuNPs with ROS/RNS (Figure 1.10a). For this study, we selected a variety of thiolated ligands including cysteine, methyl cysteine, 2-aminoethanethiol, mPEG-SH (MW 5000), and thioctic acid. These functional ligands were modified to AuNPs based on reported procedures (see the Experimental section for details)[41-43] and characterized by the UV–visible spectroscopy, TEM, dynamic light scattering and zeta potential measurements. It should be noted that commercially

available 15-nm AuNPs were used for the synthesis of mPEG-SH-capped AuNPs. For each case, 90 μL of 47 nM AuNP probe solution was mixed with 10 μL of 12.9 mM H_2O_2, and the reaction mixture was stirred at 25 °C for 2 h. After 2 h reaction, the UV–vis absorbances at 525 nm before and after the addition of ROS/RNS were recorded and compared. Importantly, as shown in Figure 1.10b, the addition of H_2O_2 had little effect on change in the absorbance at 525 nm for all non-GSH-modified AuNPs, unlike the case for GSH-AuNPs. This shows that our assay strategy does not work for AuNP probes with other thiolated ligands but works only for GSH-modified AuNPs that can form dimeric GSSG upon the addition of ROS/RNS species. This result could be attributed to its structural feature and low reduction potential (50 mV or lower) of GSH when compared to other thioled ligands such as cysteine.[44, 45]

GSH-AuNPs as Cell Assay Probes.

Our next goal was to exploit potential for the use of our GSH-AuNPs in monitoring and quantifying the ROS/RNS amount from normal and cancerous cells. Several reports suggest that many types of cancerous cells generate the increased amount of ROS/RNS due to oncogenic stimulation, increased metabolic activity and mitochondrial malfunction.[46-50] Therefore, this oxidative stress of cancer cells can be used as a hallmark for the diagnosis by differentiating normal cells from cancerous cells.[51, 52] It should also be noted that obtaining the quantitative information about a change in ROS/RNS level among normal cells or cancerous cells could be valuable for studying oxidative stress in biochemistry and cell biology.[53] As a control experiment, we first tested the response of our GSH-AuNPs probes for the mixture of different kinds of ROS/RNS in one solution [10 μL of a solution with 12.9 μM H_2O_2, ·OH,

O_2^-, NO, and ClO^- was added to 90 μL of 47 nM GSH-AuNPs in 10 mM PB solution at pH = 7.4]. After this mixture was incubated at 25 °C for 2 h, UV–vis spectrum was recorded. The result showed significant decrease in the absorption intensity at ~525 nm (Figure 1.11).

Next, we conducted the cellular uptake experiments of the GSH-AuNPs with six different cell lines (listed in Table 1.2, normal cells: 3T3-L1, NIH3T3, and C2C12; cancerous cells: A549, HeLa, and Hep3B). The cellular uptake of the GSH-AuNPs was characterized by the cell fixation and subsequent TEM imaging after the incubation of the GSH-AuNPs with cells (see the Experimental Section for more details). As shown in Figure 1.12a, many GSH-AuNPs were found inside the cell for all of six cell lines, but it should be noted that the GSH-AuNPs were not found inside the cell nucleus. These results confirm that the GSH-AuNPs can be readily internalized by both cancerous and normal cells and these probes have potential as ROS/RNS detection probes inside the cell. Interestingly, although the probes have highly negative charges on the surface (zeta potential = − 39.76 mV), there is no significant hindrance for the GSH-AuNPs in entering through cellular membrane. This could be due to the ionic screening effect by various serum proteins in cell growth medium, and other cell membrane components could play important roles for the endocytosis of the probes.[54] Next, we performed the cytotoxicity tests for the GSH-AuNPs with six different cell lines using the Cell Count Counting Kit assay.[55] A wide range of GSH-AuNP concentrations (2 nM to 200 μM) showed no or little cytotoxicity for all the tested cell lines (Figure 1.12b; see the Experimental Section for experimental details). These

GSH-AuNPs were found to have little or no toxicity to live cells even at high concentrations.

Detection of ROS/RNS in Normal and Cancerous Cells.

In a typical experiment, six cell lines (Table 1.2: normal cells, 3T3-L1, NIH3T3, and C2C12; cancerous cells, A549, HeLa and Hep3B) were cultured in serum-confluent medium for 3 days, respectively, and the same number of cells (5×10^5 cells in 10 μL of PB of 10 mM at pH 7.4) for each case were detached from the cell incubating plate (6-well clear multiple well plates, Corning, Tewksbury, MA, USA), followed by cell lysis using the M-PER mammalian protein extraction reagent (Pierce, Rockford, IL, USA). Cell debris were removed from cell lysate using centrifugation, and the remaining solution was co-incubated with 90 μL of 47 nM GSH-AuNPs in 10 mM PB solution in the presence of 10 mM $FeCl_2$ at 37 °C for 4 h. The supernatant from cell-lysate solution that was coincubated with GSH-AuNPs was used for the UV–vis measurement (see the Experimental Section for experimental details). The spectral change in the absorbance at 525 nm was measured with the UV–vis spectrophotometer. We were able to observe the change in absorbance depending on cell type. Overall, as shown in Figure 1.13b, larger ΔA_{525} values were observed for all the cancerous cells than the values for the normal cells (Figure 1.13), and this result agrees well with other literatures.[20] The error bars are relatively small, and detection of ROS/RNS was successfully performed using only one type of probe. To further validate our results, a commercially available in vitro ROS/RNS assay (OxiSelect, Cell biolabs, INC., San Diego, CA, USA) was also conducted, and the results were compared to the GSH-AuNP

assay results. The OxiSelect assay is a fluorescent signal-based method for measuring total ROS/RNS free radical activity.[56] Importantly, the ROS/RNS detection results from the commercial assay showed a very similar tendency as observed in our GSH-AuNP assay results (Figure 1.13b,c; see the Experimental Section for details).

1.3 Experimental Section.

Chemicals.

Gold nanoparticles (15 nm in diameter) were purchased from Ted pella (Redding, CA, USA) and used without further purification. Tetrachloroauric acid, glutathione, ferrous chloride, 2-aminoethanethiol, N,N-dimethylformamide, deuterium oxide, l-cystein methyl ester, and l-cystein were purchased from Aldrich (St. Louis, MO, USA). HEPES, toluene, tetra-n-octyl ammonium bromide, 6,8-dithioctic acid, xanthine oxidase, and xanthine were purchased from Sigma (St. Louis, MO, USA). Sodium borohydride, hydrogen peroxide, sodium nitrate, and hydrochloride were purchased from Daejung chemical and metals (South Korea). m-PEG-SH was purchased from Laysan Bio, Inc. (Tower Drive Arab, AL). NANOpure water (>18.0 MΩ), purified using a Milli-Q water purification system, was used for all the experiments.

Preparation of GSH-AuNPs.

GSH-AuNPs were synthesized according to literature procedures with slight modification.[33] An aqueous solution of tetrachloroauric acid ($HAuCl_4 \cdot 3H_2O$, 1 mL, 0.025 M) was added to GSH (7.8 mL, 0.019 M) dissolved in 10 mM sodium

phosphate buffer (PB, pH 7.4) (adjusted by 1 M NaOH). The solution turned clear after continuous stirring for 30 min. Then, a freshly prepared $NaBH_4$ solution (2 mg/mL dissolved in ice-cold water, 10-fold molar excess) was rapidly added with vigorous stirring (ca. 1200 rpm). The solution immediately became dark, indicating the reduction of gold salt and formation of nanoparticles. The reaction was allowed to proceed for 12 h at 25 °C. Excess ligands were removed from the solution by centrifugation at 10000 rpm for 10 min and repeated washing by buffer solution. The obtained gold nanoparticle precipitate was dispersed in 100 mL of PB (10 mM, pH 7.4) and stored at 4 °C for further characterization.

Preparation of 2-Aminoethanethiol-AuNPs.

A 400 mL aliquot of 213 mM 2-aminoethanethiol was added to 40 mL of 1.42 mM $HAuCl_4$. After the mixture was stirred for 20 min at 25 °C, 10 mL of 10 mM $NaBH_4$ was added, and the mixture was vigorously stirred for 10 min at 25 °C in the dark. After further mild stirring, the sample was stored in the dark at 5 °C and used within 2 months.[41]

Preparation of Thoictic Acid-AuNPs.

Au clusters were synthesized in toluene by the two-phase reduction of aqueous $HAuCl_4$ (3 mL, 30 mM, Aldrich), transferred to the organic phase using tetra-n-octylammonium bromide (TOABr) in toluene (8 mL, 50 mM, Fluka), and reduced with aqueous sodium borohydride (2.5 mL, 0.4 M, Aldrich). Cluster derivatization was carried out by overnight incubation in a 0.1 M solution of 6,8-dithioctic acid (TA, Sigma) in toluene. The carboxylic acid-terminated clusters were insoluble in toluene and were separated by centrifugation, and

washed several times with toluene and once with 1-propanol to remove reaction byproducts. The purified clusters were redissolved in an aqueous solution of pH 10 containing 20 mM of HEPES [N-(2 hydroxyethyl)piperazine-N′-(2-ethanesulfonic acid), Sigma].[42]

Preparation of mPEGSH-AuNPs.

An aqueous solution containing 1.36×10^{-7} moles of mPEGSH (MW 5000), previously sonicated for 15 min, was added under vigorous stirring to 10 mL of commercially available 15-nm gold sphere. The mixture was allowed to react for overnight. PEG-modified particles were then centrifuged (10000 rpm) twice to remove the excess mPEGSH and redispersed in 4 mL of deionized water.

Preparation of L-Cysteine-AuNPs.

A 10^{-4} M aqueous solution (100 mL) of chloroauric acid ($HAuCl_4$) was reduced by 0.01 g of sodium borohydride ($NaBH_4$) at 25 °C. The gold nanoparticles were stabilized by the addition of an aqueous solution of L-cysteine to the hydrosol to yield a final concentration of 10^{-4} M cysteine in solution. The pH of the cysteine-capped gold colloidal solution was 9. At this pH, the cysteine molecules on the surface of the gold nanoparticles would be negatively charged (pI of cysteine, 5.06), thus stabilizing the nanoparticles electrostatically.[43]

Preparations of L-Cystein Methyl Ester-AuNPs.

A 1.42 mM aqueous solution (50 mL) of chloroauric acid was mixed with 213 mM aqueous solution (400 μL) of L-cystein methyl ester and the reaction

mixture was stirred for 20 min at 25 °C. Then the solution was reduced by the addition of 10 mM aqueous solution (10 μL) of $NaBH_4$. The reaction mixture was stirred for overnight. After further mild stirring, the sample was stored in the dark at 5 °C and used within 3 months.

Generation of ROS/RNS

(a) **H_2O_2**: H_2O_2 was diluted appropriately by 10 mM PB at pH 7.4. Then, a H_2O_2 stock solution in buffer was prepared. To a solution of 90 μL of GSH-AuNPs in 10 mM PB at pH 7.4, stock solution was added at 25 °C, and then the solution was analyzed by UV–vis absorption spectra after 2 h. (b) **Generation of ·OH**: 10 mM solution of $FeCl_2$ was prepared in 10 mM PB at pH 7.4. After 80 μL of GSH-AuNPs and 10 μL of H_2O_2 were mixed in PB (10 mM, pH 7.4), 10 μL of $FeCl_2$ solution was added at 25 °C. UV–vis absorption spectra were measured after 2 h. (c) **Generation of $^-$OCl**: NaOCl solution was diluted appropriately in 0.1 M NaOH aq. To a solution of 90 μL of GSH-AuNPs in 10 mM PB (pH 7.4), 10 μL of $^-$OCl solution was added at 25 °C, and UV–vis absorption spectra was measured after 2 h. (d) **Generation of O_2^-**: Xanthine oxidase (XO) was dissolved in PB (10 mM, pH 7.4). Xanthine was dissolved in DMF. To a solution of 90 μL of GSH-AuNPs in PB (10 mM, pH 7.4), XO solution and xanthine solution (final concn, 33 μM, containing 6.7% DMF as a cosolvent) were added at 25 °C, and UV–vis absorption spectra were measured after 2 h. (e) **Generation of NO**: A solution of $NaNO_3$ in PB (10 mM, pH 7.4) and DEANO (DEA NONOate; diethylammonium (Z)-1-(N,N-diethylamino) diazen-

1-ium-1,2-diolate) in 0.01 M NaOH was used. To initiate decomposition of the NONOate, 5 μL of 1.0 M HCl was added to bring the solution to approximately pH 4. After 1 h, 5 μL of 1.0 M NaOH was added to bring the solutions up to approximately pH 7.4. The solutions were then added to 90 μL of GSH-AuNP in PB (10 mM, at pH 7.4).

Cell Cross-Section Imaging Using the Transmission Electron Microscopy.

For cell cross-section imaging, GSH-AuNP incubated cells were first detached from the well plate. After a wash with PBS, at least 5×10^5 cells were fixed for 2 h with modified Karnovsky's fixative (2 % paraformaldehyde and 2 % glutaraldehyde in 0.05 M sodium cacodylate buffer, pH 7.2). After three washings with 0.05 M sodium cacodylate buffer (pH 7.2) at 4 °C, cells were fixed with 1 % osmium tetroxide in 0.05 M sodium cacodylate buffer (pH 7.2) for 2 h and then washed with distilled water two times. Fixed cells were En bloc stained at 4 °C for overnight using 0.5 % uranyl acetate and then dehydrated with a graded concentration series of ethanol (30 %, 50 %, 70 %, 80 %, 90 %, 100 %, 100 %, and 100 % ethanol; 10 min for each dehydration step). Infiltrated cells using propylene oxide and Spurr's resin were polymerized at 70 °C for 24 h. Various sections of the resin block were cut using the ultramicrotome (MT-X, RMC, Tucson, AZ, USA) and stained 2 % uranyl acetate and Reynolds' lead citrate for 7 min, followed by transferring the section of interest onto a 300 mesh copper TEM grid.

Toxicity Assay.

The cytotoxicity of various concentrations of GSH-AuNPs was evaluated using the Cell Counting Kit (CCK-8, Dojindo lab., Japan). Cells were grown in a 96-well plate in 100 μL of DMEM supplemented with FBS. After 24 h seeding, cells were incubated with various concentrations (from 2 nM to 200 μM) of glutathione-modified gold probes for 48 h, and cell viability assay was carried out. The metabolic activity of the cells was measured using CCK-8 (a sensitive colorimetric assay for the determination of the number of viable cells after incubating with probes).[55] Then, 10 μL of the CCK-8 solution was directly added to the incubated cells in each well. After 2 h incubation at 37 °C, the amount of formazan dyes, generated by dehydrogenased of active cells, was measured by a microplate reader (Anthos 2010, Anthos Labtec, Eugendorf, Austria).

Cell Lysis.

For cell lysis, well grown cells were detached from a well plate using TrypLETM Express (1X, Gibco, Invitrogen, USA). After being perfectly washed with DPBS, the same number of cells (5×10^5 cells in this case) was incubated with 200 μL of cell lysis buffer (M-PER mammalian protein extraction reagent, Pierce, Rockford, IL, USA) with gentle shaking for 10 min. After cell debris was removed by simple centrifugation (~14000 g for 5 min), the supernatant was transferred to a new eppendorf tube for the assay that followed.

Detection of ROS from Cells.

To compare the ROS level of different type of cells, three types of cancer cells [HeLa (human cervical cancer cell), A549 (human lung cancer cell) and

Hep3B (human hepatoma cell)] and three types of normal cells [3T3-L1 (fibroblast cell), NIH3T3 (fibroblast cell), and C_2C_{12} (myoblast cell)] were cultured in Dulbecco's Modified Eagle's Medium (DMEM) (GIBCO, Invitrogen Inc., Carlsbad, CA, USA), supplemented with 10 % (v/v) Fetal Bovine Serum (FBS) (GIBCO, Invitrogen Inc., Carlsbad, CA, USA) and 5 % penicillin/streptomycin (Sigma-Aldrich). After 3 days of culturing, cells were detached from the culturing flasks with trypsin EDTA (Gibco, Invitrogen Inc., Carlsbad, CA, USA). The cells were then washed with PB (10 mM, pH 7.4) three times. The cells ($\sim 5 \times 10^5$ cells) were incubated with 47 nM GSH-AuNPs in 90 μL of PB (10 mM, pH 7.4) followed by the addition of 10 mM ferrous chloride (10 μL) to the solution to generate more detectable ROS radical species. After 4 h incubation and subsequent centrifugation at 2000 rpm for 3 min, 60 μL of the supernatant was collected for UV–vis analysis. UV–vis absorbance spectra of GSH-AuNP-cell mixtures were recorded for each cell line, and the respective supernatant from a cell-cultured solution was used as a blank.

Commercial in Vitro ROS/RNS Assay.

To validate our GSH-AuNP-based cell assay results, the results from commercially available OxiSelect In Vitro ROS/RNS Assay Kit were compared. The OxiSelect assay is a fluorescence-based method in which fluorescence intensity is proportional to the total ROS/RNS level within the sample. This assay utilizes a proprietarily quenched fluorogenic probe, dichlorodihydrofluorescin DiOxyQ (DCFH-DiOxyZ), which can specifically detect ROS/RNS. The DCFH-DiOxyZ can be transformed to the highly reactive fluorescence-quenched DCFH form, and the quenched fluorescence signal from the DCFH can be turned on upon ROS/RNS detection. The same number of

cells (5×10^5 cells) was used for all the experiments after cell detachment from the culture dish and cell lysis. Next, 50 μL of cell lysate was added to a 96-well plate (30096, SPL lifescience, Gyeonggi-Do, South Korea), suitable for fluorescence measurement. DCFH can be highly reactive to ROS/RNS by mixing 50 μL of catalyst with 100 μL of the DCFH solution (DCFH-DiOxyQ, priming reagent and stabilization solution with the recommended ratio by the manufacturer). After 45 min incubation at room temperature with gentle shaking, the fluorescence signal, which is proportional to the ROS/RNS level, can be obtained using a fluorescence plate reader (The SynergyHT, BioTek, VT, USA) with 480 nm excitation and 530 nm emission.

Effect of pH on Absorbance of GSH-AuNPs.

We evaluated the effect of pH on absorbance. As shown in Figure 1.4, the pH hardly influenced the absorbance properties of GSH-AuNPs under physiological conditions (pH 5.0 to pH 8.0)

Characterization of GSH-AuNPs before and after the Addition of ROS/RNS by Mass Spectroscopy.

We characterized the formation of GSSG from the GSH-AuNPs in the presence of the ROS/RNS by mass spectrometric studies (Finnigan MSQ Plus Surveyer MS system, photodiode array detector using electron spray ionization). In case of GSH-AuNPs, only certain fragments were observed such as base peak at m/z = 307.78 for GSH and additional peaks at m/z 178.78 for the loss of glycine moiety (Figure 1.6a). We also performed the mass spectroscopy for final product of our reaction mixture of GSH-AuNPs with hydroxyl radicals, generated from Fenton reaction. This exhibited base peaks at m/z 306.93 and at m/z 612.81 corresponding to GSSG (Figure 1.6b).

Characterization of GSH-AuNPs before and after the Addition of ROS/RNS by ^{1}H NMR.

We also used ^{1}H NMR technique (Varian Inova-500, Varian Assoc., Palo Alto, USA) to find the chemical structure of final products. The ^{1}H NMR spectra (Figure 1.6) were recorded from GSH-AuNPs before (Figure 1.6b) and after (Figure 1.6a) the reaction with hydroxyl radicals that were produced from the Fenton reaction. First, GSH-AuNPs were centrifuge at 10,000 rpm for 10 min. The supernatant was removed and the nanoparticles were dried overnight at 333 K. The GSH-AuNP solution after reaction with hydroxyl radicals, generated from the Fenton reaction, was evaporated at 40 °C under reduced pressure and dried overnight at 333 K. Sample weights for the NMR measurements were approximately 2 mg of each. The ^{1}H NMR spectrum indicates a shifting of peak position which is an evidence of the reaction that occurs on the surface of AuNP.

1.4 Conclusion.

In summary, we developed a simple and straightforward strategy to detect a wide range of different ROS/RNS molecules including NO, $^-$OCl, O_2^-, H_2O_2, and ·OH via the dimerization of GSH on AuNPs surface to GSSG upon the addition of ROS/RNS. This ROS/RNS-mediated dimerization of GSH induces the detachment of GSH from AuNPs and destabilizes AuNPs to provoke particle aggregation that results in plasmonic couplings between AuNPs. These plasmonic couplings were readily detected with the naked eyes or UV–vis spectrophotometer. This chemistry works efficiently with radical forms of ROS/RNS, and the Fenton reaction boosted the detection sensitivity for

nonradical species such as H_2O_2 by converting it to ·OH. Moreover, it was shown that other non-GSH thiol molecule-modified AuNP probes were not sensitive to the presence of ROS/RNS, indicative of high specificity of this method to GSH-AuNPs. Finally, we showed that GSH-AuNPs probes can be used to quantify the amount of ROS/RNS from normal and cancerous cells to measure oxidative stress in cell. Our results proved that these probes can be internalized by cells and have no or little cytotoxicity even at high probe concentrations (over μM level). These show that the GSH-AuNPs can be potentially used as ROS/RNS detection probes inside the cell. Our assay quantitatively detected higher amount of ROS/RNS from cancerous cells than from normal cells, which agrees well with oxidative stress-based results reported in other literatures, and these results were matched well by commercially available assay kit-based results. These versatile and simple ROS/RNS detection probes and assay platform offer new opportunities in detecting and quantifying the amount of ROS/RNS and relating ROS/RNS detection with oxidative stress in cells, differentiating normal cells from cancerous cells, and various other studies in ROS/RNS-related cell signaling and phenotypic changes.

1.5 References.

1. Autréaux, B. D.; Toledano, M. B. Nat. Rev. Mol. Cell Biol. 2007, 8, 813–824.

2. Valko, M.; Leibfritz, D.; Moncol, J.; Cronin, M. T.; Mazur, M.; Telser, J. Int. J. Biochem. Cell Biol. 2007, 39, 44– 84.

3. Winterbourn, C. C. Nat. Chem. Biol. 2008, 4, 278– 286.

4. Nel, A.; Xia, T.; Madler, L.; Li, N. Science 2006, 311, 622– 627.

5. Chen, X.; Tian, X.; Shin, I.; Yoon, J. Chem. Soc. Rev. 2011, 40, 4783– 4804.

6. Tang, Y.; Feng, F.; He, F.; Wang, S.; Li, Y.; Zhu, D. J. Am. Chem. Soc. 2006, 128, 14972– 14976.

7. Shen, Q.; Nie, Z.; Guo, M.; Zhong, C.-J.; Lin, B.; Li, W.; Yao, S. Chem. Commun. 2009, 8, 929–931.

8. Jiang, H.; Ju, H. Anal. Chem. 2007, 79, 6690– 6696.

9. Gill, R.; Bahshi, L.; Freeman, R.; Willner, I. Angew. Chem., Int. Ed. 2008, 120, 1676– 1679.

10. Hu, M.; Tian, J.; Lu, H.-T.; Weng, L.-X; Wang, L.-H. Talanta 2010, 82, 997– 1002.

11. Uusitalo, L. M.; Hempel, N. Int. J. Mol. Sci. 2012, 13, 10660–10679.

12. Rosi, N. L.; Mirkin, C. A. Chem. Rev. 2005, 105, 1547–1562.

13. Lee, J.-S.; Han, M. S.; Mirkin, C. A. Angew. Chem., Int. Ed. 2007, 46, 4093– 4096.

14. Wilson, R. Chem. Soc. Rev. 2008, 37, 2028– 2045.

15. Georganopoulou, D. G.; Chang, L.; Nam, J.-M.; Thaxton, C. S.; Mufson, E. J.; Klein, W. L.; Mirkin, C. A. Proc. Natl. Acad. Sci. U.S.A. 2005, 102, 2273–2276.

16. Neely, A.; Perry, C.; Varisli, B.; Singh, A. K.; Arbneshi, T.; Senapati, D.; Kalluri, J. R.; Ray,P. C. ACS Nano 2009, 3, 2834–2840.

17. Kong, B.; Zhu, A.; Luo, Y.; Tian, Y.; Yu, Y.; Shi, G. Angew. Chem., Int. Ed. 2011, 50, 1837– 1840.

18. jiang, Y.; Zhao, H.; Zhu, N.; Lin, Y.; Yu, P.; Mao, L. Angew.Chem. Int. Ed. 2008, 47, 8601– 8604.

19. Kalluri, J. R.; Arbneshi, T.; Khan, S. A.; Neely, A.; Candice, P.; Varisli, B.; Washington, M.; McAfee, S.; Robinson, B.; Banerjee, S.et al. Angew. Chem., Int. Ed. 2009, 48, 9668– 9671.

20. Chi, H.; Liu, B.; Guan, G.; Zhang, Z.; Han, M.-Y. Analyst 2010, 135, 1070– 1075.

21. Laromaine, A.; Koh, L.; Murugesan, M.; Ulijn, R. V.; Stevens, M. M. J. Am. Chem. Soc. 2007, 129, 4156– 4157.

22. Kong, B.; Zhu, A.; Luo, Y.; Tian, Y.; Yu, Y.; Shi, G. Angew. Chem., Int. Ed. 2011, 50, 1837– 1840.

23. Lim, D.-K.; Jeon, K.-S.; Kim, H.-M.; Nam, J.-M.; Suh, Y. D. Nat. Nanotechnol. 2011, 6, 452– 460.

24. Woo, J.-R.; Lim, D.-K.; Nam, J.-M. Small 2011, 7,648– 655.

25. Jang, K.-J.; Lee, H.; Jin, H.-L.; Park, Y.; Nam, J.-M. Small 2009, 5, 2665– 2668.

26. Lim, D.-K.; Jeon, K.-S.; Kim, H. M.; Nam, J.-M.; Suh, Y. D. Nat. Mater. 2010, 9, 60–67.

27. Shiang, Y.-C.; Huang, C.-C.; Chang, H.-T. Chem. Commun. 2009, 23, 3437–3439.

28. Jv, Y.; Li, B.; Cao, R. Chem. Commun. 2010, 46, 8017–8019

29. Jiang, Y.; Zhao, H.; Lin, Y.; Zhu, N.; Ma, Y.; Mao, L. Angew. Chem., Int. Ed. 2010, 49, 4800– 4804.

30. Lee, H.; Lee, K.; Kim, I. K.; Park, T. G. Adv. Funct. Mater. 2009, 19, 1884– 1890.

31. Auchinvole, C. A. R.; Richardson, P.; McGuinnes, C.; Mallikarjun, V.; Donaldson, K.; McNab, H.; Campbell, C. J. ACS Nano 2012, 6, 888– 896.

32. Polavarapu, L.; Manna, M.; Xu, Q.-H. Nanoscale 2011, 3, 429– 434.

33. Brinas, R. P.; Hu, M.; Qian, L.; Lymar, E. S.; Hainfeld, J. F. J. Am. Chem. Soc. 2008, 130, 975–982.

34. Wu, Q.; Cao, H.; Luan, Q.; Zhang, J.; Wang, Z.; Warner, J.-H.; Watt, A. R. Inorg. Chem. 2008, 47, 5882– 5888.

35. Blair, I. A. Biomed. Chromatogr. 2010, 24, 29– 38.

36. Awasthi, Y. C.; Sharma, R.; Yadav, S.; Dwivedi, S.; Sharma, A.; Awasthi, S. Curr. Drug Metab. 2007, 8, 315– 323.

37. He, X.; Zhong, Z.; Guo, Y.; Lv, J.; Xu, J.; Zhu, M.; Li, Y.; Liu, H.; Wang, S.; Zhu, Y.et al. Langmuir 2007, 23, 8815– 8819.

38. Imlay, J. A. Annu. Rev. Microbiol. 2003, 57, 395–418.

39. Page, S. E.; Wilke, K. T.; Pierre, V. C. Chem. Commun. 2010, 46, 2423– 2425.

40. Bhandari, A.; Kim, W.; Hohn, K. J. Environ. Eng. 2010, 136, 1147– 1152.

41. Niidome, T.; Nakashima, K.; Takahashi, H.; Niidome, Y. Chem. Commun. 2004, 17, 1978– 1979.

42. Abad, J. M.; Mertens, S. F. L.; Pita, M.; Fernandez, V. M.; Schiffrin, D. J. J. Am. Chem. Soc. 2007, 129, 4156– 4157.

43. Sarangi, S. N.; Hussain, A. M. P.; Sahu, S. N.; Strong, U. V. Appl. Phys. Lett. 2009, 95, 0731091–0731093.

44. Jones, D. P. Methods Enzymol 2002, 348, 93– 112.

45. Kirlin, W. G.; Cai, J.; Thompson, S. A.; Diaz, D.; Kavanagh, T. J.; Jones, D. P. Free Radical Biol. Med. 1999, 27, 1208– 1218.

46. Kumar, B.; Koul, S.; Khandrika, L. Cancer Res. 2008, 68, 1777– 1785.

47. Trachootham, D.; Alexandre, J.; Huang, P. Nat. Rev. Drug Discovery 2009, 8, 579–591.

48. Kim, J.-W.; Dang, C. V. Cancer Res. 2006, 66, 8927– 8930.

49. EO, H.; Liu, J.; Alvitar, M.; Keating, M. J.; Huang, P. Pharmacol. 2004, 53, 209– 219.

50. Szatrowski, T. P.; Nathan, C. F. Cancer Res. 1991, 51, 794– 798.

51. Weinberg, F.; Chandel, N. S. Cancer Cell. Mol. Life. Sci. 2009, 66, 3663– 3673.

52. Pelicano, H.; Carneya, D.; Huang, P. Drug Resist. 2004, 7, 97– 110.

53. Raj, L.; Ide, T.; Gurkar, A. U.; Foley, M.; Schenone, M.; Li, X.; Tolliday, N. J.; Golub, T. R.; Carr, S. A.; Shamji, A. F.et al. Nature 2011, 475, 231– 234.

54. Rosi, N. L.; Giljohann, D. A.; Thaxton, C. S.; Lytton-Jean, A. K. R.; Han, M. S.; Mirkin, C. A. Science 2006, 19, 1027– 1030.

55. Ishiyama, M.; Miyazono, Y.; Sasamoto, K.; Ohkura, Y.; Ueno, K. Talanta 1997, 44, 1299– 305.

56. Keston, A. S.; Brandt, R. Anal. Biochem. 1965, 11, 1– 5.

Scheme.

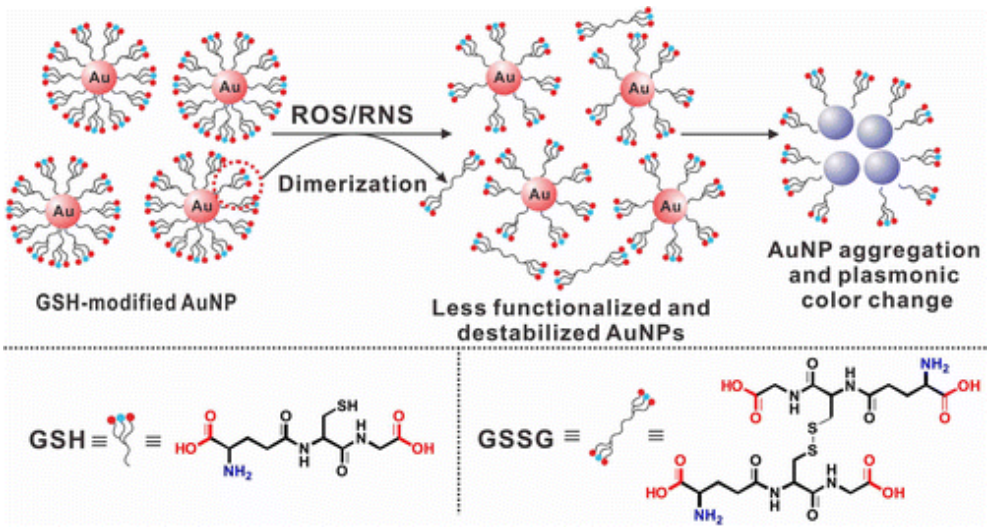

Scheme 1.1. The reaction between the glutathione-modified Au nanoparticles and ROS/RNS and the plasmonic coupling-based colorimetric ROS/RNS detection.

Figures.

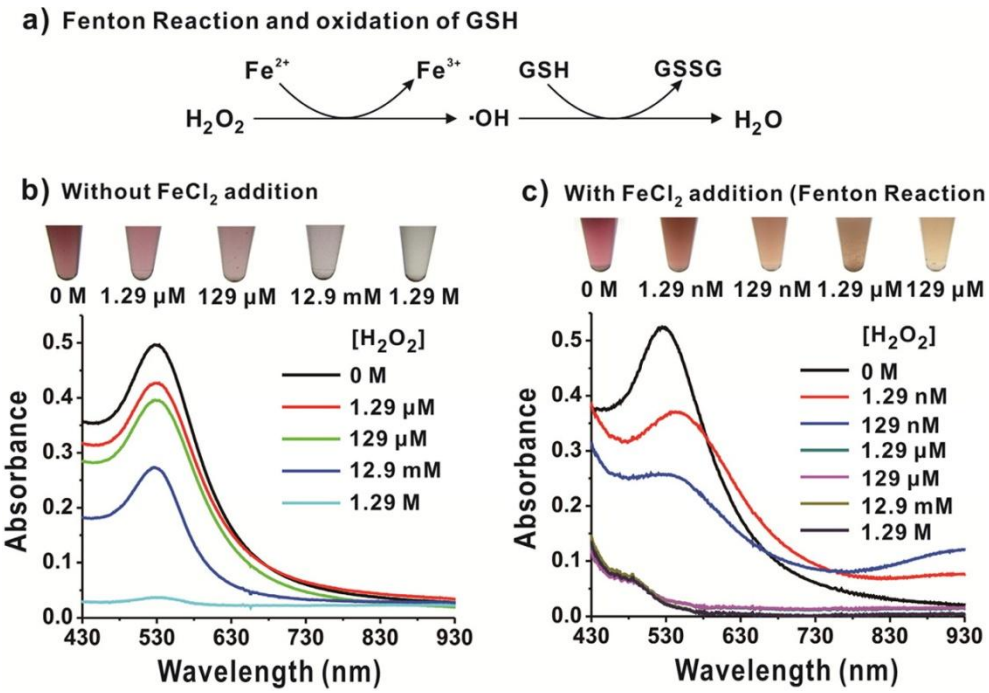

Figure 1.1. Schematic illustration The Fenton reaction-aided H_2O_2-detection using the GSH-AuNP probes. (a) $FeCl_2$-catalyzed oxidation of GSH (Fenton reaction). (b) UV–vis absorption spectra and corresponding solution color images of the GSH-AuNP solutions after the addition of a series of different concentrations of H_2O_2. (c) UV–vis absorption spectra and corresponding solution color images of the GSH-AuNP solutions after the addition of a series of different concentrations of H_2O_2 and 10 mM $FeCl_2$ solution.

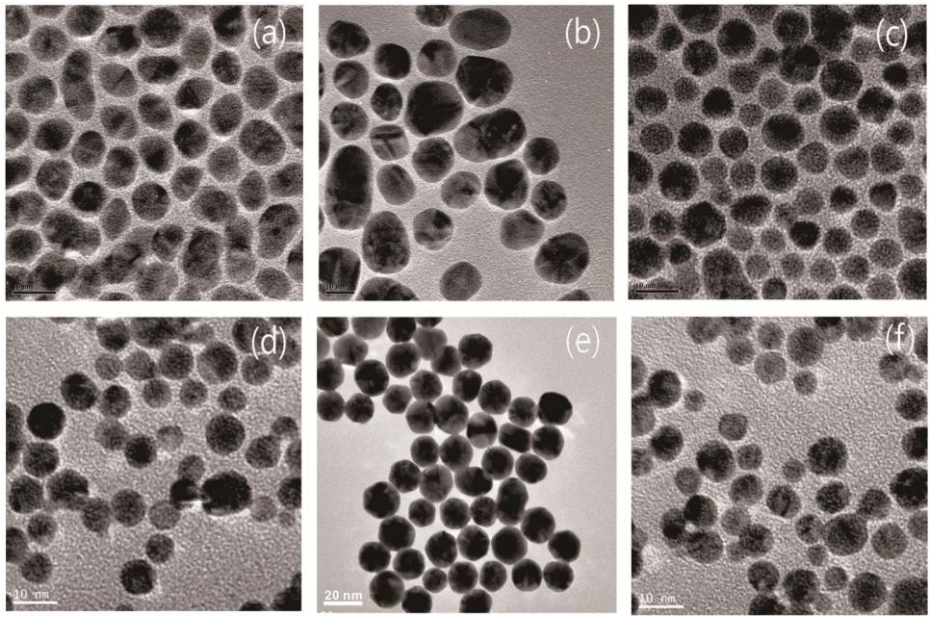

Figure 1.2. The corresponding high resolution transmission electron micrographs of the (A) GSH-AuNPs, (B) 2-aminoethanethiol –AuNPs, (C) thoictic acid –AuNPs, (D) L-cysteine –AuNPs, (E) mPEGSH –AuNPs, and (F) L-cystein methyl ester-AuNPs.

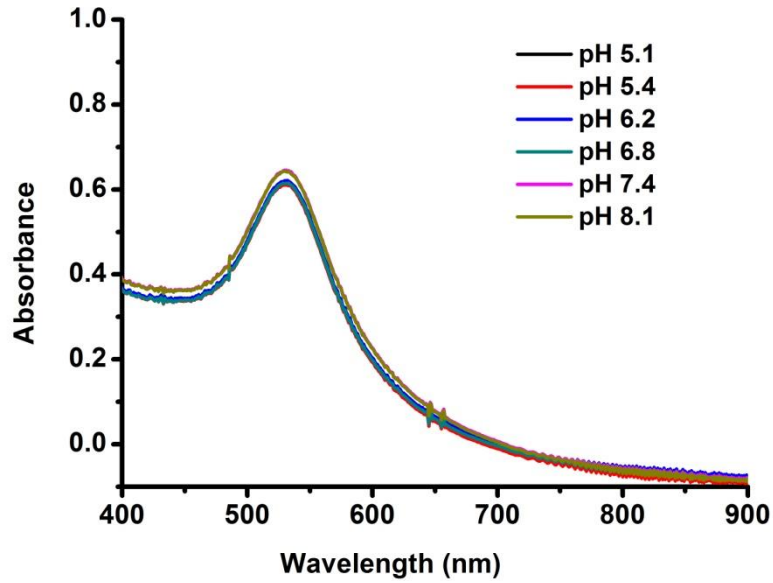

Figure 1.3. The UV-Vis absorption spectra of GSH-AuNPs were obtained in sodium phosphate buffer at various pH (pH 5.1 to pH 8.1).

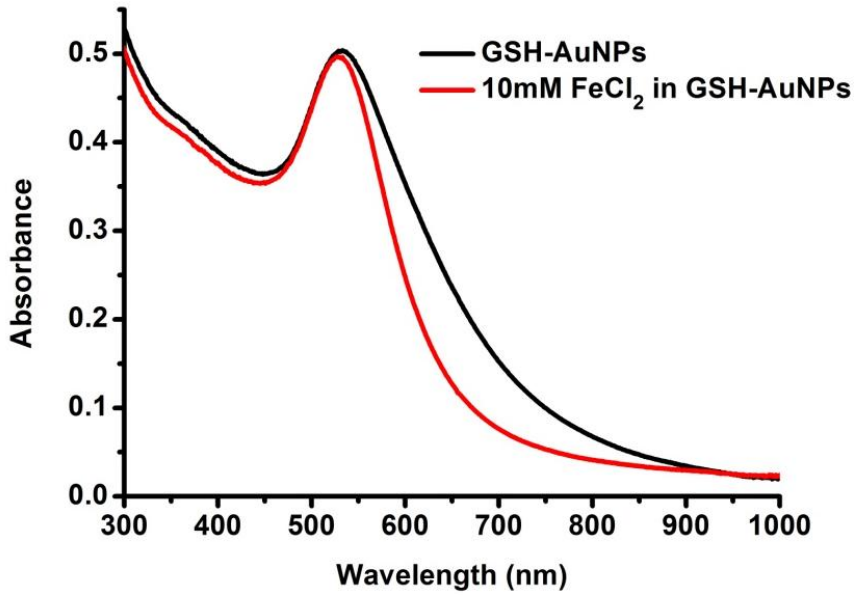

Figure 1.4. The corresponding UV-Vis Absorption spectra of GSH-AuNP solution after the addition of 10 mM $FeCl_2$.

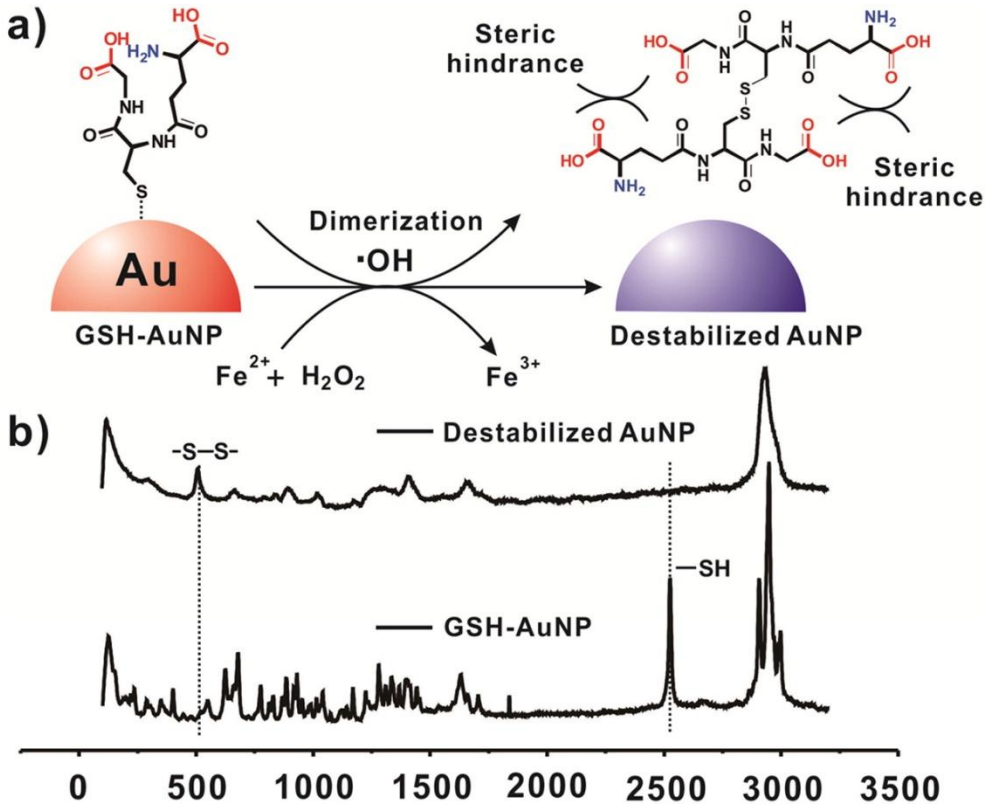

Figure 1.5. Raman spectroscopic study for the destabilization of GSH-AuNPs by the Fenton reaction. (a) Schematic diagram shows the dimerization of glutathione on gold nanoparticle surface after reacting with hydroxyl radicals. (b) The Raman spectra of GSH-AuNPs and destabilized gold nanoparticles

a)

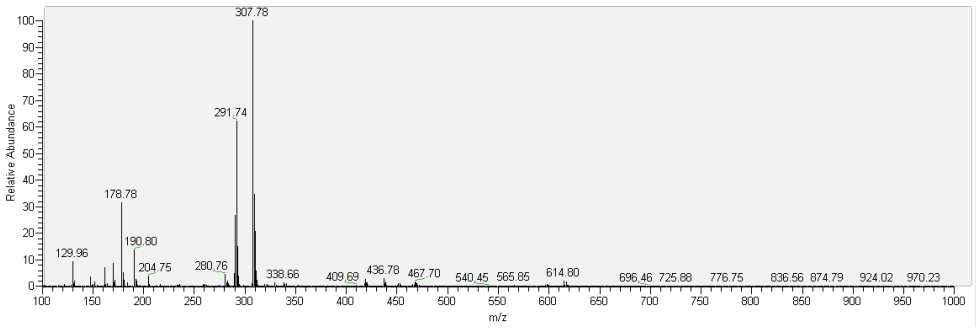

b)

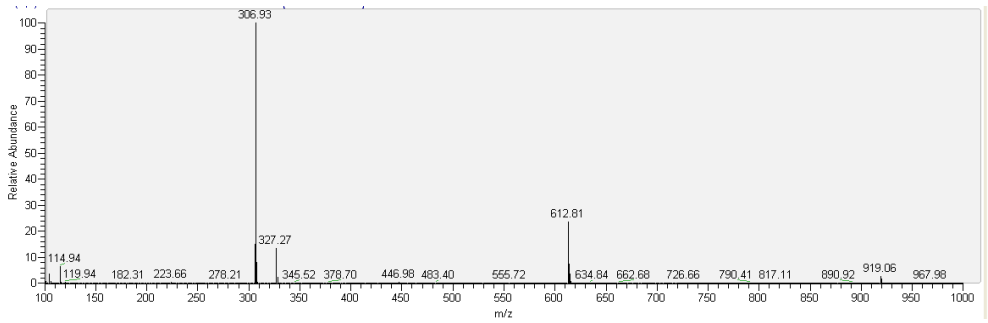

Figure 1.6. ESI-MS spectra of a) aggregated AuNPs with GSSGs (in H_2O) and b) GSH-AuNPs (in H_2O)

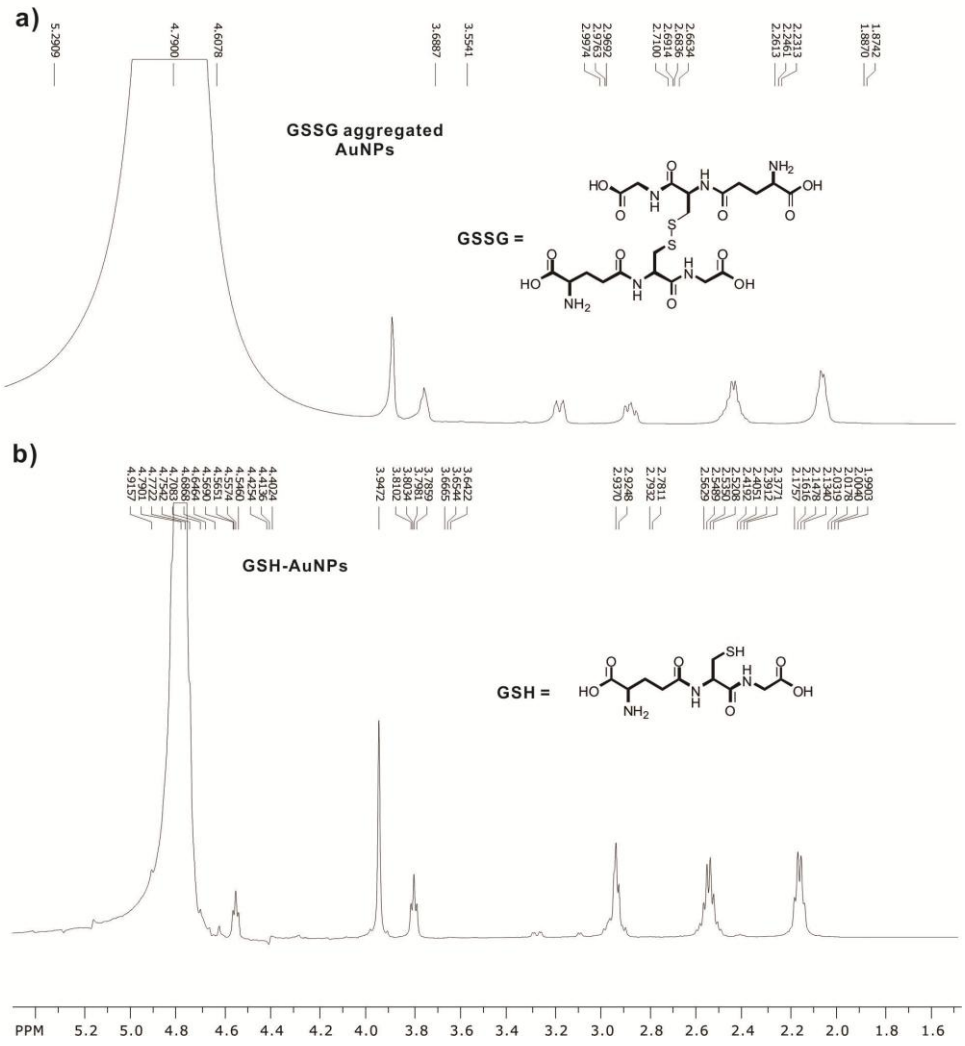

Figure 1.7. ^{1}H NMR (500 MHz) spectra of a) aggregated AuNPs with GSSGs (in D_2O) and b) GSH-AuNPs (in D_2O).

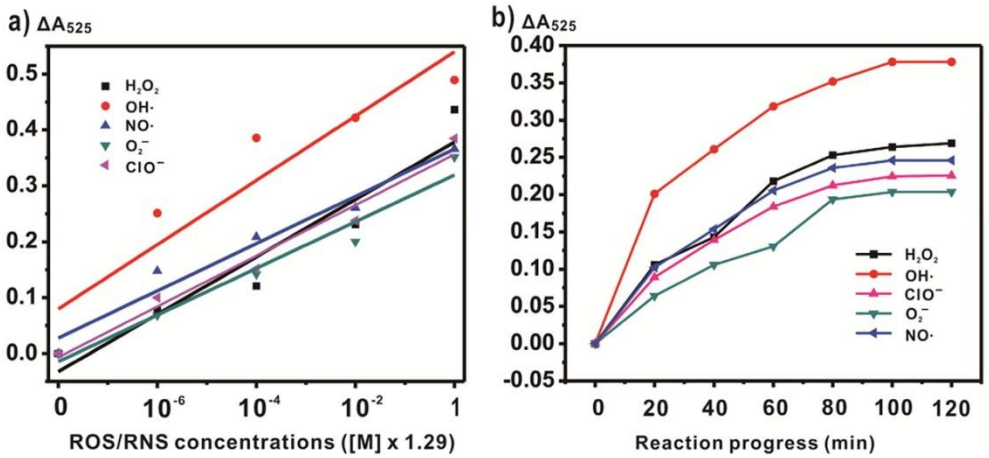

Figure 1.8. (a) Plots of reaction kinetics for change in ΔA_{525} as a function of (a) ROS/RNS concentration upon the treatment with the GSH-AuNPs for 2 h or (b) reaction progress (min) for various ROS/RNS at a constant concentration (1.29 mM) upon the reaction with the GSH-AuNPs.

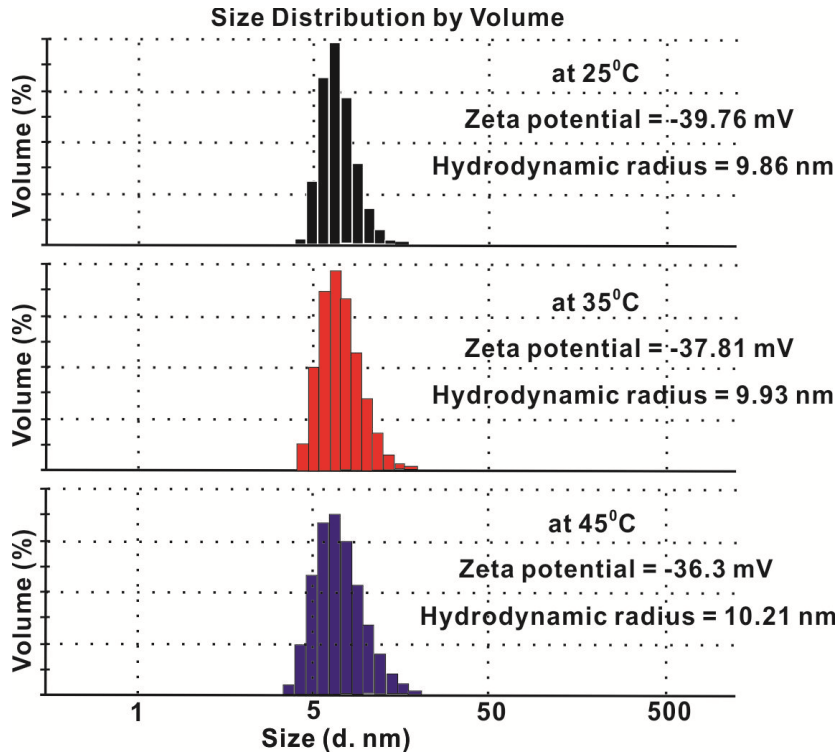

Figure 1.9. The zeta potentials and hydrodynamic radii of the GSH-AuNPs at 25 ℃ and 37 ℃, respectively

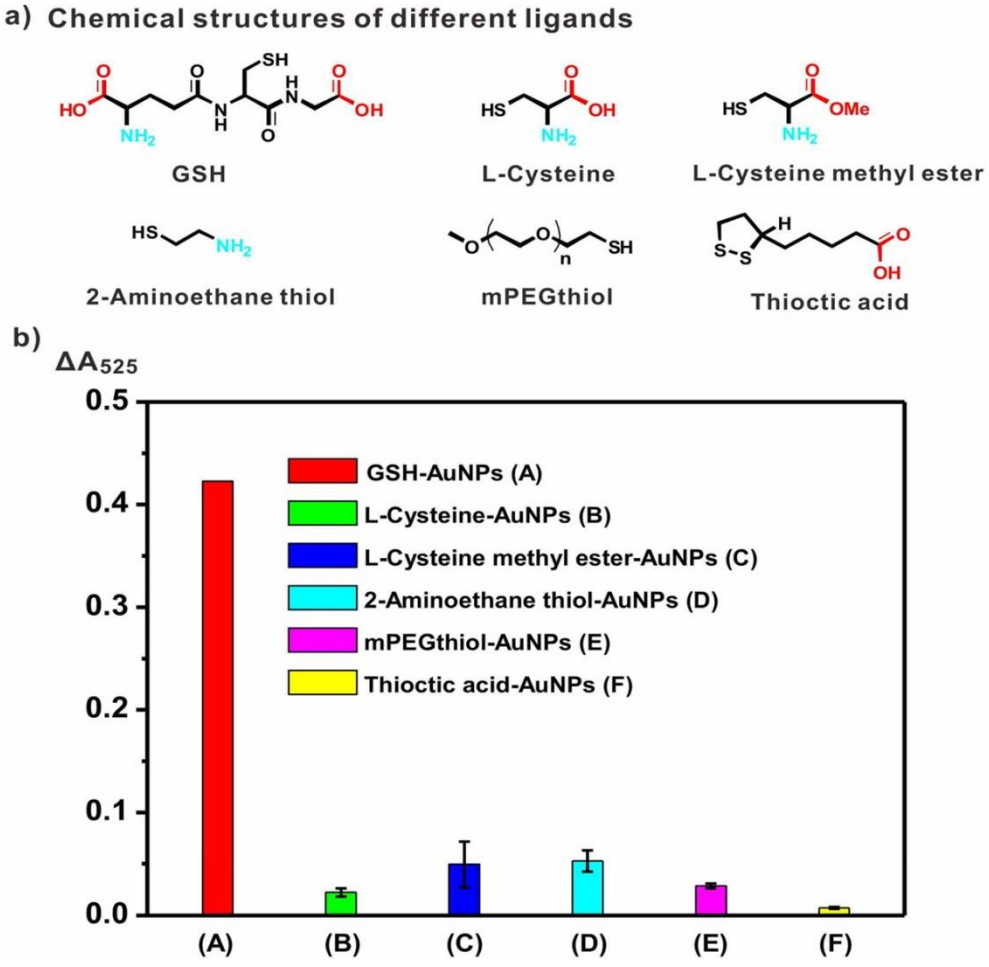

Figure 1.10. Comparison of GSH-AuNPs with other thiolated ligands for H_2O_2 detection: (a) The chemical structures of non-GSH thiolated ligands; (b) ΔA_{525} values for differently functionalized AuNPs upon the treatment with 12.9 mM H_2O_2.

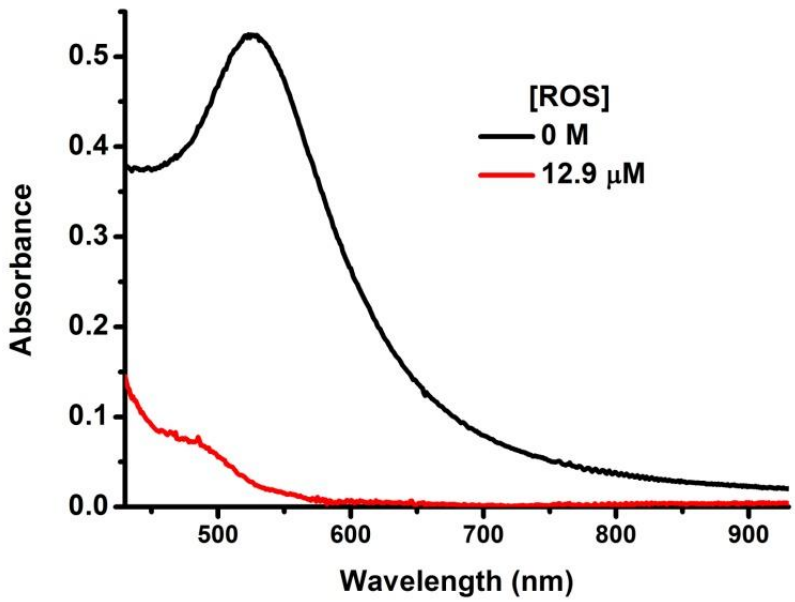

Figure 1.11. The corresponding UV-Vis Absorption spectra of GSH-AuNPs solution after addition of 12.9 mM various type of ROS including H_2O_2, $^{\cdot}OH$, ^{-}OCl, NO and O_2^{-}.

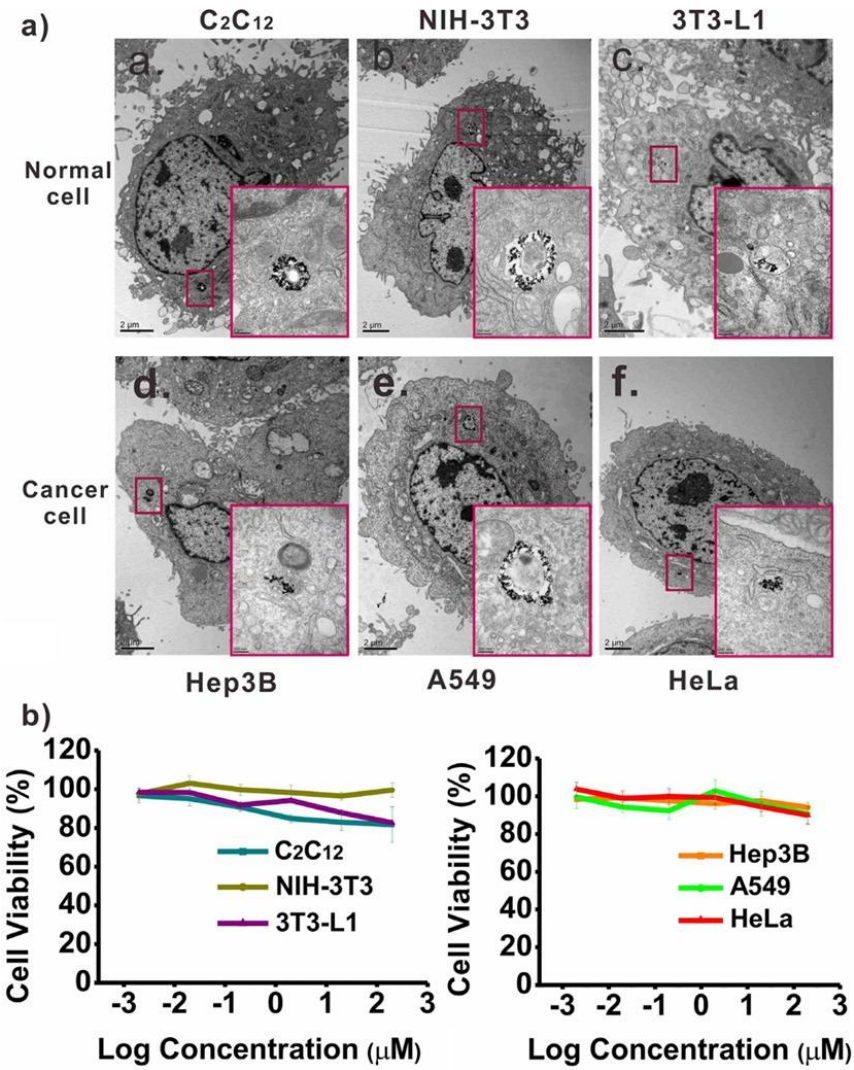

Figure 1.12. GSH-AuNPs with cells. (a) The GSH-AuNP probes are internalized into both normal and cancerous cells. Up taken probes were characterized by the TEM after cell fixation. (b) The cell viability results obtained using the Cell Counting Kit after 2-day incubation with varying concentrations of GSH-AuNP probes. The error bars represent the standard deviations based on three independent measurements.

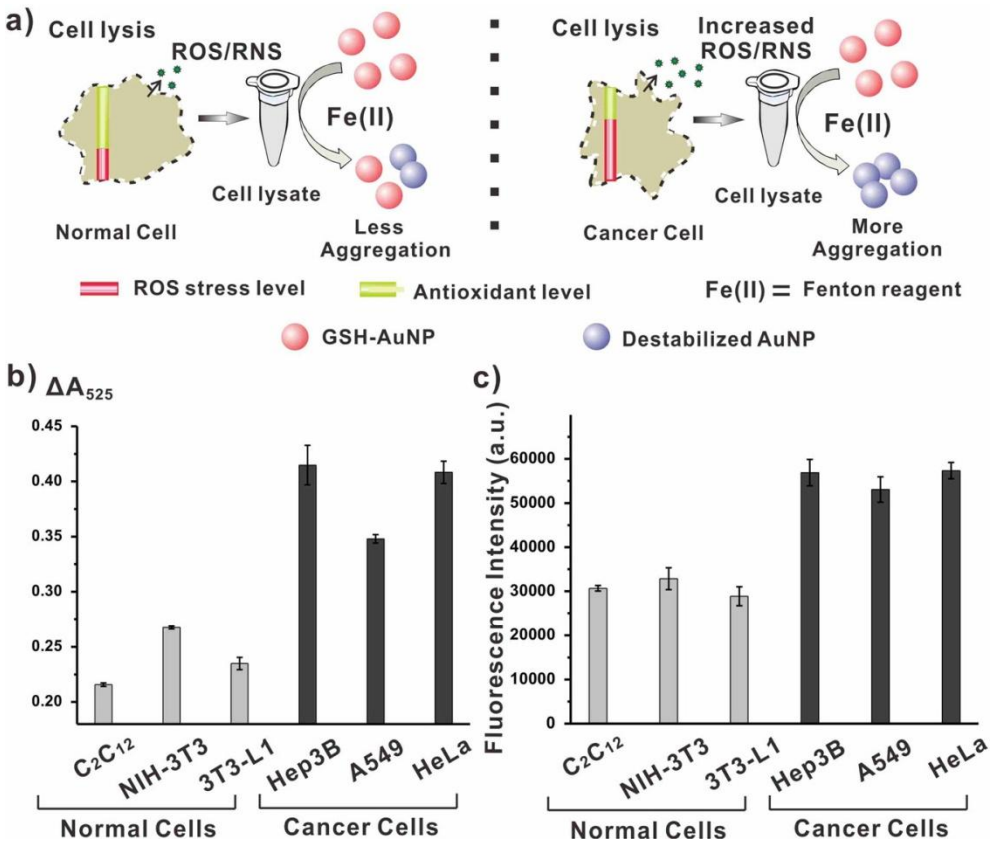

Figure 1.13. (a) Changes in redox balance for normal and cancerous cells and subsequent detection of ROS/RNS from cells using the GSH-AuNP probes. (b) Quantitative comparison of ROS/RNS assay results from various normal and cancerous cells using GSH-AuNPs probes. (c) ROS/RNS assay results from various normal and cancerous cells using a commercially available in vitro ROS/RNS kit. The error bars represent the standard deviations based on three independent measurements.

Tables.

SN	Gold nanoparticles	Ligand structure	Zeta potentials (mV)	Hydrodynamic radius (nm)
1	GSH-AuNPs	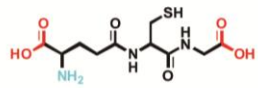	-39.76	9.86
2	2-Aminoethanethiol-AuNPs		40.07	14.47
3	mPEGSH-AuNPs	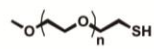	-0.047	22.18
4	Thioctic acid-AuNPs	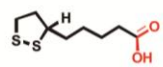	-50.4	11.93
5	L-cysteine-AuNPs	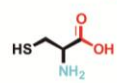	-40.5	8.83
6	L-cysteine methyl ester-AuNPs	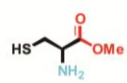	-29.6	9.61

Table 1.1. Chemical structure, zeta potentials and hydrodynamic radius ofdifferent ligands capped AuNPs.

Mouse	Myoblast cell	C_2C_{12}	Normal
	Fibroblast cell	3T3-L1	Normal
	Fibroblast cell	NIH-3T3	Normal
Human	Hepatoma cell	Hep3B	Cancerous
	Lung cell	A549	Cancerous
	Cervical cell	HeLa	Cancerous

Table 1.2. Origin and nature of all kind of cell lines use in this study.

Chapter 2

Core-Satellite Nano-Bio-Hybrids as SERS Based Bioprobes for Distinguishable Imaging of Oxidative and Nitrosative Stress in Living Cells

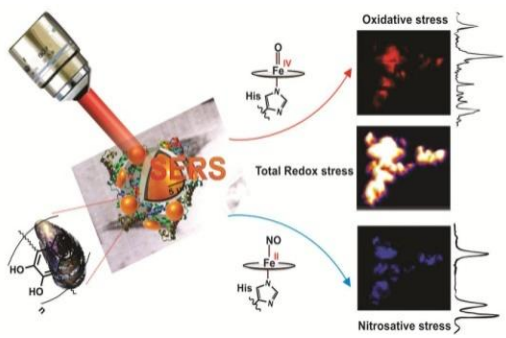

2.1 Introduction.

Understanding the role of endogenous or exogenous reactive oxygen species (ROS) and reactive nitrogen species (RNS) at molecular, cellular and organismal level in a range of physiological processes as well as in the pathogenesis of disorders such as cardiovascular diseases, cancer, diabetes, neurodegenerative diseases and drug-induced hepatotoxicity, is a thrust area of research in redox chemical biology.[1-2] Hydrogen peroxide (H_2O_2) and nitric oxide (NO) are important candidates in the groups of ROS and RNS respectively,[3] often exhibiting interdependent production and roles in the complex signal transduction and oxidative pathways; and also sometimes direct the activation of distinct signalling mechanisms determining the cell fate.[4] An optimum balance in the production of H_2O_2 and NO controls the process of defence against various pathogens and triggers the timely apoptosis.[5] Also, NO can even promote or inhibit cytotoxic activity of H_2O_2 in certain cell models.[6] Simultaneous and distinguishable monitoring of H_2O_2 and NO is crucial to dictating the concerned chemistry and respective downstream biological consequence; providing insight into their inter-relationship in the signal transduction and biochemical pathways. Although, a number of methods have been reported for specific monitoring of H_2O_2 or NO based on mainly fluorescence and other signaling pathways,[7] there are few efforts towards developing single probe for simultaneous detection of both ROS/RNS.[8] Moreover, conventional fluorophores suffer from the disadvantages such as photo-bleaching, low cellular uptake, poor biocompatibility, enzymatic degradation, pH-sensitivity and tedious synthesis.[9] Surface-enhanced Raman scattering (SERS)-based biosensing probes have advantages such as highly sensitive molecular finger-printing, multiplexing, non-invasiveness and easy sampling with practically no interference of water and air for in-vitro and in-vivo

applications.[10] To the best of our knowledge, so far there is no report on biocompatible SERS-based nanoprobe for simultaneous monitoring of ROS and RNS. Among various SERS-active plasmonic nanostructures, core-satellite assemblies have strong potential for SERS-based analysis due to the generation of many electromagnetic 'hot-spot' regions within the single discrete assembly; and plasmonic coupling among core and satellites can be well-controlled based on the interparticle distances.[11] Recently, core-satellite nanostructures have been used for biological delivery/elimination, bioimaging and therapy.[12] It has been demonstrated that high SERS sensitivities can be attained by locating reporter molecules at the interstitial sites of core and satellites (hottest regions).[11j] Heme proteins are biological receptors for ROS/RNS; and different modes of their binding with Fe-porphyrin core triggers different biochemical signals in biological system.[13] Characteristic vibrational frequencies of Fe-porphyrin core in heme proteins are very susceptible to chemical modification by different ROS/RNS, therefore these proteins can serve as sensitive Raman reporters. However, unlike conventional Raman reporters, it is challenging to hybridize biomolecules such as proteins with metal surfaces due to the their susceptibility towards denaturation and conformational changes; which is a 'bottle neck' in using sophisticated plasmonic assemblies for real-life biological applications in spite of their extraordinary SERS enhancement capabilities.[14] Recently, bioinspired coating of polydopamine (pdop) has been demonstrated for nano-bio-interfacing using various nanomaterials due to its highly biocompatible nature and controllable thickness with nanometer precision.[15] Here, we designed a 'core-satellite' plasmonic nano-assembly consisting of large gold nanoparticle (AuNP) as core (80 nm diameter) and small AuNPs as satellites (10 nm diameter), functionalized with myoglobin (Mb) protein with the help of subnanometer thick polydopamine (pdop) spacer between core and

satellites. Mussel-inspired chemistry of biocompatible pdop nanospacer provides a robust anchoring platform for bio-conjugation of Mb protein and subsequent controllable assembly of satellite AuNPs. Intense SERS signals corresponding to characteristic Raman bands of Fe-porphyrin reporter moieties located in 'hot-spot' junctions could be obtained due to extensive plasmonic coupling among core and satellite AuNPs. Our SERS probe was found to be highly sensitive towards exposure of H_2O_2 and NO as distinct Raman signals could be obtained due to the presence of both ROS/RNS. Biological experiments revealed facile internalization of core-shell bioprobes in the living cells and demonstration of excellent biocompatibility. Finally, we were able to quantitatively and distinctly monitor H_2O_2 and NO in normal and cancer cells using our SERS bioprobes.

2.2 Results and Discussion.

First, we performed well-controlled coating of AuNPs (80 nm diameter) with pdop utilizing the Tris-mediated oxidative polymerization reaction of dopamine with modified reaction conditions (Experimental section).[16] The obtained pdop-AuNPs having subnanometer thick pdop layer (from TEM) were characterized by characterized by the transmission electron microscope (TEM), UV–Vis spectrophotometer, dynamic light scattering (DLS) measurement and X-ray photoelectron spectroscopy (XPS) (Figure 2.1, Figure 2.2, Figure 2.3 and see the Experimental section). The localized surface plasmon resonance (LSPR) band of pdop-AuNPs at 539 nm showed a small red-shift (~7 nm) (the LSPR band for citrate-AuNPs is 522 nm; Figure 2.1h). Next, we immobilized Mb on the surface of pdop-AuNPs (80 nm core with ~1 nm pdop thickness) by incubating 100 μL of pdop-AuNPs (10 pM) with 10 uL of aqueous solution of

Mb (0.1 mg/mL) for 10 min at pH 8.5, followed by centrifugation of reaction mixture at 5000 rpm for 5 min and washing with DI water to remove unreacted Mb (Experimental section). Upon Mb-immobilization the hydrodynamic size of pdop-AuNP was increased by 2-3 nm and the pH dependent measurement of zeta potential resulted the pI value to be 5.5 (pI of pdop-AuNPs was 3.5). In this bioconjugation chemistry, at pH 8.5, amine groups present in Mb protein would covalently react with catechol-moieties present in pdop units through Michael-type addition.[17] In the UV/Vis spectrum of Mb-functionalized pdop-AuNPs (Mb-pdop-AuNP), a sharp Soret band at 409 cm^{-1} corresponding to Mb co-existed with consistent LSPR band of AuNP core at 539 nm; however, Q bands (504 and 535 nm) and CT1 band (634 nm) of Mb having relatively low extinction are subsided by LSPR band of Au core (Figure 2.1h).[18] Invariable position of LSPR band even after Mb modification is due to pdop molecular spacer which insulates probable electronic communication between Fe-porphyrin moiety and plasmonic core.[19] Also, no shift in Mb absorption band validates the structural and conformational stability of Mb protein after conjugation with pdop-Au core. This biocompatible behavior of pdop is interesting in the case of delicate proteins such as Mb which have previously shown denaturation upon being in direct contact with metal surfaces.[14] For assembly of small satellite AuNPs around Mb-functionalized core, Mb-pdop-AuNPs were further mixed with 20 μL of bis(p-sulfonatophenyl) phenylphosphine (BSPP) functionalized AuNPs (10 nm) as satellites at pH 5 (pH adjusted with 0.1 M HCl) resulting the core-satellite assembly which were further passivated with thiolated polyethylene glycol (MW 5000) for colloidal stability. UV-Vis spectrum of Mb-immobilized Au core-satellite assemblies showed two bands at 409 nm and 557 nm corresponding to Mb and gold LSPR, respectively and Mb band was slightly red-shifted (by 3 nm) as compared to pure Mb (Figure 2.1h). SEM and TEM images presented in Figure 2.1e-g,

clearly demonstrate the presence of discrete core-satellite assemblies where satellite AuNPs got assembled in high density around large core particle. Average number of satellite particles per core was estimated to be 92, as calculated by UV/Vis spectroscopy (see the Experimental section). Further, the formation of core-satellite plasmonic assembly was directly visualized in the dark-field microscope (Axiovert 200, Carl Zeiss, USA), and the Rayleigh scattering colour images are shown in the insets of Figure 2.1b and 2.1g (full image in Figuure 2.4). The green to orange-red scattering color change was observed when satellite particles were assembled on Au core particles at pH 5, due to the plasmonic couplings between Au core and Au satellite nanoparticles. As a test for SERS activity, a sufficiently de-oxygenated solution of core-satellite assembly was drop-casted on the glass slide and subjected to the Raman spectroscopy using 514 nm laser under argon gas environment (Experimental section). Raman spectrum of met-Mb sandwiched in core-satellite assembly showed typical ν_4 (A_{1g}) vibration band at 1372 cm^{-1} characteristic of six-coordinated high spin (6cHS) state of Mb-Fe^{3+} along with another major bands at 1428, 1485, 1569, and 1624 cm^{-1} corresponding to δ_s (=CH_2), ν_3 (A_{1g}), ν_2 (A_{1g}) and ν (C=C), respectively (Figure 2.5, red spectrum).[20] Intense SERS signals are essentially due to the location of heme units in the electromagnetic hot-spot regions of the plasmonic assembly. In a control experiment, attempt to construct core-satellite assembly without pdop interface was failed as formation of random assemblies of core and satellite particles were observed with subsequent quick denaturation of Mb as studied Raman spectroscopy (Figure 2.5). After having Raman-active core-satellite assembly nanoprobe in our hands, the stage was set to examine it for SERS-based sensing of H_2O_2 and NO as the typical ROS and RNS candidates in aqueous solutions. Mechanistically, reaction of met-Mb with H_2O_2 results the formation of a ferryl

Mb radical cation intermediate which is further oxidized to the Mb-Fe^{4+}=O (Figure 2.6a).[13a, 20] As shown in Figure 2.6b, upon successive addition of H_2O_2 in the solution of core-satellite probe, the ν_4 band and 1372 cm^{-1} gradually shifted to 1386 cm^{-1}, which shows the oxidation of Mb-Fe^{3+} (met-Mb) to Mb-Fe^{4+}=O (Ferryl Mb). Also, δ_s (=CH_2) and ν_3 (A_{1g}) bands of met-Mb are shifted to 1411 cm^{-1} and 1513 cm^{-1} respectively, and the intensity of shifted peaks gradually increased upon increasing the amounts of H_2O_2. Also, the intensity of ν_2 (A_{1g}) band at 1569 cm^{-1} gradually decreased upon successively adding H_2O_2. Such spectral shifts during the oxidation of Mb using H_2O_2 as oxidant is in correlation with previous reports.[21] H_2O_2-mediated chemical transformation of Fe-porphyrin core can also be diagnosed by UV/Vis spectroscopy: there is a clear loss of typical heme intensity at 407 nm after addition of hydrogen peroxide and a lower intensity band at 425 nm along with a shoulder band at 580 nm (probably due to shift in one of the Q bands) is originated as the clear evidence of H_2O_2-mediated heme-oxidation (Figure 2.7).[21a, 22] For RNS testing, required amount of NO was chemically generated (see the Experimental section) and treated with the core-satellite nanoprobe in the presence of sodium dithionite. Sodium dithionite converts met-Mb to deoxy-ferrous-Mb, which provides high affinity towards binding with NO; and stable complex Mb(Fe^{2+}-NO) is formed.[23] As shown in Figure 2.6c, after addition of sodium dithionite original ν_4 band at 1372 cm^{-1} shifts to lower frequency (1354 cm^{-1}) which can be assigned to the deoxy-Mb-Fe^{2+} 5cHS state.[23b] After successive addition of increasing amounts of NO, gradual origin of an overlapping band at 1366 cm^{-1} is observed due to formation of Mb(Fe^{2+}-NO) complex.[24] In Figure 2.6c, simultaneous origin of Raman band at 596 cm^{-1} is due to Fe-NO stretching mode.[24] NO molecule is known to bind with Fe center of heme unit through backbonding utilizing its low-lying π^* orbitals, optimally

matching with filled dπ orbitals of Fe(II).[25] For quantitative SERS-based estimation of H_2O_2, we monitored the SERS intensity change at 1386 cm^{-1} because this band is closely related to the intraporphyrin transitions of the heme group. To do so, the area under the band at 1386 cm^{-1} was deconvoluted, assuming a Lorentzian shape, where the band position and the full widths at half maximum is fixed. As shown in Figure 2.6d, the intensity at 1386 cm^{-1} linearly depends on increasing amounts of H_2O_2 (R^2 = 0.978) with a wide dynamic range (10^{-2} to 10^{-8} M), and limit of detection (LOD) 10 nM could be achieved for H_2O_2. Similarly, upon increasing concentration of NO, there is linear increase in Raman intensity at 596 cm^{-1} (R^2 = 0.964) giving quantitative estimation for NO present in as low as 10 nM concentration. Importantly, when H_2O_2 and NO are taken as equimolar mixture, origin of both distinct diagnostic characteristic bands at 1386 and 596 cm^{-1} corresponding to H_2O_2 and NO respectively, can be observed without any interference; and intensity of both bands increases with increase in amounts of both ROS/RNS. Evidence for Fe(III)-NO complex formation was also achieved by UV/Vis spectrum, where a clear red-shift in Soret band by 15 nm and origin of a shoulder band at 580 nm due to red-shifted Q band was observed (Figure 2.7).[23a] Such multiplexing capability of our core-satellite nanoprobe gives opportunity for simultaneous quantitative characterization of both ROS/RNS. As shown in Figure 2.6e, reaction of H_2O_2 and NO exhibits very fast kinetics as it takes ~8 min for reaching reaction equilibrium for both ROS/RNS. Due to wide dynamic range and fast detection kinetics, our nanoprobe would be helpful as remote optical sensor for studying abnormal cells where ROS/RNS level is usually in micromolar range, as well as to monitor ROS/RNS at very low concentrations in normal cells and other ex-vitro biological systems. After establishing high SERS sensitivities of core-satellite nanoprobe for H_2O_2 and NO, our next goal was to test its potential for SERS-based monitoring and

quantifying intracellular ROS and RNS in normal and cancer cells. Measurement of 'oxidative stress' due to increased metabolic activity and mitochondrial malfunction in cancer cells can be used as diagnostic hallmark for differentiating cancer cells from normal cells.[2] Also, distinct quantitative monitoring of H_2O_2 and NO will be useful for biochemical understanding of the role of each of these two important ROS/RNS constituents in the genesis of 'oxidative stress' condition. First, we conducted the cellular uptake experiments of the core-satellite nanoprobes with four different cell lines (normal cells: NIH3T3 and C_2C_{12}; cancerous cells: A549 and HeLa). Same number of all cells (1×10^4) was treated with equal amounts of core-satellite nanoprobes for two hours and locations of the particles were confirmed by TEM images of fixed cells (Experimental section). As shown in Figure 2.9a-d, core-satellite nanoprobes were found to be inside cells encapsulated in endosomes without entering in to nuclei of the cells in all four cases. Efficiency of cellular uptake of nanoprobes was estimated to be 55-62% for all four cell lines as determined by ICP-AES data (Figure 2.9e-f). Such high cellular internalization efficiency of core-satellite nanoprobes is crucial for intracellular probing of ROS/RNS. We believe biocompatible polyethylene glycol passivation of core-satellite nanoprobes avoids hindrance from negatively charged cellular membrane during receptors-mediated endocytosis. As shown in Figure 2.9g, our core-satellite nanoprobes were found to be highly biocompatible as indicated by the results obtained from cytotoxicity test with different cell lines treated with wide concentration range of particles (31 nM to 1 μM) for two days; over 90% cells survived (for details see the Experimental section). Thereafter, nanoprobe-treated all four normal and cancer cell lines were subjected to SERS-mapping at 1386 cm^{-1} as diagnostic peak for H_2O_2 and at 596 cm^{-1} as diagnostic peak for NO using 514 nm laser (Figure 2.10a). As shown in Figure

2.10b-e, Raman images are well-correlated with bright field and dark-field microscope images in all four cases. Dark-field images of cells treated with nanoprobes clearly exhibited stronger light-scattering as compared to untreated cells (Figure 2.10b-e). Comparison of Raman maps obtained for normal cells and cancer cells clearly indicated higher and densely located pixel-intensities of corresponding colors (red for H_2O_2 and blue for NO) in the case of cancerous cells as compared to normal cells (Figure 2.10b-e). Quantitative estimation of amounts of H_2O_2 and NO obtained in correlation with intensities of Raman peaks at 1386 cm^{-1} and 596 cm^{-1}, recorded at three different places in the cell clearly demonstrate cancer cells produced up to 60 % more H_2O_2 and NO as compared to normal cells. Total redox level imaging can also be obtained having rich quantitative features by integrating Raman maps obtained corresponding to H_2O_2 and NO as shown in Figure 2.10g with the help of imageJ program; total redox level is clearly quantitatively higher in the case of cancerous cells as compared to normal cells. In order to further validate our results, a commercially available fluorescence signal based in vitro ROS/RNS assay (OxiSelect, Cell biolabs, INC., San Diego, CA, USA) was also conducted and the results were compared to our SERS based nanoprobe (for details see the Experimental section).[26] Importantly, the ROS/RNS detection results from the commercial assay showed a very similar pattern as observed in our SERS based assay results (Figure 2.11). Interestingly, total amount of ROS/RNS after laser irradiation (514 nm, 8 min) for SERS imaging was slightly more than the total amount of ROS/RNS measured before laser irradiation.

2.3 Experiment Section.

1. Materials and Instruments.

All the materials were used as received without any further purification. Dopamine·HCl was purchased from Sigma-Aldrich (USA). Gold nanoparticles were purchased from BBInternational (USA). Hydrochloric acid and sodium hydroxide were purchased from Daejung Chemicals and Metals (Korea). Tris was purchased from USB Corporation (USA). The formvar/carbon-coated copper grids were purchased from Ted Pella, Inc. (USA). Nanopure water (18.0 MΩ-cm) was used for all experiments. The UV-Vis spectra were obtained from a UV-Vis spectrophotometer (Agilent 8453 spectrophotometer, USA). Elemental analysis and binding energy measurements were performed using the X-ray photoelecton spectroscope (Axis HSi, KRATOS Analytical). The dynamic light scattering measurements were performed using Malvern Zetasizer (Nano ZS). TEM images were obtained using the Energy-Filtering Transmission Electron Microscope (LIBRA 120, Carl Zeiss) with an accelerating voltage of 120 kV. SEM images and EDS-elemental mapping data were obtained using the Field-Emission Scanning Electron Microscope (SUPRA 55VP, Carl Zeiss). The Raman spectra were acquired using Renishaw inVia Raman Microscope equipped with 514 nm, 633 nm and 785 nm laser sources.

2. Methods.

Polydopamine (pdop) coating on 80-nm gold nanoparticles (Figure 2.1).

1 mL of commercially available colloidal solution of 80-nm citrate-stabilized AuNPs (cit-AuNPs) (11 pM) was centrifuged and re-dispersed in Tris·HCl buffer (pH 8.5, 10 mM). 2 μL solution (5 mg/mL) of dopamine·HCl in Tris·HCl buffer (pH 8.5, 10 mM) was then added, and the reaction mixture was vortexed at 25 ˚C for 4 h. Finally, the reaction mixture was centrifuged at 8000 rpm for 5 min, and the supernatant was removed. The sediment containing pdop-AuNPs

was then re-dispersed in DI water. The thickness of the pdop layer on 80-nm Au core was estimated to be ~1 nm from the TEM analysis.

Synthesis of bis(p-sulfonatophenyl)phenyl phosphine (BSPP)-functionalized AuNPs (BSPP-AuNPs).

BSPP-AuNPs (10 nm in AuNP diameter) were prepared by a ligand-exchange reaction. 10 mL colloidal solution of commercially available cit-AuNPs (11 nM) was added 2 mg of BSPP, and the reaction solution was stirred overnight (12 h) at 25 °C. After the reaction, the excess BSPP was removed by centrifugation and washing with DI water.

Myoglobin conjugation with pdop-AuNP followed by synthesis of Au core-satellite nanoassemblies.

First, we immobilized Myoglobin on the surface of pdop-AuNPs (80 nm core with ~1 nm pdop thickness) by incubating 100 μL of pdop-AuNPs (10 pM) with 10 μL of aqueous solution of Mb (0.1 mg/mL) for 10 min at pH 8.5, followed by centrifugation of reaction mixture at 5000 rpm for 5 min and washing with DI water to remove unreacted Myogolobin. For assembly of small satellite AuNPs around Mb-functionalized core, Mb-pdop-AuNPs were further mixed with 20 uL of bis(p-sulfonatophenyl) phenylphosphine (BSPP) functionalized AuNPs (10 nm) as satellites at pH 5 (pH adjusted with 0.1 M HCl) resulting the core-satellite assembly.

Quantification of the number of satellites per core by the UV–Vis spectroscopy.

After the core-satellite assembly at pH 5, the mixture was centrifuged and the UV–Vis spectrum of the supernatant was recorded to estimate the remaining number of BSPP-AuNPs in the supernatant. The average number of BSPP-

AuNPs per pdop-AuNP was calculated using the following formula:

$$\text{Average number of satellites per core} = \frac{(N_{sat})_{initial} - (N_{sat})_{final}}{N_{core}}$$

$(N_{sat})_{initial}$ = Number of satellites in the supernatant, calculated from UV-vis data before assembly

$(N_{sat})_{final}$ = Number of satellites in the supernatant, calculated from UV-vis data after assembly at pH 3

N_{core} = Number of core particles used in the reaction

It should be noted that, under the centrifugation condition used herein (5,000 rpm for 5 min), only pdop-AuNPs and larger core-satellite assemblies were precipitated without the co-precipitation of small BSPP-AuNPs.

Dark-Field Microscopy of Pdop-AuNPs and Au core-satellite Nanoprobes.

Properly cleaned glass-slides were treated with 2% (v/v) aqueous solution of 3-aminopropyl-trimethoxysilane (APTS) for 10 seconds, followed by washing with DI water and drying under nitrogen. Thereafter, 10 μL of a sample (pdop-AuNP or CPN) was loaded on the APTS-treated glass slide and sandwiched with another thinner glass slide to make a sample ready for the dark-field microscopy. The dark-field images were obtained with the Carl Zeiss (DE/Axiovert 200) microscope (Figure 2.4).

Cell Culture and Treatment with Au Core-satellite Nanoprobes

Cells (C_2C_{12}, NIH-3T3, A549 and HeLa) were suspended in a 96-well plate to a concentration of 104 cells/mL in Dulbecco's modified Eagle's medium (DMEM, 50 μL in each well) with 10% fetal bovine serum (FBS), and 1% antibiotic solution (GIBCO, Invitrogen, Karlsruhe, Germany), and cultured at 37 °C and 5% CO_2, overnight. The culture medium was then replaced with freshly prepared

DMEM. Then, different concentrations of Au core-satellite nanoprobe solution in PBS were added and the cells were left in the culture chamber for 2 hours.

Dark-Field Imaging of Live Cells

All cell lines were cultured onto 35 mm polylysine-modified glass bottom culture dishes (MatTek Corp., USA) and allowed to grow in DMEM medium supplemented with 10 % fetal bovine serum and 1% antibiotics (37 °C, 5 % CO_2) for overnight. Next, the medium was replaced with fresh culture medium containing nanoprobes and cells were further incubated for 2 hours. Thereafter, glass slide was washed with PBS to remove excess nanoprobes and the dark-field images were obtained with the Carl Zeiss (DE/Axiovert 200) microscope.

Cell Cross-Section Imaging Using the Transmission Electron Microscopy.

For cell cross-section imaging, nanoprobe incubated cells were first detached from the well plate. After a wash with PBS, at least 5 x 10^5 cells were fixed for 2 h with modified Karnovsky's fixative (2 % paraformaldehyde and 2 % glutaraldehyde in 0.05 M sodium cacodylate buffer, pH 7.2). After three washings with 0.05 M sodium cacodylate buffer (pH 7.2) at 4 °C, cells were fixed with 1 % osmium tetroxide in 0.05 M sodium cacodylate buffer (pH 7.2) for 2 h and then washed with distilled water two times. Fixed cells were En bloc stained at 4 °C for overnight using 0.5 % uranyl acetate and then dehydrated with a graded concentration series of ethanol (30 %, 50 %, 70 %, 80 %, 90 %, 100 %, 100 %, and 100 % ethanol; 10 min for each dehydration step). Infiltrated cells using propylene oxide and Spurr's resin were polymerized at 70 °C for 24 h. Various sections of the resin block were cut using the ultramicrotome (MT-X, RMC, Tucson, AZ, USA) and stained 2 % uranyl acetate

and Reynolds' lead citrate for 7 min, followed by transferring the section of interest onto a 300 mesh copper TEM grid.

Toxicity Assay.

The cytotoxicity of various concentrations of CPNs was evaluated using the Cell Counting Kit (CCK-8, Dojindo lab., Japan). Cells were grown in a 96-well plate in 100 μL of DMEM supplemented with FBS. After 24 h seeding, cells were incubated with various concentrations (from 100 pM to 1 μM) of nanoprobes for 48 h, and cell viability assay was carried out. The metabolic activity of the cells was measured using CCK-8 (a sensitive colorimetric assay for the determination of the number of viable cells after incubating with probes). Then, 10 uL of the CCK-8 solution was directly added to the incubated cells in each well. After 2 h incubation at 37 °C, the amount of formazan dyes, generated by dehydrogenased of active cells, was measured by a microplate reader (Anthos 2010, Anthos Labtec, Eugendorf, Austria).

Commercial in Vitro ROS/RNS Assay.

To validate our GSH-AuNP based cell assay results, the results from commercially available OxiSelect In Vitro ROS/RNS Assay Kit were compared. The Oxi-Select assay is a fluorescence-based method in which fluorescence intensity is proportional to the total ROS/RNS level within the sample. This assay utilizes a proprietarily quenched fluorogenic probe, dichlorodihydrofluorescin DiOxyQ (DCFH-DiOxyZ), which can specifically detect ROS/RNS. The DCFH-DiOxyZ can be transformed to the highly reactive fluorescence-quenched DCFH form, and the quenched fluorescence signal from the DCFH can be turned on upon ROS/RNS detection. The same number of cells (5 x 10^5 cells) was used for all the experiments after cell detachment

from the culture dish and cell lysis. Next, 50 μL of cell lysate was added to a 96-well plate (30096, SPL lifescience, Gyeonggi-Do, South Korea), suitable for fluorescence measurement. DCFH can be highly reactive to ROS/RNS by mixing 50 μL of catalystwith 100 μL of the DCFH solution (DCFH-DiOxyQ, priming reagent and stabilization solution with the recommended ratio by the manufacturer). After 45 min incubation at room temperature with gentle shaking, the fluorescence signal, which is proportional to the ROS/RNS level, can be obtained using a fluorescence plate reader (The SynergyHT, BioTek, VT, USA) with 480 nm excitation and 530 nm emission.

Procedure for NO generation and its use.

NO was in situ prepared by reduction of dilute nitric acid with copper: 8 HNO_3 + 3 Cu → 3 $Cu(NO_3)_2$ + 4 H_2O + 2 NO in concentrations ranging from 0 to 10 mM. The solutions was then quickly added to Au core-satellite nanoprobe solution.

Procedure for Raman imaging of live cells.

All cell lines were cultured onto 35 mm polylysine-modified glass bottom culture dishes (MatTek Corp., USA) and allowed to grow in DMEM medium supplemented with 10 % fetal bovine serum and 1 % antibiotics (37 °C, 5 % CO_2) for overnight. Next, the medium was replaced with fresh culture medium containing SERS nanoprobes and cells were further incubated for 2 hours. Thereafter, glass slide was washed with PBS to remove excess nanoprobes. SERS mapping experiments were performed with a Renishaw InVia Raman microscope system with a laser beam directed to the sample through a 50× objective lens. The samples were excited with a 514 nm laser with a focal spot of 1 μm and 1.5 mW/μm^2 power, and the mapping measurements at 1386

cm^{-1} and 596 cm^{-1} were carried out as raster scans in 1 μm steps over the specified area (approx. 30 x 30 μm^2) with 1 s as the integration time per step.

2.4 Conclusion

In conclusion, we have devised a plasmonic core-satellite assembly equipped with Mb as dual responsive Raman tag for SERS-based distinguishable monitoring of ROS and RNS in living cells. In the SERS-bioprobe fabrication, pdop plays a crucial role as biomolecule-immobilizer interface and subnanometer thick spacer for efficient plasmonic coupling between core and satellites eventually responsible for high SERS efficiency of Raman probe. Uniformity and stability of core-satellite assembly are responsible for reproducible and quantitative Raman signaling. Current method paves the path of sophisticated hot plasmonic assemblies to be used for clinical and redox biological applications helpful in unravelling the etiology and pathophysiology of many diseases involving alterations of oxidative and nitrosative stress such as cancer, neurological disorders, pancreatic malfunction and inflammatory diseases.

2.5 References

1. a) B. D. Autréaux, M. B. Toledano, Nat. Rev. Mol. Cell Biol. 2007, 8, 813-824; b) N. Bashan, J. Kovsan, I. Kachko, H. Ovadia, A. Rudich, Physiol. Rev. 2009, 89, 27-71; c) A. N. Pandey, A. Tripathi, K. V. PremKumar, T. G. Shrivastav, S. K. Chaube, J. Cell. Biochem. 2010, 111, 521-528; d) F. Peyrot, C. Ducrocq, J. Pineal Res. 2008, 45, 235-246;

2. a) M. Valko, D. Leibfritz, J. Moncol, M. T. Cronin, M. Mazur, J. Telser, Int. J. Biochem. Cell Biol. 2007, 39, 44-84; b) C. C. Winterbourn, Nat. Chem. Biol. 2008, 4, 278-286; c) N. Caporaso, J. Natl. Cancer Inst. 2003, 95, 1263-1265; d) D. Galaris, V. Skiada, A. Barbouti, Cancer Lett. 2008, 266, 21-29; e) M. T. Lin, M. F. Beal, Nature 2006, 443, 787-795; f) J. S. Walsh, G. T. Miwa, Annu. Rev. Pharmacol. Toxicol. 2011, 51, 145–167; g) S. Russmann, G. A. Kullak-Ublick, I. Grattagliano, Curr. Med. Chem. 2009, 16, 3041–3053.

3. a) S. G. Rhee, Science 2006, 312, 1882-1883; b) M. Reth, Nat. Immun. 2002, 3, 1129-1134; c) E. W. Miller, B. C. Dickinson, C. J. Chang, Proc. Natl. Acad. Sci. U.S.A. 2010, 107, 15681-15686; d) A. Soneja, M. Drews, T. Malinski, Pharmacol. Rep. 2005, 57 (suppl) 108– 119; e) W. K. Alderton, C. E. Cooper, R. G. Knowles, Biochem. J. 2001, 357, 593-615; f) S. P. L. Cary, J. A. Winger, E. Derbyshire, M. A. Marletta, Trends Biochem. Sci. 2006, 31, 231-239.

4. a) J.-H. Li, Plant. Physiol. 2009, 114-124; b) S. A. Milligan, M. W. Owens, M. B. Grisham, Am. J. Physiol. - Lung Cell 1996, 271, L114– L120; c) H. Eguchi, N. Fujiwara, H. Sakiyama, D. Yoshihara, K. Suzuki, Neurosci. Lett. 2011, 494, 29- 33; d) H. K. Lum, Y. K. C. Butt, S. C. L. Lo, Nitric Oxide 2002, 205– 213. e) J. L. Sartoretto, H. Kalwa, M. D. Pluth, S. J. Lippard, T. Michel, Proc. Natl. Acad. Sci. U.S.A. 2011, 108, 15792-15797; f) G. P. Meares, D. Fontanilla, K. A. Broniowska, T. Andreone, J. R. Lancaster Jr., J.A. Corbett, Am. J. Physiol. Endocrinol. Metab. 2013, 67, E614–E622.

5. T. Wei, C. Chen, J. Hou, W. Xin, A. Mori, Biochim. Biophys. Acta 2000, 1498, 72-79.

6. a) Y. Yoshioka, T. Kitao, T. Kishino, A. Yamamuro, S. Maeda, J. Immunol. 2006, 176, 4675-468; b) J. G. Filep, C. Lapierre, S. Lachance, J. S. Chan., Biochem. J. 1997, 321, 897-901; c) U. Rauen, T. Li, I. Ioannidis, H. de Groot, Am. J. Physiol. Cell. Physiol 2007, 292, C1440– C1449; d) R. Farias-Eisner, J. Biol. Chem. 1996, 271, 6144-6151; e) L. A. Ridnour, Free Radical Biol. Med. 2005, 38, 1361-1371; f) S. Kotamraju, Y. Tampo, A. Keszler, C. R. Chitambar, J. Joseph, A. L. Haas, B. Kalyanaraman, Proc. Natl. Acad. Sci. U.S.A. 2003, 100, 10653-10658; g) H. K. Lum, Y. K. C. Butt, S. C. L. Lo, Nitric Oxide 2002, 205– 213.

7. a) E. W. Miller, C. J. Chang, Curr. Opin. Chem. Biol. 2007, 11, 620–625; b) X. Chen, X. Tian, I. Shin, J. Yoon, Chem. Soc. Rev. 2011, 40, 4783–4804; c) L. E. McQuade, S. J. Lippard, Curr. Opin. Chem. Biol. 2010, 14, 43–49. d) R. Gill, L. Bahshi, R. Freeman, I. Willner, Angew. Chem., Int. Ed. 2008, 120, 1676–1679. e) N. L. Rosi, C. A. Mirkin, Chem. Rev. 2005, 105, 1547–1562.

8. a) S. Kumar, W.-K. Rhim, D.-K. Lim, J.-M. Nam, ACS Nano 2013, 7, 2221-2230; b) L. Yuan , W. Lin, Y. Xie, B. Chen, S. Zhu, J. Am. Chem. Soc. 2012, 134, 1305–1315; c) T. Guo, L. Cui, J. Shen, R. Wang, W. Zhu, Y. Xu, X. Qian, Chem. Commun.2013, 49, 1862-1864; d) A. J. Shuhendler, K. Pu, L. Cui, J. P. Uetrecht, J. Rao, Nature Biotechnology 2014, 32, 373–380; e) Y. Wang, J.-M. Noël, J. Velmurugan, W. Nogala, M. V. Mirkin, C. Lu, M. G. Collignon, F. Lemaître, C. Amatore, Proc. Natl. Acad. Sci USA 2012, 109, 11534-11539.

9. a) L. L. del Mercato, A. Z. Abbasi, M. Ochs, W. J. Parak, ACS Nano 2011, 5, 9668–9674; b) O. Kreft, A. M. Javier, G. B. Sukhorukov, W. J. Parak, J. Mater. Chem. 2007, 17, 4471–4476.

10. a) Y. Wang, B. Yan, L. Chen, Chem. Rev. 2013, 113, 1391-1428; b) K. Kneipp, H. Kneipp, I. Itzkan, R. R. Dasari, M. S. Feld, Chem. Rev. 1999, 99, 2957-2976. c) C. W. Freudiger, W. Min, B. G. Saar, S. Lu, G. R. Holtom, Science 2008, 322, 1857-1861; d) K. Meister, J. Niesel, U. Schatzschneider, N. Metzler-Nolte, D. A. Schmidt, M. Havenith, Angew. Chem. Int. Ed. 2010, 49, 3310-3312; e) P. Rivera_Gil, C. Vazquez-Vazquez, V. Giannini, M. P. Callao, W. J. Parak, M. A. Correa-Duarte, R. A. Alvarez-Puebla, Angew. Chem. Int. Ed. 2013, 52, 13694 –13698; f) Y. Shen, F. Xu, L. Wei, F. Hu, W. Min, Angew. Chem. Int. Ed. 2013, ASAP (DOI: 10.1002/ange.201310725); g) M. Okada, N. I. Smith, A. F. Palonpon, H. Endo, S. Kawata, M. Sodeoka, K. Fujita, Proc. Natl. Acad. Sci. USA 2012, 109, 28-32.

11. a) B. M. Ross, J. R. Waldeisen, T. Wang and L. P. Lee, Appl. Phys. Lett. 2009, 95, 193112; b) N. Gandra, S. Singamaneni, Chem. Commun. 2012, 48, 11540-11542; c) I. Choi, H. D. Song, S. Lee, Y. I. Yang, T. Kang and J. Yi, J. Am. Chem. Soc. 2012, 134, 12083-12090; c) J. R. Waldeisen, T. Wang, B. M. Ross and L. P. Lee, ACS Nano 2011, 5, 5383-5389; d) D. S. Sebba, J. J. Mock, D. R. Smith, T. H. LaBean and A. A. Lazarides, Nano Lett. 2008, 8, 1803-1808; e) X. Xu, N. L. Rosi, Y. Wang, F. Huo and C. A. Mirkin, J. Am. Chem. Soc. 2006, 128, 9286-9287; f) L. Xu, H. Kuang, C. Xu, W. Ma, L. Wang and N. A. Kotov, J. Am. Chem. Soc. 2012, 134, 1699-1709; g) Y. Zheng, T. Thai, P. Reineck, L. Qiu, Y. Guo and U. Bach, Adv. Funct. Mater. 2013, 23, 1519-1526; h) J. A. Fan, Y. He, K. Bao, C. H. Wu, J. M. Bao, N. B. Schade, V. N. Manoharan, G. Shvets, P. Nordlander, D. R. Liu and F. Capasso, Nano Lett.

2011, 11, 4859– 4864; i) F. Huo, A. K. R. Lytton-Jean and C. A. Mirkin, Adv. Mater. 2006, 18, 2304–2306; j) N. Gandra, A. Abbas, L. Tian and S. Singamaneni, Nano Lett., 2012, 12, 2645– 2651; k) M. Gellner, D. Steinigeweg, S. Ichilmann, M. Salehi, M. Schütz, K. Kömpe, M. Haase and S. Schlücker, Small 2011, 7, 3445-3451; j) J. H. Yoon, J. Lim and S. Yoon, ACS Nano 2012, 6, 7199-7208; k) W. Xie, B. Walkenfort and S. Schlücker, J. Am. Chem. Soc. 2013, 135, 1657-1660; l) J. B. Lassiter, H. Sobhani, J. A. Fan, J. Kundu, F. Capasso, P. Nordlander and N. J. Halas, Nano Lett. 2010, 10, 3184–3189; m) B. Luk'yanchuk, N. I. Zheludev, S. A. Maier, N. J. Halas, P. Nordlander, H. Giessen and C. T. Chong, Nat. Mater. 2010, 9, 707–715.

12. Y. T. Leo Chou, Kyrl Zagorovsky and Warren C. W. Chan Nat. Nanotech. 2014, 9, 148-155.

13. a) M. P. Richards, Antioxid. Redox Sign. 2013, 18, 2342-2351.; b) U. Flögel, M. W. Merx, A. Gödecke, U. K. M. Decking, J. Schrader, Proc. Natl. Acad. Sci. USA 2001, 98, 735-740; c) H. M. Girvan, A. W. Munro, J. Biol. Chem. 2013, 288,13194-13203. d) M. K. Chan, Curr. Opin. Chem. Biol. 2001, 5, 216-222; e) P. George, D. H. Irvine, Nature 1951, 168, 164-165; f) W. Chen, S. Cai, Q.-Q. Ren, W. Wen, Y.-D. Zhao, Analyst 2012, 137, 49–58.

14. M. Feng, and H. Tachikawa, J. Am. Chem. Soc., 2008, 130, 7443-7448.

15 a) C.-Y. Chien, W.-B. Tsai, ACS Appl. Mater. Interfaces 2013 ASAP (DOI: 10.1021/am401071f); b) R. Ogaki, D. T. Bennetsen, I. Bald, M. Foss, Langmuir 2012, 28, 8594– 8599; c) K. Sun, Y. Xie, D. Ye, Y. Zhao, Y. Cui, Y. F. Long, W. Zhang, X. Jiang, Langmuir 2012, 28, 2131–2136; d) S. Ho, S. H.

Yang, S. M. Kang, K.-B. Lee, T. D. Chung, H. Lee, I. S. Choi, J. Am. Chem. Soc. 2011, 133, 2795–2797.

16. a) H. Lee, S. M. Dellatore, W. M. Miller, P. B. Messersmith, Science 2007, 318, 426-430; b) B. Fei, B. Qian, Z. Yang, R. Wang, W. C. Liu, W. C. Mak, J. H. Xin, Carbon 2008, 46, 1792–1828; c) L. Q. Xu, W. J. Yang, K.-G. Neoh, E.-T. Kang, G. D. Fu, Macromolecules 2010, 43, 8336–8339.

17. a) D. R. Dreyer, D. J. Miller, B. D. Freeman, D. R. Paul, C. W. Bielawski, Langmuir, 2012, 28, 6428– 6435; b) C.-T. Chen, V. Ball, J. J. de Almeida Gracio, M. K. Singh, V. Toniazzo, D. Ruch, M. J. Buehler, ACS Nano 2013, 7, 1524-1532.

18. a) L. Tofani, A. Feis, R. E. Snoke, D. Berti, P. Baglioni, G. Smulevich, Biophys. J. 2004, 87, 1186-1195; b) S. Franzen, S. G. Boxer, J. Biol. Chem. 1997, 272, 9655-9660.

19. M. Lee, J. U. Kim, J. S. Lee, B. I. Lee, J. Shin, C. B. Park, Adv. Mater. 2014, ASAP, (DOI: 10.1002/adma.201305766).

20. a) B. J. Reeder, Antioxid. Redox Signal. 2010, 13, 1087-1123; b) B. J. Reeder, D. A. Svistunenko, C. E. Cooper, M. T. Wilson, Antioxid. Redox Signal. 2004, 6, 954-966.

21 a) X. X. Han, A. M. Schmidt, G. Marten, A. Fischer, I. M. Weidinger, P. Hildebrandt, ACS Nano 2013, 7, 3212-3220; b) A. J. Sitter, C. M. Reczek, J. Terner, Biochim Biophys Acta., 1985, 828, 229-235; c) S. Hu, K. M. Smith, T. G. Spiro, J. Am. Chem. Soc. 1996, 118, 12638-12646.

22. a) C. Giulivi, E. Cadenas, Free Radical Biol. Med. 1998, 24, 269–279. b) A. I. Alayash, B. A. B. Ryan, R. F. Eich, J. S. Olson, R. E. Cashon, J. Biol. Chem. 1999, 274, 2029-2037.

23. a) F. B. Jensen, J. Exp. Biol. 2007, 210, 3387-3394; b) F. Guo, X. X. Xu, Z. Sun, J. X. Zhang, Z. X. Meng, W. Zheng, H. M. Zhou, B. L. Wang, Y. F. Zheng, Colloids Surf., B 2011, 86, 140–145.

24. a) A. V. Soldatova, M. Ibrahim, J. S. Olson, R. S. Czernuszewicz, T. G. Spiro, J. Am. Chem. Soc. 2010, 132, 4614–4625; b) R. F. Eich, T. Li, D. D. Lemon, D. H. Doherty, S. R. Curry, J. F. Aitken, A. J. Mathews, K. A. Johnson, R. D. Smith, G. N. Phillips, Jr., J. S. Olson, Biochemistry 1996, 35, 6976–6983.

25. V. K. K. Praneeth, F. Paulat, T. C. Berto, S. DeBeer George, C. Nather, C. D. Sulok, N. Lehnert, J. Am. Chem. Soc. 2008, 130, 15288–15303.

26. A. S. Keston, R. Brandt, Anal. Biochem. 1965, 11, 1-5.

27. a) G. Pasparakis, Small 2013, 9, 4130–4134; b) L. Minai, D. Yeheskely-Hayon, D. Yelin, Sci. Rep. 2013, 3, 2146.

2.5 Figures.

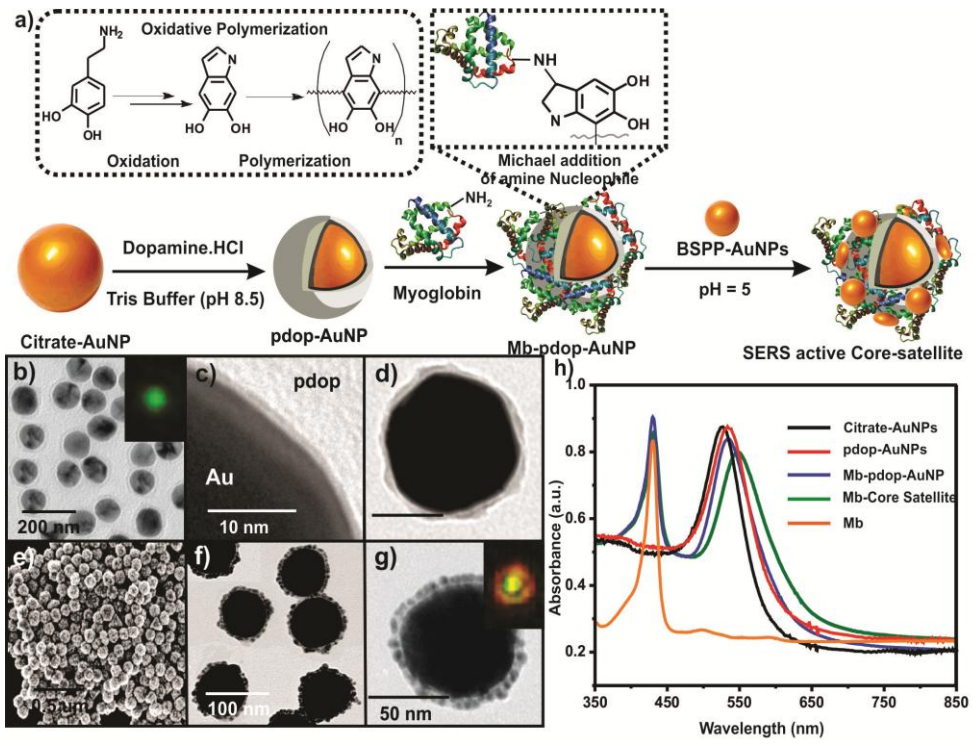

Figure 2.1. (a) Schematic representation for synthesis of Mb-functionalized core-satellite bioprobe. (b-c) TEM images of pdop-AuNPs. (d) TEM image of Mb-functionalized pdop-AuNP. (e) SEM image of core-satellites . (f-g) TEM images of core-satellites. (h) UV/Vis spectra of citrate-AuNPs, pdop-AuNPs, Mb-functionalized pdop-AuNPs, core-satellite assembly and Mb. (Insets of Fig. 1b and 1g are corresponding actual dark-field light scattering images of the particle)

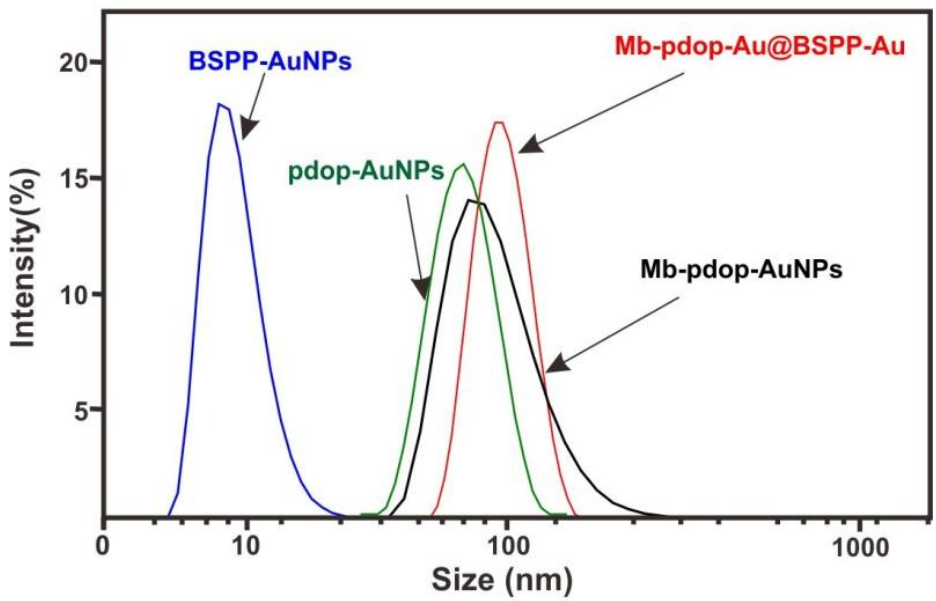

Figure 2.2. The corresponding hydrodynamic size data from the dynamic light scattering measurements.

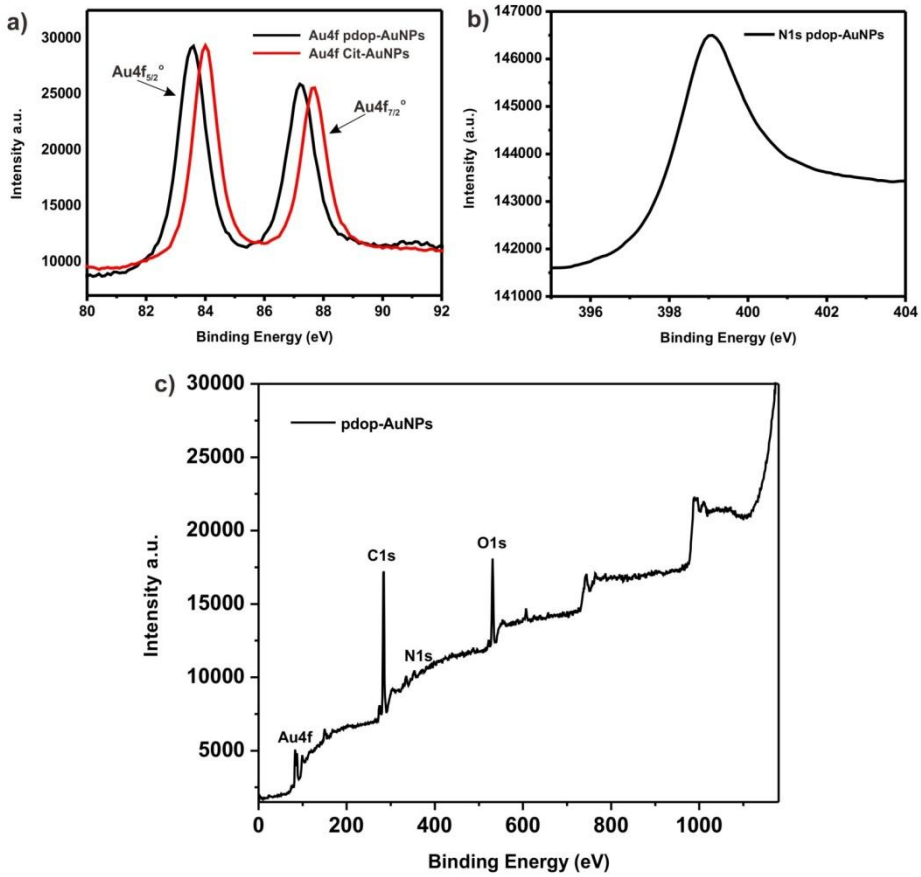

Figure 2.3. The XPS analysis of pdop-AuNPs (80-nm core). a) Comparison between Au 4f peaks in pdop-AuNPs and citrate-AuNPs. (b) High resolution N 1s peak. (c) The XPS survey spectrum of pdop-AuNPs.

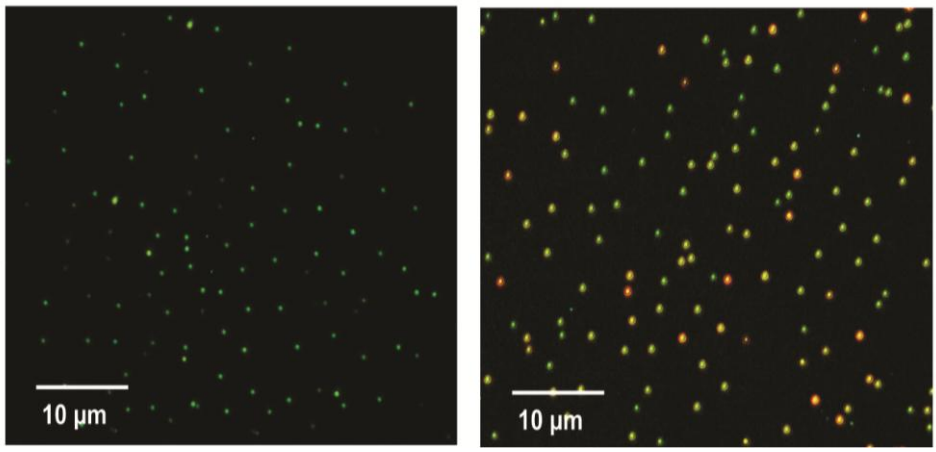

Figure 2.4. The dark-field microscopy images of AuNPs (80 nm) and core-satellite nanoprobes respectively.

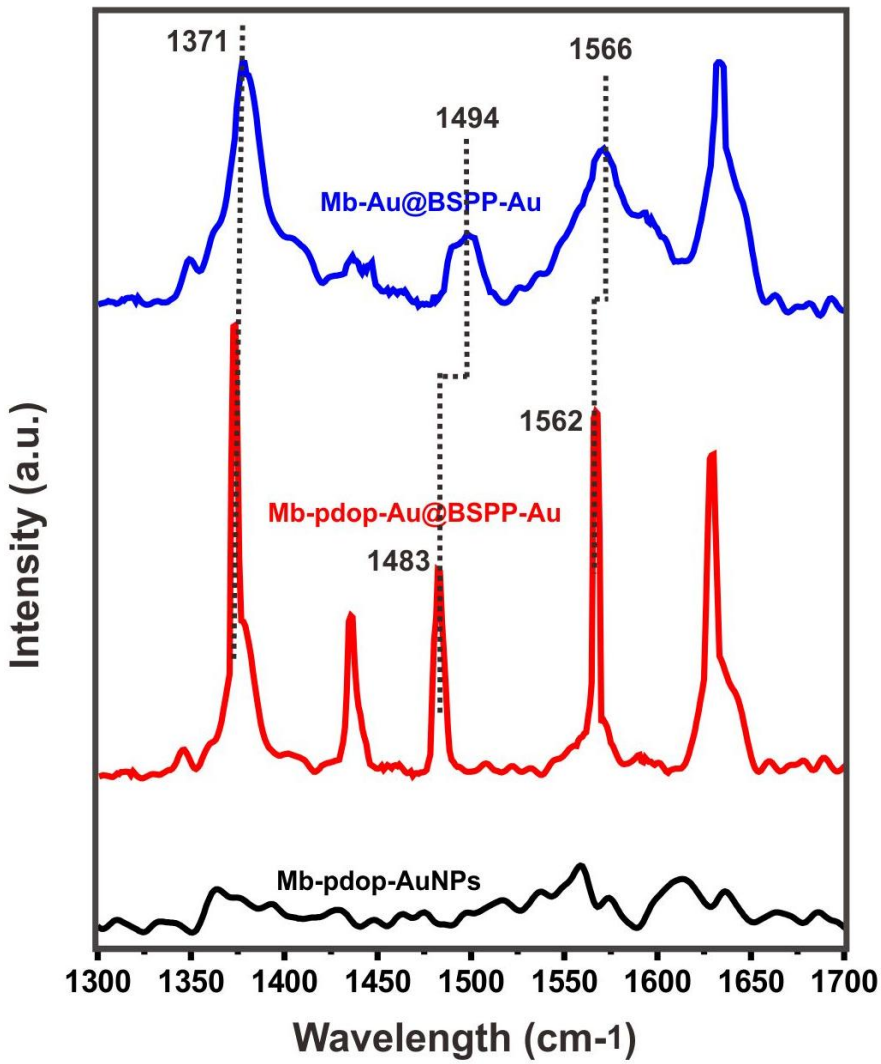

Figure 2.5. Comparison of characteristic Raman peaks of Mb with and without the use of pdop spacer.

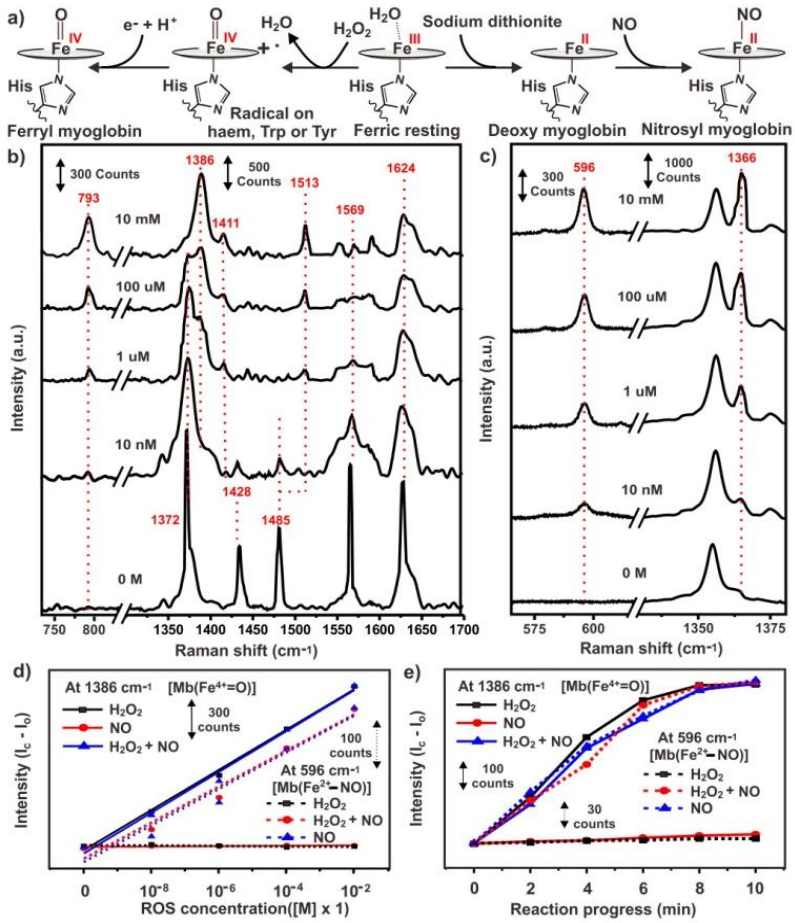

Figure 2.6. (a) Schematic representation for expected structural changes in heme group present in core-satellite nanoprobe upon reaction with H_2O_2 and NO. (b-c) Raman spectra obtained after exposure of core-satellite nanoprobe with different concentrations of H_2O_2 and NO. (d) Plots of changes in intensities of Raman peaks at 1386 cm^{-1} and 596 cm^{-1} after exposing core-satellite nanoprobes with different concentrations of H_2O_2, NO and their equimolar mixtures. (e) Plots of changes in intensities of Raman peaks at 1386 cm^{-1} and 596 cm^{-1} after exposing core-satellite nanoprobes with H_2O_2, NO and their equimolar mixtures at different times

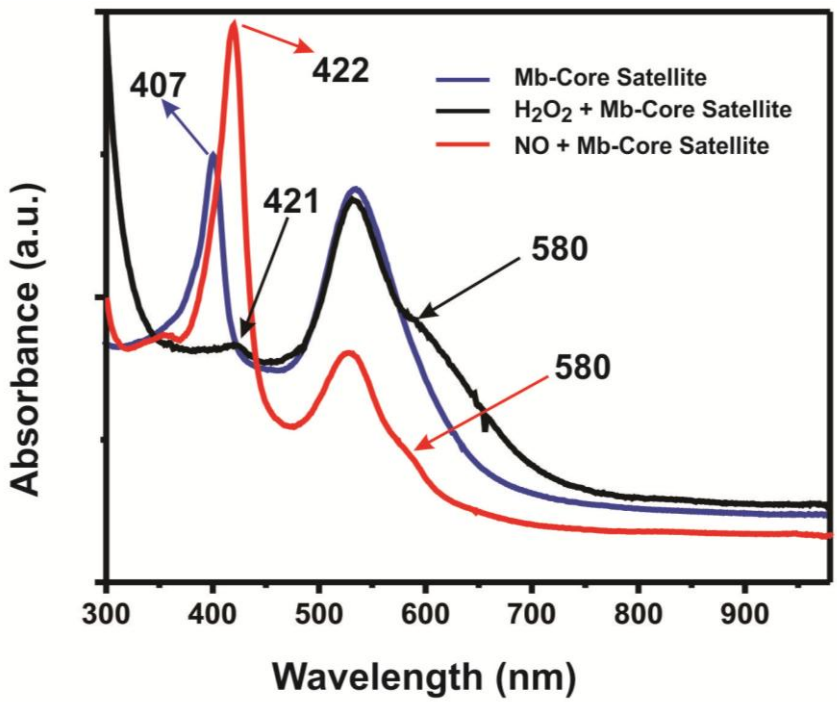

Figure 2.7. UV/Vis spectra of Mb-core satellite nanoprobe before and after addition of H_2O_2 and NO.

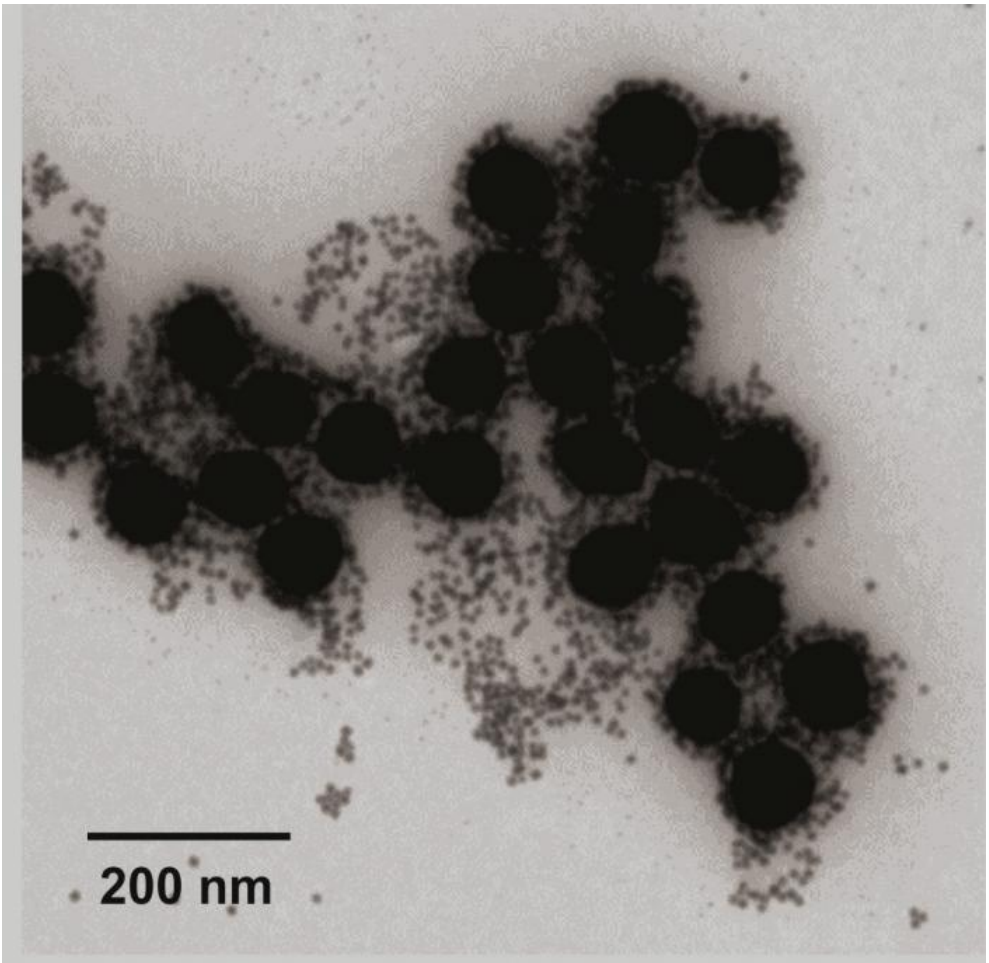

Figure 2.8 TEM image of core satellite structures without pdop**.**

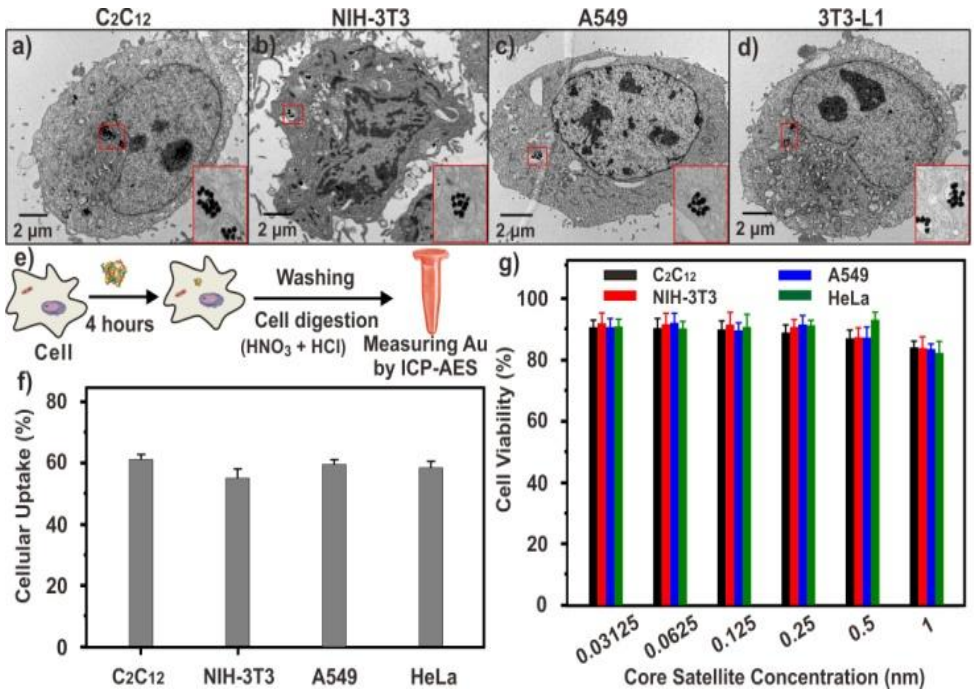

Figure 2.9. Core-satellite nanoprobes with cells. (a) TEM images of normal and cancer cells after core-satellite nanoprobe internalization followed by cell fixation. (b) Schematic for estimation of gold amount by ICP-AES after core-satellite internalization. (c) % cellular uptake of core-satellite nanoprobes calculated from ICP-AES data for all cells. (d) Cell viability results for all four different cells obtained using the cell counting kit after 2-day incubation with varying concentrations of core-satellite AuNP probes. The error bars represent the standard deviations based on three independent measurements.

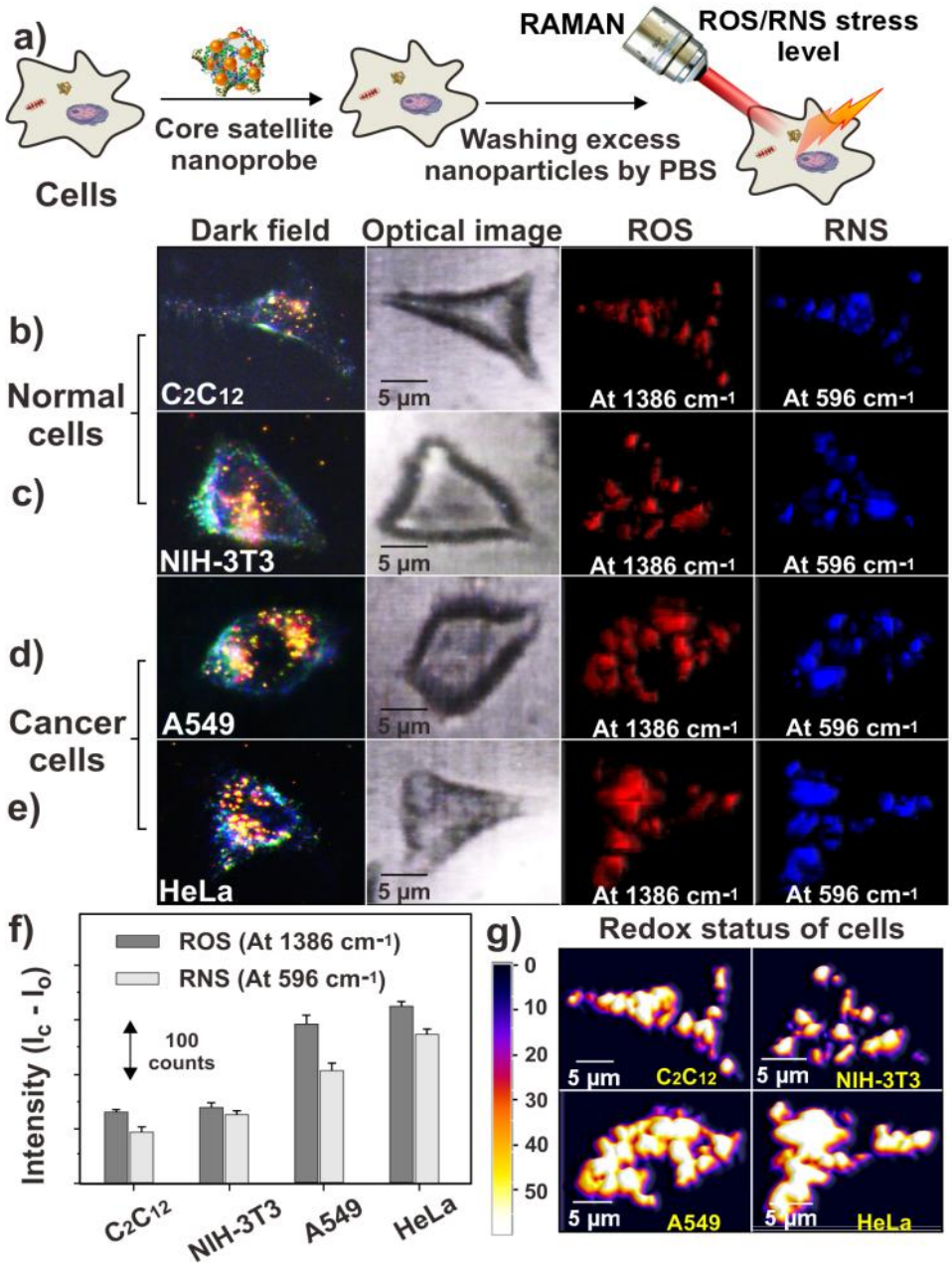

Figure 2.10. a) Schematic representation for ROS/RNS monitoring using core-satellite nanoprobes. b) dark-field image, bright-field image, Raman mapping image corresponding to the band at 1386 cm^{-1} for ROS measurement and

Raman mapping image corresponding to the band at 596 cm^{-1} for RNS measurement in normal and cancer cells (left to right). c) Change in Raman intensities at 1386 cm^{-1} and 596 cm^{-1} for normal and cancerous cells. d) Contour Raman maps corresponding to bands at 1386 and 596 cm^{-1} as the representation of total amount of ROS and RNS in normal and cancerous cells.

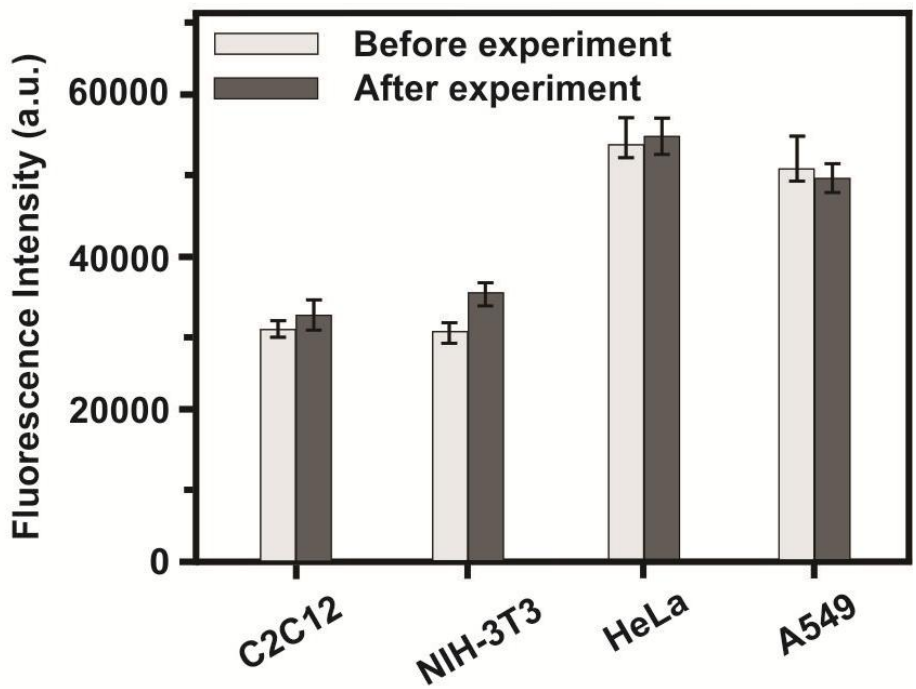

Figure 2.11. Total ROS/RNS estimated from commercial assay in different cell lines before and after experiment

Chapter 3

Oxidative Nano-Peeling Chemistry-Based Controlled Synthesis of Plasmonic Nanocore-Petal Nanostructures and Their Applications in Photothermal and Photodynamic Cancer Cell Therapeutics

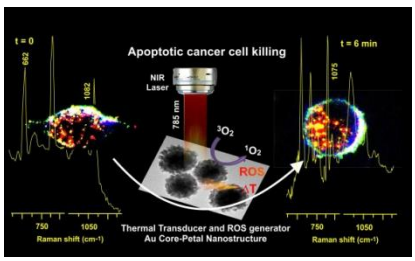

3.1 Introduction.

Plasmonic metal nanostructures have been drawing enormous attention for their potential use in biosensing, bioimaging and therapeutic applications.[1-6] Near-infrared (NIR) light-mediated photo-therapeutic approaches with these plasmonic nanostructures, viz. photodynamic therapy (PDT)[7-8] and photothermal therapy (PTT)[4-6], have shown promising advantages including high spatial resolution, improved target selectivity, reduced side effects, non-invasiveness without a need for surgery, fast and effective treatment and low cost over conventional cancer therapies. PDT involves the use of an organic photosensitizer (PS) molecules which convert normal tissue oxygen ($^3O_2$) to very reactive and cytotoxic singlet oxygen ($^1O_2$) with the site-selective exposure of light of a suitable wavelength.[7] For a highly efficient PDT, light wavelength needs to match with the maximum absorption wavelength of a PS within the NIR region (700-1100 nm; phototherapeutic NIR window to avoid the interference with blood and tissue).[9] Unfortunately, most of the therapeutic PS molecules absorb light in the visible region and are prone to photodecomposition under long-term light exposure,[10-11] and prolonged PDT treatment creates severe local hypoxia by depletion of tissue oxygen and hampering further PDT operation.[12-13] On the other hand, PTT method is involved with plasmonic nanoparticles such as gold nanoparticles (AuNPs) that induce hyperthermia and/or subsequent generation of small shock waves induced by exposure of continuous wave or pulse laser, resulting in the apoptotic or necrotic cancer cell death depending on the extent of increase in the local temperature.[4-6] The efficient hyperthermal necrotic destruction of cancer cells involves very high temperature (>70 °C),[14] causing collateral damage to healthy cells and also rendering undesirable, uncontrollable reshaping of nanostructures.[15-16] For less invasive apopotic cancer cell death, it

is desirable to use low-temperature (<45 °C) PTT strategy. However, PTT operation even at benign temperature could render thermal stress in cancer cells while pursuing apoptosis, and, under a prolonged treatment condition, cancer cells can acquire transient resistance hampering the further treatment.[17] For these reasons, there have been emerging efforts towards the development of PDT-PTT integrated platforms that involve visible/NIR light-absorbing hybrid nanostructures between PTT-active structures such as Au nanoflowers, Au nanorods, Au nanocages and nano-graphene oxide and PDT-active structures, and these hybrid nanostructures allow the use of moderate hyperthermia along with ROS-mediated intracellular damage.[18-24] There are still several challenges, including mismatch between the absorption wavelengths of PS and plasmonic nanostructure, energy transfer between PS and nanostructure, the requirement of lower operation temperature or non-thermal treatment, toxicity of nanostructures and complex conjugation chemistry, that need to be addressed for the full utilization of these hybrid nanostructure-based approach. In particular, an effective photothermal nanostructured transducer should have high optical absorption cross-section and is biocompatible, easily synthesizable with high structural precision and synthetic yield and plasmonically tunable in the NIR region.[25-32] Further, there have been no effort towards exploring ROS generation capability of NIR-active plasmonic nanostrucutures in combination with their inherent hyperthermic effect for potential continuous wave–based NIR laser cancer phototherapy without the need for additional organic PS molecules.

Branched plasmonic nanostructures such as nanostars, nanoflowers and nanolaces can form strong electromagnetic fields inside particles due to their closely positioned and coupled sharp edge structures. These strong plasmonic couplings and large surface area are useful features for surface-enhanced

Raman scattering (SERS), photothermal conversion and catalysis.[33-38] These branched plasmonic nanostructures could be good candidates for PDT and PTT substrates, but the solution-phase large-scale synthesis of such anisotropically growing branched Au nanostructures with high structural precision and controllability is challenging due to the high diffusion coefficient and face-centered cubic faceting tendency of Au atoms.[39,40] The anisotropic growth of these nanobranches can seldom occur when the reaction is kinetically controlled and the growth of high-energy facets is faster than low-energy facets. Further, it is tedious, complicated and very difficult to optimize such reaction conditions with varying surfactants in order to produce structurally reproducible homogeneous nanostructures in a large number.[33,39-44]

Here, we introduce the oxidative nano-peeling chemistry of polydopamine (pdop) for the controlled growth and synthesis of plasmonic nanobranch structures of tunable size and density on the surface of pdop-coated spherical AuNPs, and the thermoplasmonic property-based multi-functionalities of these Au core-petal nanoparticles (CPNs) were explored for the plasmonic imaging with the dark-field microscopy and SERS spectroscopy and PDT-PTT dual therapeutic applications (Figure 3.1a). The pdop layer can be stably and uniformly assembled on Au core surface,[45-48] and Au(III)-induced oxidation of the catechol moieties of pdop triggers the disassembly of pdop on AuNP core and facilitates the anisotropic structural growth of petal nanostructures with various protrusion lengths and densities. The CPNs with different branching morphologies are highly controllable and exhibit wide optical spectra from visible to NIR region depending on the protrusion length and density of the petals. The local photothermal heating of 0.5 nM CPNs with densely protruded petals in aqueous solution to 53.7 ˚C was achieved within 6 min with 785-nm laser of 2 W/cm^2, and it was also observed that $^1O_2$ in aqueous solution was generated during this process. We further studied CPNs for their photo-

therapeutic potential using human cervical cancer cells (HeLa cells). It was confirmed by the dark-field microscopic imaging and TEM that CPNs were efficiently taken up by HeLa cells in a large numbers (up to 1260 particles per cell; 10^4 cells were measured) within 2 h, and these CPNs displayed no cytotoxicity. Upon the exposure to 785-nm laser for 6 min, as high as 95 % HeLa cells were killed at a benign temperature (~42 °C). Such an efficient killing of cancer cells at a relatively low temperature is due to the synergistic combination of the photothermal effect and the plasmonic 'hot-electron'-assisted intracellular ROS generation. We also explored the intracellular structural and biochemical changes after photo-therapeutic treatment of cancer cells in order to obtain a mechanistic insight in cell death. The transmission electron microscopic (TEM) analysis of the fixed cells and nuclei-targeting dye-staining assay revealed the severe damages of cellular membrane and apoptotic morophology change of cells. A myriad of plasmonically coupled local hot spots inside AuCPs allowed for SERS-based monitoring of ROS-mediated changes in DNA, and the results show that the oxidation and denaturation of DNA were triggered by the exposure of the cells with CPNs to 785-nm laser.

3.2. Results and Discussion.

In a typical experiment, commercially available citrate-stabilized AuNPs (80 nm in diameter) were treated with dopamine•HCl in 10 mM Tris•HCl buffer at pH 8.5 for 4 h at room temperature to form 5-nm pdop-coated AuNPs (pdop-AuNPs) [Figure 3.1b; see the Experimental section for more details]. The localized surface plasmon resonance (LSPR) band of pdop-AuNPs at 531 nm showed a small red-shift (~9 nm) (the LSPR band for citrate-AuNPs = 522 nm), possibly due to the charge transfer between AuNP and pdop.[48] The pdop

coating on AuNPs was also confirmed by X-ray photoelectron spectroscopy (XPS) (Figure 3.2). When the high resolution Au 4f XPS spectra between pdop-AuNPs and citrate-AuNPs were compared, the 0.4 and 0.8 eV shifts of binding energies that correspond to Au 4f5/2 (83.6 eV) and Au 4f7/2 (87.1 eV), respectively, were observed (Figure 3.2). These data further support the binding of the catechol groups to AuNP surface.[49-51] In the presence of polymerization initiators (Tris) under alkaline conditions, dopamine was transformed to 5,6-dihydroxyindolines, their dione derivatives and other related molecules and these are closely packed due to strong supramolecular forces such as charge transfer, π-π stacking and hydrogen bonding to form the pdop layer on AuNPs.[52-55] For the synthesis of CPNs from pdop-AuNPs, 5 mL of 1 nM pdop-AuNP solution, 100 μL of $HAuCl_4$ (5 mM), 100 μL of PVP (5% w/v, 10,000 MW) and 100 μL of hydroxyl amine (50 mM) were added consecutively and the reaction mixture was rigorously shaken for 5 min at 25 °C. The solution exhibited a gradual solution color change from red to blue, and the resulting blue-colored solution was stable for weeks, as confirmed by UV/Vis spectroscopy and TEM without showing any aggregation and change in color. The electron microscopic images of the sample revealed the formation of highly branched CPNs with closely positioned plasmonic petals around spherical Au core (Figure 3.1c-d). The Raman spectra of pdop-AuNPs before and after $HAuCl_4$ treatment revealed the diminishing catechol peak at 1617 cm^{-1} and the enhancement in quinone peak at 1651 cm^{-1} (Figure 3.3). $HAuCl_4$-mediated oxidation of catechol to quinone was also confirmed by ^{13}C NMR where the signals at 142.9 ppm and 143.7 ppm due to catecholic carbons diminished in intensities while the intensities of quininonic carbon signals at 182.0 ppm 183.7 ppm increased (Figure 3.4).[52] These suggest that the oxidations of catechols to quinones caused the disruption of the hydrogen bonds between catechol and

quinone groups of pdop oligomers and the breakdown of the bonds between the catechols and AuNP to result in the disassembly or 'nanopeeling' of the pdop oligomers on AuNP core (Figure 3.1a). In a control experiment, we reacted citrate-stabilized 80-nm AuNPs with $HAuCl_4$ and NH_2OH under the same conditions that were applied for the synthesis of CPNs from pdop-AuNPs. No protruding nanobranches were observed, and increase in the diamer of spherical AuNPs from 80 to 83 nm was observed. By simply varying the amount of $HAuCl_4$, one can readily control the formation of Au petals on Au cores (Figure 3.1i) and corresponding optical signals (Figure 3.1h). It is clear that the number and length of the nanopetals increase as the amount of $HAuCl_4$ increases, and these changes also affect the LSPR peaks from visible to NIR region (Figure 3.1h). CPN-4 showed densely protruding nanopetals from Au core, and these densely positioned metal nanopetals can generate plasmonic coupling-based strong optical signals. In particular, a wide and strong spectrum from CPN-4 particles are desirable for biological applications due to the deep penetration depth of NIR range for biological samples. For the above reasons, we focused on CPN-4 particles for further studies. Figures 1e and 1f represent the dark-field images of pdop-AuNPs and CPN-4 particles, respectively. Strong color change and scattering signal enhancement were observed when the CPNs with plasmonically coupled nanopetals were formed from pdop-AuNPs. The red-to-green color ratio (R/G) was changed from 0.84 for pdop-AuNPs to 1.62 for CPN-4 with ~2 times overall increase in scattering signal intensity. This change in Rayleigh scattering can be attributed to the extensive plasmonic couplings between closely positioned metal nanobranches of CPN-4.[35] The UV-Vis spectra of CPNs cover a broad range from visible to NIR region (530 to 975 nm) due to the multimodal couplings of the nanopetals of CPNs (Figure 3.1h).[43-44]

Next, we tested the potential use of CPNs as photothermal transducers for therapeutic applications (Figure 3.5a). Four different CPNs (CPN-1, CPN-2, CPN-3, and CPN-4; total amount of Au was the same for all these four cases) with increasing density of nanopetals were used for the experiments. First, a quartz cuvette filled with CPN solution (12 μg/mL Au content from ICP-MS) was irradiated with 785-nm laser source (2 W/cm^2) power from 0 to 10 min, and the temperature was measured by a thermocouple in the cuvette. As shown in Figure 3.5b, temperature increased to as high as 53.7 ˚C from 23 ˚C at 6-min laser irradiation with CPN-4 solution (no further noticeable increase in temperature was observed after 6-min irradiation). From the results, we can conclude that the photothermal conversion was highly dependent on the density of the nanopetals of CPNs. It was also shown that laser power is a key parameter in controlling the temperature of the solution with CPNs, and 2 W/cm^2 was found to be the optimal laser power density for effective therapeutic applications (Figure 3.5c). In a control experiment with spherical AuNPs, poor photothermal response was observed under the identical irradiation conditions. For the validation of the repeated use of CPNs for photothermal heating, the photothermal heating-cooling process was repeated. In a typical experiment, the nanoparticle solution was exposed to 785-nm laser for 5 min and allowed to cool down for 30 min to room temperature. This process was repeated three times. The results suggest that the photothermal heating process is completely repeatable with the identical heating-cooling profiles for all of four different CPN cases (Figure 3.5d). In the case of CPN-4, we tested how particle concentration affects the photothermal heating. It was found that 0.5 nM CPN-4 concentration with >4-min irradiation is needed to heat the solution to > 50 ˚C, and, for heating the solution to >55 ˚C, 1 nM AuCP-4 concentration for 5-min heating is required (Figure 3.5e; 785-nm laser,

2 W/cm^2). We then checked the ability of CPNs for organic photosensitizer-free generation of ROS and subsequent PDT applications. It is known that plasmonic nanostructures can photosensitize the activation of $^3O_2$, for eventual conversion to $^1O_2$, and are involved with a plasmonic electron transfer to $^3O_2$.[30,56-58] As proof-of-concept experiments, CPNs or AuNPs (1 nM concentration) were exposed to the laser (785 nm, 2 W/cm^2) for 5 min, and the presence of $^1O_2$ was monitored by an N,N -dimethyl-4-nitrosoaniline(RNO)–histidine colorimetric assay (Figure 3.5f).[59] In this assay, the imidazole moiety of histidine reacts with $^1O_2$, and the resulting transient complex bleaches the RNO molecules – the amount of $^1O_2$ can be directly correlated with decrease in the RNO band intensity in UV-Vis spectrum. The generation of $^1O_2$ was characterized by analysing the characteristic emission at ~1268 nm upon exciting the CPN-4 nanoparticle solution in D_2O with the light wavelength that matches with the LSPR of nanostructure (Figure 3.6).[30,56-57] Purging the solution with nitrogen exhaustively, ceases the phosphorescence emission at 1268 nm, further supporting the presence of $^1O_2$ (Figure 3.6). As shown in Figure 3.5f-g, the amount of produced $^1O_2$ increases with increase in laser exposure time or laser power. The maximum amount of $^1O_2$ was produced with CPN-4 while AuNPs generated the least amount of $^1O_2$, and this shows $^1O_2$ production is highly dependent on the nanopetal shape and density. This laser irradiation-based $^1O_2$ production response pattern is very similar to the pattern of the photothermal results.

We next used CPNs for in vitro cancer therapeutic applications with living cervical cancer cells (HeLa cells). First, we investigated the internalization of nanoparticles by cells. Typically, 1 nM nanoparticle solution was incubated with HeLa cells at 37 °C for 2 h, and excess CPNs were removed by washing the cells with PBS buffer. The dark-field light-scattering images of the treated

cells can directly visualize internalized CPNs, and, as shown in Figure 3.7b, the internalization of CPN-4 particles can be confirmed by the bright reddish orange color inside cells while the dark-field image of the untreated cells shows much weaker nanoparticle-scattering signals (Figure 3.7a). In order to reveal the exact location of CPNs inside the cells, CPN-4-treated cells were fixed, sectioned and subjected to the TEM. The TEM images shows CPN-4 particles were internalized by cells and distributed in the cytosol of a cell (Figure 3.7ci). High-magnification TEM image revealed that CPN-4 particles were mainly located in endosomes, indicative of endocytosis (Figure 3.7cii). The average content of CPN-4 particles, taken up by HeLa cells, was found to be ~1260 particles/cell by the ICP-MS analysis, which is significantly high despite the fact that the size of CPN-4 particles is relatively large (~100 nm in diameter). This could be due to the branching-shape effect that facilitates a facile penetration of cell membrane and the ionic screening effect by various serum proteins (for example, human serum albumin) in cell growth medium and other cell membrane components.[43,60-62] Next, we performed the cytotoxicity test with HeLa cells using Cell Counting Kit (CCK-8, Dojindo lab., Japan). After incubation of the HeLa cells with different amounts of the CPN-4 particles (100 pM to 1 μM) for 24 h, the cell viability results were obtained (Figure 3.7d). The results show that CPN-4 particles have negligible cytotoxic effects on HeLa cells, even at high probe concentrations (>100 nM). We then investigated the use of CPNs for dual PTT-PDT applications with NIR light. With this objective, we measured the photothermal response of CPN-4 as the function of laser irradiation time (785 nm, 2 W/cm^2) in cell growth medium (DMEM, 10 % FBS, 1 % antibiotic) up to 15 min and it took close to 10 min in order to rise medium temperature to 54 °C with negligible further increase in temperature. Choice of temperature <45 °C using benign laser conditions (NIR

laser, ~2 W/cm^2) for clinical PTT-PDT treatment would be crucial to avoid unnecessary heating of normal tissues.[63-64] The experiments were carried out with CPNs and spherical AuNPs. In a typical experiment, HeLa cells were incubated with 0.5 nM nanoparticle solution for 2 h, followed by irradiation with 785-nm laser (2 W/cm^2) for 6 min in order to rise medium temperature to 42±1 °C. (Figure 3.8) A colorimetric live/dead cell vitality assay kit (Invitrogen) was used to determine cell viability after irradiation. In Figure 3f, the green and red colored cells represent live and dead cells, respectively. The cell viability without nanoparticles was nearly 100 % after 6-min laser irradiation, and this demonstrates that 6-min laser irradiation (785-nm laser; 2 W/cm^2) does not damage the cells when there are no plasmonic nanoparticles. The degree of branching on AuNP directly affected cell death when the cells were exposed to 785-nm laser (Figure 3.7e-f). In particular, CPN-4 particles killed nearly all the cancer cells after 6-min laser irradiation with medium temperature rise not more than 42 °C. In the next set of experiments, we quantified total amount of ROS in plasmonic nanoparticle-treated HeLa cells after laser irradiation using the OxiSelect assay (fluorescent signal-based method for measuring total ROS activity in cell lysates). The results show that total amount of ROS is directly correlated with the degree and density of branching on AuNPs (Figure 3.9c). This further suggests that CPN-4 particles can efficiently kill cancer cells with relatively mild increase in temperature (~42 °C) via PTT-PDT dual therapeutics. We then probed the actual fate of important cellular components that have been affected by light-induced PDT-PTT. The damage of cell membrane is a sign of thermoplasmonic therapeutic effect, and this can be directly monitored by fluorescence microscopy using ethidium bromide (EB) to stain the nuclei of dead cells with a damaged cell membrane.[58] In the presence of CPN-4 particles and subsequent laser

irradiation, EB-treated HeLa cells exhibited intense red color. The result indicates that the oxidative damage of lipid cell membrane by CPN-4-mediated PDT-PTT effect. The cell-membrane damage was further confirmed by TEM as shown in the inset image of Figure 3.9b, and change in cell morphology from irregular ellipsoidal to circular shape, indicative of cell death, was also observed from the cells with CPN-4 particles in the dark-field microscope image (Figure 3.9b). Finally, we investigated the ROS-mediated change in nucleic acids using CPN-4 particles as the surface-enhanced Raman scattering (SERS) probes. After treating HeLa cells with CPN-4 particles, the sample was exposed to 785-nm laser for 2, 4, and 6 min, respectively, and genomic DNA was isolated with an extraction procedure as described in literature (Figure 3.9d).[65] The SERS signals were then used to study ROS-mediated primary and secondary structural changes in the isolated DNA (Figure 3.9e).[66] 10 μL of DNA solution (0.1 mg/mL) was mixed with 10 μL of 5 nM CPN-4 solution for the measurement of the SERS spectrum. Isolated DNA is likely to interact with CPN-4 metallic surface through its nucleobases via electrostatic interactions. [43] $^1O_2$ and other intracellular secondary ROS are known to be mutagenic and genotoxic and involved in numerous biological processes. Hydroxyl radicals, excessively generated from lipid oxidation by singlet oxygen, may abstract the hydrogen atoms from the solvent exposed regions of the sugar-phosphate DNA backbone, leading to β-cleavage of the strand and unstacking of DNA bases.[67] The signal of the phosphate-backbone-characteristic Raman band (P^{O2-} symmetric stretch) at 1082 cm^{-1} shifted to 1075 cm^{-1} and its intensity was successively increased in the CPN-4-treated case with 2-6 min exposure to 785-nm laser over CPN-4-free case, and it can be due to phosphate-backbone damage and consequent DNA aggregation. Another ROS-mediated chemical modification involves the oxidation of DNA bases, in particular, the oxidation

of guanine to result in 8-oxoguanosine lesion.[68-69] The Raman peak at 662 cm^{-1} that corresponds to the radial-breathing vibration mode of guanine shifts to lower Raman shift value after the PDT-PTT treatment. Shifted Raman band at ~ 649 cm^{-1} can be attributed to the preferred conformational change of anti-form in guanine to syn-form in 8-oxoguanine and change in electronic environment due to higher hydrogen bond occupancy of 8-oxoguanine as compared to guanine.[65] All these results suggest that there were clear chemical and structural changes in DNA inside the cells when the cells were treated with CPN-4 particles and 785-nm laser.

3.3. Experimental Section

1. Materials and Instruments.

All the materials were used as received without any further purification. Dopamine·HCl was purchased from Sigma-Aldrich (USA). Gold nanoparticles were purchased from BBInternational (USA). Hydrochloric acid and sodium hydroxide were purchased from Daejung Chemicals and Metals (Korea). Tris was purchased from USB Corporation (USA). The formvar/carbon-coated copper grids were purchased from Ted Pella, Inc. (USA). Nanopure water (18.0 MΩ-cm) was used for all experiments. The UV– Vis spectra were obtained from a UV-Vis spectrophotometer (Agilent 8453 spectrophotometer, USA). Elemental analysis and binding energy measurements were performed using the X-ray photoelecton spectroscope (Axis HSi, KRATOS Analytical). The dynamic light scattering measurements were performed using Malvern Zetasizer (Nano ZS). TEM images were obtained using the Energy-Filtering Transmission Electron Microscope (LIBRA 120, Carl Zeiss) with an accelerating voltage of 120 kV. SEM images and EDS-elemental mapping data were obtained using the Field-

Emission Scanning Electron Microscope (SUPRA 55VP, Carl Zeiss). The Raman spectra were acquired using Renishaw inVia Raman Microscope equipped with 514 nm, 633 nm and 785 nm laser sources.

2. Methods.

2.1 Polydopamine (pdop) coating on 80-nm gold nanoparticles.

1 mL of commercially available colloidal solution of 80-nm citrate-stabilized AuNPs (cit-AuNPs) (11 pM) was centrifuged and re-dispersed in Tris·HCl buffer (pH 8.5, 10 mM). 5 μL solution (5 mg/mL) of dopamine·HCl in Tris·HCl buffer (pH 8.5, 10 mM) was then added, and the reaction mixture was vortexed at 25 °C for 4 h. Finally, the reaction mixture was centrifuged at 8000 rpm for 5 min, and the supernatant was removed. The sediment containing pdop-AuNPs was then re-dispersed in DI water. The thickness of the pdop layer on 80-nm Au core was estimated to be ~4.1 nm from the TEM analysis.

2.2 Synthesis of Au core-petal nanostructures.

For the synthesis of CPN-1, 5 mL of 1 nM pdop-AuNP solution, 50 μL of HAuCl4 (5 mM), 100 μL of PVP (1 % w/v, 10,000 MW) and 50 μL of hydroxyl amine (50 mM) were added consecutively and the reaction mixture was rigorously shaken for 5 min at 25 °C. In order to synthesize CPN-2, CPN-3 and CPN-4; 100 uL, 200 uL and 500 uL HAuCl4 (5 mM) and hydroxyl amine (50 mM) respectively, were used.

2.3 Dark-Field Microscopy of Pdop-AuNPs and CPN Nanoprobes.

Properly cleaned glass-slides were treated with 2 % (v/v) aqueous solution of 3-aminopropyl-trimethoxysilane (APTS) for 10 seconds, followed by washing with DI water and drying under nitrogen. Thereafter, 10 μL of a sample (pdop-AuNP or CPN, 0.1 nM) was loaded on the APTS-treated glass slide and

sandwiched with another thinner glass slide to make a sample ready for the dark-field microscopy. The dark-field images were obtained with the Carl Zeiss (DE/Axiovert 200) microscope.

2.3 RNO-Histidine assay.

To a freshly prepared aqueous solution of RNO (50 μM) and 10 mM His (10 mL), 2 mL CPN solution was added and the mixture solution was transferred to a 1 mL quartz cuvette and was subjected to standard laser irradiation (785 nm, 2 W/cm^2). The UV/Vis absorbance at 440 nm was recorded at predetermined irradiation dose.

2.4 $^1O_2$ luminescence detection.

A 1 mL CPN solution in D_2O was subjected to laser irradiation, and the emitted luminescence was recorded. The measurements took place in the dark and at a constant temperature of 15 °C by using thermostat unit coupled to the detector.

2.5 Cell Culture and Treatment with CPN Nanoprobes.

The HeLa cells were suspended in a 96-well plate, to a concentration of 10^4 cells/mL in Dulbecco's modified Eagle's medium (DMEM, 50 μL in each well) with 10 % fetal bovine serum (FBS), and 1 % antibiotic solution (GIBCO, Invitrogen, Karlsruhe, Germany), and cultured at 37 °C and 5 % CO_2, overnight. The culture medium was then replaced with freshly prepared DMEM. Then, different concentrations of CPNs solution in PBS were added and the cells were left in the culture chamber for 2 hours.

2.6 Dark-Field Imaging of Live HeLa Cells.

HeLa cells were cultured onto 35 mm polylysine-modified glass bottom culture dishes (MatTek Corp., USA) and allowed to grow in DMEM medium supplemented with 10% fetal bovine serum and 1% antibiotics (37 °C, 5% CO_2) for overnight. Next, the medium was replaced with fresh culture medium containing CPN nanoprobes (0.1 nM) and cells were further incubated for 2 hours. Thereafter, glass slide was washed with PBS to remove excess CPN nanoprobes and the dark-field images were obtained with the Carl Zeiss (DE/Axiovert 200) microscope.

2.7 Cell Cross-Section Imaging Using the Transmission Electron Microscopy.

For cell cross-section imaging, CPNs incubated cells were first detached from the well plate. After a wash with PBS, at least 5x105 cells were fixed for 2 h with modified Karnovsky's fixative (2 % paraformaldehyde and 2 % glutaraldehyde in 0.05 M sodium cacodylate buffer, pH 7.2). After three washings with 0.05 M sodium cacodylate buffer (pH 7.2) at 4 °C, cells were fixed with 1 % osmium tetroxide in 0.05 M sodium cacodylate buffer (pH 7.2) for 2 h and then washed with distilled water two times. Fixed cells were En bloc stained at 4 °C for overnight using 0.5 % uranyl acetate and then dehydrated with a graded concentration series of ethanol (30 %, 50 %, 70 %, 80 %, 90 %, 100 %, 100 %, and 100 % ethanol; 10 min for each dehydration step). Infiltrated cells using propylene oxide and Spurr's resin were polymerized at 70 °C for 24 h. Various sections of the resin block were cut using the ultramicrotome (MT-X, RMC, Tucson, AZ, USA) and stained 2 % uranyl acetate and Reynolds' lead citrate for 7 min, followed by transferring the section of interest onto a 300 mesh copper TEM grid.

2.8 Toxicity Assay.

The cytotoxicity of various concentrations of CPNs was evaluated using the Cell Counting Kit (CCK-8, Dojindo lab., Japan). Cells were grown in a 96-well plate in 100 μL of DMEM supplemented with FBS. After 24 h seeding, cells were incubated with various concentrations (from 100 pM to 1 μM) of CPN-4 probes for 48 h, and cell viability assay was carried out. The metabolic activity of the cells was measured using CCK-8 (a sensitive colorimetric assay for the determination of the number of viable cells after incubating with probes). Then, 10 uL of the CCK-8 solution was directly added to the incubated cells in each well. After 2 h incubation at 37 °C, the amount of formazan dyes, generated by dehydrogenased of active cells, was measured by a microplate reader (Anthos 2010, Anthos Labtec, Eugendorf, Austria).

2.9 Photothermal Therapy.

After incubation of the HeLa cells with CPNs, the cell monolayers were washed three times with PBS buffer and irradiated with a near-IR laser (785 nm, 2 W cm^{-2}, spot size 5 mm). The cells were then incubated with 200 μL of fresh LIVE/DEAD reagent solution (LIVE/DEAD Viability/Cytotoxicity Kit, Molecular Probes) for 30 min in the dark. The green dots indicate healthy cells while the red dots indicate dead cells.

2.11 Genomic DNA Isolation.

After applying photothermal therapy using CPN-4 nanoprobes for 0, 2, 4, and 6 mins, cells were lysed with 4 mL of lysis buffer containing 0.5 M Tris-HCl (pH 8.0), 20 mM EDTA, 10 mM NaCl, 1 % SDS, and 0.5 mg/mL proteinase K. The mixture was incubated overnight at 55 °C; and thereafter, 2 mL of saturated NaCl (6 M) was added, and the samples were incubated at 55 °C for

10 min. After centrifugation at 5000 rpm for 30 min, the supernatant containing DNA was mixed with 2 times volumes of chilled absolute ethanol, and the DNA was spooled by gently inverting the mix. The tubes were incubated at room temperature for 15 min, and the DNA was recovered by centrifuging at 10000 rpm for 10 min at room temperature. The DNA was washed several times thoroughly with 70 % ethanol and finally air-dried at room temperature.

2.12 SERS measurements of isolated DNA using CPN-4 Nanoprobes.

Isolated DNAs (10 uL, 0.1 mg/mL) from the HeLa cells after PDT-PTT treatment for different durations, were mixed with CPN-4 nanoprobes (10 uL, 5 nM) and SERS spectra were recorded from the mixture loaded on glass slide using Reinshaw InVia Raman spectrometer at 514 nm laser focused with 50x objective.

3.4. Conclusion.

In summary, we have discussed an unprecedented 'oxidative nano-peeling chemistry' of pdop organic corona for plasmonic manipulation of spherical particles. It was well possible to install plasmonic petals of controlled length and density resulting homogeneous flower like nanostructures depending on the amount of gold chloride and reduction kinetics. Suitably designed CPN structures exhibit tunable excellent photothermal and ROS generation properties, which are useful in designing a synergistic bimodal cancer NIR photothermal therapeutic system tested for efficient killing of cervical cancer cells within a short time of 6 min and laser power density 2 W/cm^2 with an ambient temperature rise to ~42 °C. Also, SERS active plasmonic response of CPN nanostructures helped us to probe ROS-mediated structural modifications

at molecular level of genomic DNA isolated from PDT-PTT treated cancer cells. Mechanistic exploration suggested that cause of cell death may be a combination of ROS mediated cell membrane damage and nucleic acid oxidative denaturation. In future, use of such biocompatible plasmonic probes can eventually overcome several drawbacks associated with conventional organic photosensitizer molecules for phototherapy of cancer.

3.5. References.

1. Y. Wang, B. Bing-Yan, L. Chen, Chem. Rev. 2013, 113, 1391-1428.

2. N. J. Halas, S. Lal, W.-S. Chang, S. Link, P. Nordlander, Chem. Rev. 2011, 111, 3913–3961.

3. D. Peer, J. M. Karp, S. Hong, O. C. Farokhzad, R. Margalit, R. Langer, Nature Nanotech. 2007, 2, 751-760.

4. Z. Qin, J. C. Bischof, Chem. Soc. Rev. 2012, 41, 1191–1217.

5. P. K. Jain, X. Huang, I. H. El-Sayed, M. A. El-Sayed, Acc. Chem. Res. 2008, 41, 1578-1586.

6. S. Lal, S. E. Clare, N. J. Halas, Acc. Chem. Res. 2008, 41, 1842-1851.

7. A. P. Castano, P. Mroz, M. R. Hamblin, Nature Rev. 2006, 6, 535–545.

8. J. P. Celli, B. Q. Spring, I. Rizvi, C. L. Evans, K. S. Samkoe, S. Verma, B. W. Pogue, T. Hasan, Chem. Rev. 2010, 110, 2795–2838.

9. E. C. Dreaden, M. A. Mackey, X. Huang, B. Kang, M. A. El-Sayed, Chem. Soc. Rev. 2011, 40, 3391–3404.

10. Y. Hongying, W. Fuyuan, Z. Zhiyi, Dyes Pigments 1999, 43, 109–117.

11. S. Coutier, S. Mitra, L. N. Bezdetnaya, R. M. Parache, I. Georgakoudi, T. H. Foster, F. Guillemin, Photochem. Photobiol. 2001, 73, 297–303.

12. B. J. Tromberg, A. Orenstein, S. Kimel, S. J. Barker, J. Hyatt, J. S. Nelson, M. W. Berns, Photochem. Photobiol. 1990, 52, 375–385.

13. T. M. Sitnik, J. A. Hampton, B. W. Henderson, Br. J. Cancer 1998, 77, 1386–1394.

14. X. Huang, P. K. Jain, I. H. El-Sayed, M. A. El-Sayed, Photochem. Photobiol. 2006, 82, 412–417.

15. H. Takahashi, T. Niidome, A. Nariai, Y. Niidome, S. Yamada, Nanotechnology 2006, 17, 4431–4435.

16. W. Lu, A. K. Singh, S. A. Khan, D. Senapati, H. Yu, P. C. Ray, J. Am. Chem. Soc. 2010, 132, 18103-18114.

17. J. T. Beckham, G. J. Wilmink, S. R. Opalenik, M. A. Mackanos, A. A. Abraham, K. Takahashi, C. H. Contag, T. Takahashi, E. D. Jansen, Lasers Surg. Med. 2010, 42, 912-925.

18. S. Wang, P. Huang, L. Nie, R. Xing, D. Liu, Z. Wang, J. Lin, S. Chen, G. Niu, G. Lu, X. Chen, Adv. Mater. 2013, 25, 3055–3061.

19. B. Jang, J.-Y. Park, C.-H. Tung, I.–H. Kim, Y. Choi, ACS Nano 2011, 5, 1086–1094.

20. L. Gao, J. Fei, J. Zhao, H. Li, Y. Cui, J. Li, ACS Nano 2012, 6, 8030–8040.

21. B. Tian, C. Wang, S. Zhang, L. Feng, Z. Liu, ACS Nano 2011, 5, 7000–7009.

22. M. Guo, H. Mao, Y. Li, A. Zhu, H. He, H. Yang, Y. Wang, X. Tian, C. Ge, Q. Peng, X. Wang, X. Yang, X. Chen, G. Liu, H. Chen, Biomaterials 2014, ASAP http://dx.doi.org/10.1016/j.biomaterials. 2014.02.018.

23. A. Topete, M. Alatorre-Meda, P. Iglesias, E. M. Villar-Alvarez, S. Barbosa, J. A. Costoya, P. Taboada, P. Mosquera, ACS Nano 2014, Article ASAP DOI: 10.1021/nn406425h.

24. Q. Chena, C. Wanga, L. Chenga, W. He, Z. Cheng, Z. Liu, Biomaterials 2014, 35, 2915–2923.

25. L. C. Kennedy, L. R. Bickford, N. A. Lewinski, A. J. Coughlin, Y. Hu, E. S. Day, J. L. West, R. A. Drezek, Small 2011, 7, 169–183.

26. E. Ye, K. Y. Win, H. R. Tan, M. Lin, C. P. Teng, A. Mlayah, M.-Y. Han, J. Am. Chem. Soc. 2011, 133, 8506–8509.

27. Y. Wang, K. C. L. Black, H. Luehmann, W. Li, Y. Zhang, X. Cai, D. Wan, S.-Y. Liu, M. Li, P. Kim, Z.-Y. Li, L. V. Wang, Y. Liu, Y. Xia, ACS Nano 2013, 7, 2068–2077.

28. W. Hasan, C. L. Stender, M. H. Lee, C. L. Nehl, J. Lee, T. W. Odom, Nano Lett. 2009, 9, 1555–1558.

29. Z. Krpetic, P. Nativo, V. Sée, I. A. Prior, M. Brust, M. Volk, Nano Lett. 2010, 10, 4549–4554.

30. G. Pasparakis, Small 2013, 9, 4130–4134.

31. L. Minai, D. Yeheskely-Hayon, D. Yelin, Sci. Rep. 2013, 3, 2146.

32. T. Zhao, X. Shen, L. Li, Z. Guan, N. Gao, P. Yuan, S. Q. Yao, Q.-H. Xu, G. Q. Xu, Nanoscale 2012, 4, 7712-7719.

33. B. Lim, Y. Xia, Angew. Chem. Int. Ed. 2011, 50, 76–85.

34. A. R. Tao, S. Habas, P. Yang, Small 2008, 4, 310-325.

35. F. Hao, C. L. Nehl, J. H. Hafner, P. Nordlander, Nano Lett. 2007, 7, 729-732.

36. J. Fang, S. Du, S. Lebedkin, Z. Li, R. Kruk, M. Kappes, H. Hahn, Nano Lett. 2010, 10, 5006–5013.

37. M. Pradhan, J. Chowdhury, S. Sarkar, A. K. Sinha, T. Pal, J. Phys. Chem. C 2012, 116, 24301– 24313.

38. Q. Li, Y. Jiang, R. Han, X. Zhong, S. Liu, Z.-Y. Li, Y. Sha, D. Xu, Small 2013, 9, 927–932.

39. Y. Yin, P.A Alivisatos, Nature 2005, 437, 664-670.

40. J. Erlebacher, M. J. Aziz, A. Karma, N. Dimitrov, K. Sieradzki, Nature 2001, 410, 450-453.

41. S. Chen, Z. L. Wang, J. Ballato, S. H. Foulger, D. L. Carro, J. Am. Chem. Soc. 2003, 125, 16186-16187.

42. M. Yamamoto, Y. Kashiwagi, T. Sakata, H. Mori, M. Nakamoto, Chem. Mater. 2005, 17, 5391-5393.

43. Z. Wang, J. Zhang, J. M. Ekman, P. J. A. Kenis, Y. Lu, Nano Lett. 2010, 10, 1886–1891.

44. S. Barbosa, A. Agrawal, L. Rodrí guez-Lorenzo, I. Pastoriza-Santos, R. A. Alvarez-Puebla, A. Kornowski, H. Weller, L. M. Liz-Marzan, Langmuir 2010, 26, 14943–14950.

45. H. Lee, S. M. Dellatore, W. M. Miller, P. B. Messersmith, Science 2007, 318, 426-430.

46. M. E. Lynge, R. van der Westen, A. Postmab, B. Stä dler, Nanoscale 2011, 3, 4916–4928.

47. B. P. Lee, P. B. Messersmith, J. N. Israelachvili, J. H. Waite, Annu. Rev. Mater. Res. 2011, 41, 99–132.

48. M. Weinhold, S. Soubatch, R. Temirov, M. Rohlfing, B. Jastorff, F. S. Tautz, C. Doose, J. Phys. Chem. B 2006, 110, 23756–23769.

49. J. Ryu, S. H. Ku, H. Lee, C. B. Park, Adv. Funct. Mater. 2010, 20, 2132–2139.

50. B. Fei, B. Qian, Z. Yang, R. Wang, W. C. Liu, W. C. Mak, J. H. Xin, Carbon 2008, 46, 1792–1828.

51. A. A. Ooka, R. L .Garrell, Biopolymers 2000, 57, 92–102.

52. D. R. Dreyer, D. J. Miller, B. D. Freeman, D. R. Paul, C. Bielawski, Langmuir 2012, 28, 6428– 6435.

53. C. –T. Chen, V. Ball, J. J. de Almeida Gracio, M. K. Singh, V. Toniazzo, D. Ruch, M. J. Buehler, ACS Nano 2013, 7, 1524-1532.

54. S. Hong, Y. S Na, S. Choi, I. T. Song, W. Y. Kim, H. Lee, Adv. Funct. Mater. 2012, 22, 4711–4717.

55. Y. Liu, K. Ai, L. Lu, Chem. Rev. (2014), ASAP DOI: 10.1021/cr400407a.

56. Y.-F. Huang, M. Zhang, L.-B. Zhao, J.-M. Feng, D.-Y. Wu, B. Ren, Z.-Q. Tian, Angew. Chem. Int. Ed. 2014, 53, 2353–2357.

57. R. Vankayala, A. Sagadevan, P. Vijayaraghavan, C.-L. Kuo, K. C. Hwang, Angew. Chem. Int. Ed. 2011, 50, 10640–10644.

58. T. Zhao, X. Shen, L. Li, Z. Guan, N. Gao, P. Yuan, S. Q. Yao, Q.-H. Xu, G. Q. Xu, Nanoscale 2012, 4, 7712–7719.

59. I. Kraljic, S. E. Mohsni, Photochem. Photobiol. 1978, 28, 577-581.

60. T. Cedervall, I. Lynch, M. Foy, T. Berggrd, S. C. Donnelly, G. Cagney, S. Linse, K. A. Dawson, Angew. Chem. Int. Ed. 2007, 46, 5754 –5756.

61. A. M. Alkilany, C. J. Murphy, J. Nanopart. Res. 2010, 12, 2313–2333.

62. N. L. Rosi, D. A. Giljohann, C. S. Thaxton, A. K. R. Lytton-Jean, M. S. Han, C. A. Mirkin, Science 2006, 19, 1027–1030.

63. K. L. O'Neill, D. W. Fairbairn, M. J. Smith, B. S. Poe, Apoptosis 1998, 3, 369–375.

64. J. van der Zee, Ann. Oncol. 2002, 13, 1173-1184.

65. S. R. Panikkanvalappil, M. A. Mackey, M. A. El-Sayed, J. Am. Chem. Soc. 2013, 135, 4815– 4821.

66. S. R. Panikkanvalappil, M. A. Mahmoud, M. A. Mackey, M. A. El-Sayed, ACS Nano, 2013, 7, 7524–7533.

67. B. Balasubramanian, W. K. Pogozelski, T. D. Tullius, Proc. Natl. Acad. Sci. U. S. A. 1998, 95, 9738– 9743.

68. S. Steenken, S. V. Jovanovic, J. Am. Chem. Soc. 1997, 119, 617– 618.

69. J. Cadet, T. Delatour, T. Douki, D. Gasparutto, J.-P. Pouget, J.-L. Ravanat, S. Sauvaigo, Mutat. Res., Genet. Toxicol. Environ. Mutagen. 1999, 424, 9– 21.

Figures.

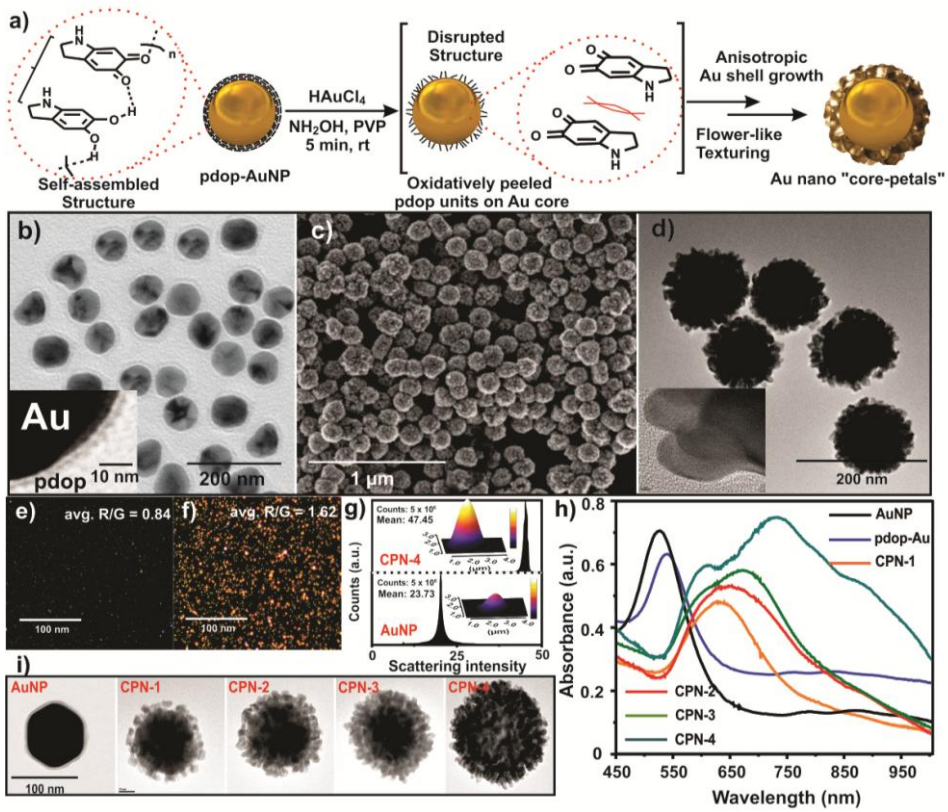

Figure 3.1. (a) Schematic representation for oxidative nanopeeling chemistry of pdop for the synthesis of CPN. (b) TEM image of pdop-AuNPs (80 nm core) with ~5 nm pdop coating. (c) SEM image of CPNs. (d) TEM image of CPNs. (e) Dark-field microscopy image of pdop-AuNPs. (f) Dark-field microscopy image of CPNs. (g) Comparison of scattering intensities and color spectrum obtained from CPNs and pdop-AuNPs. (h) UV/Vis spectra of AuNPs, pdop-AuNPs, CPN-1, CPN-2, CPN-3, CPN-4. (i) TEM images of AuNP, CPN-1, CPN-2, CPN-3, CPN-4 (from left to right).

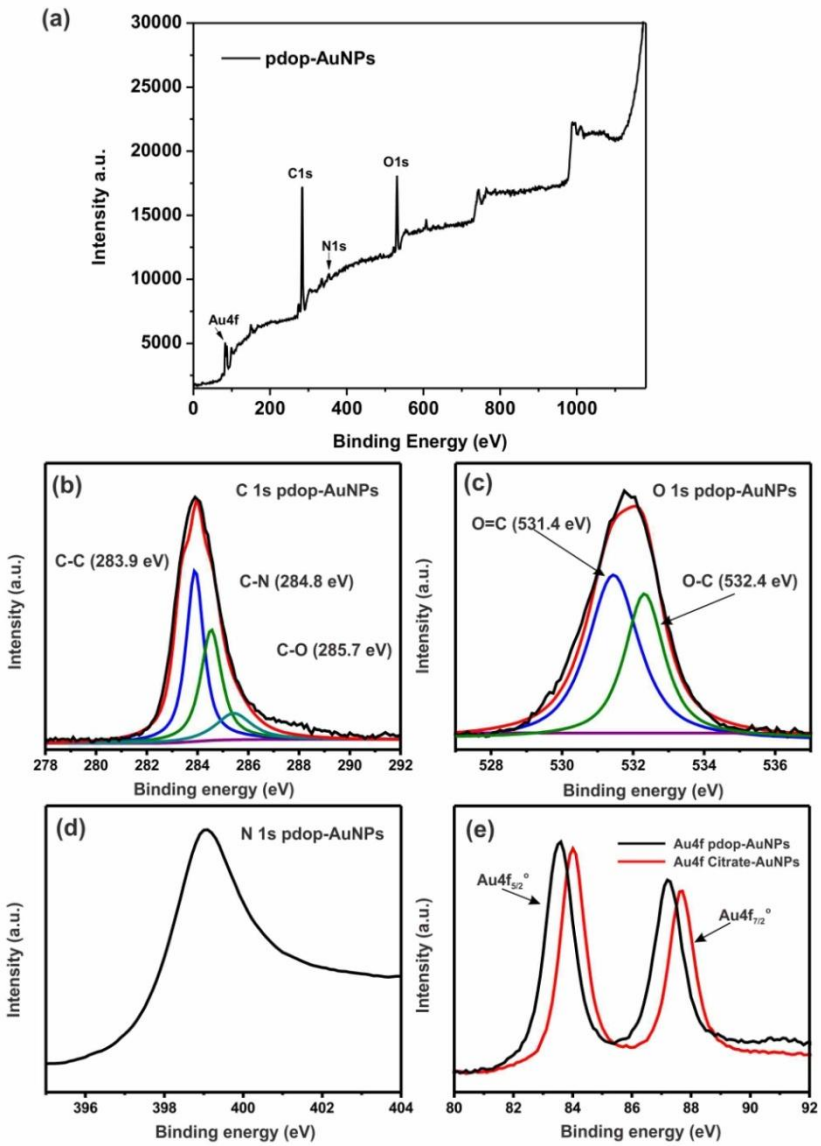

Figure 3.2. The XPS analysis of pdop-AuNPs (80-nm core). (a) The XPS survey spectrum of pdop-AuNPs. (b) The deconvoluted high resolution C 1s peak. (c) The deconvoluted high resolution O 1s peak. (d) High resolution N 1s peak. (e) Comparison between Au 4f peaks in pdop-AuNPs and citrate-AuNPs.

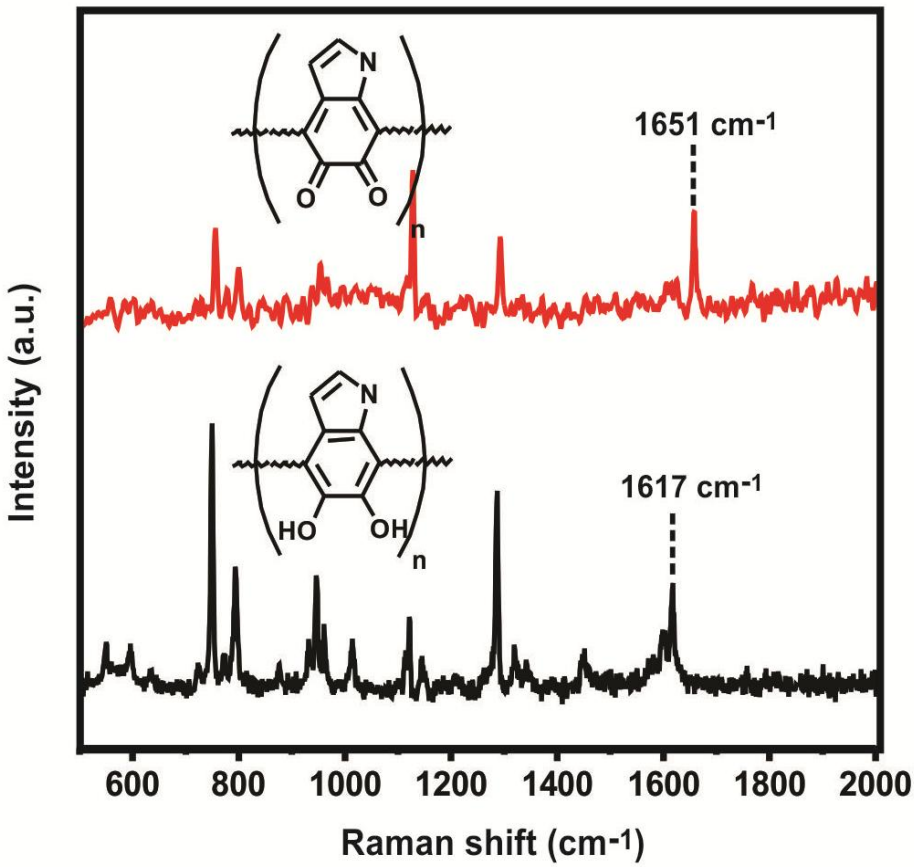

Figure 3.3. Raman spectra (514 nm laser, 10 mW laser power) of pdop-AuNPs before (lower spectrum) and after (upper spectrum) $HAuCl_4$ treatment.

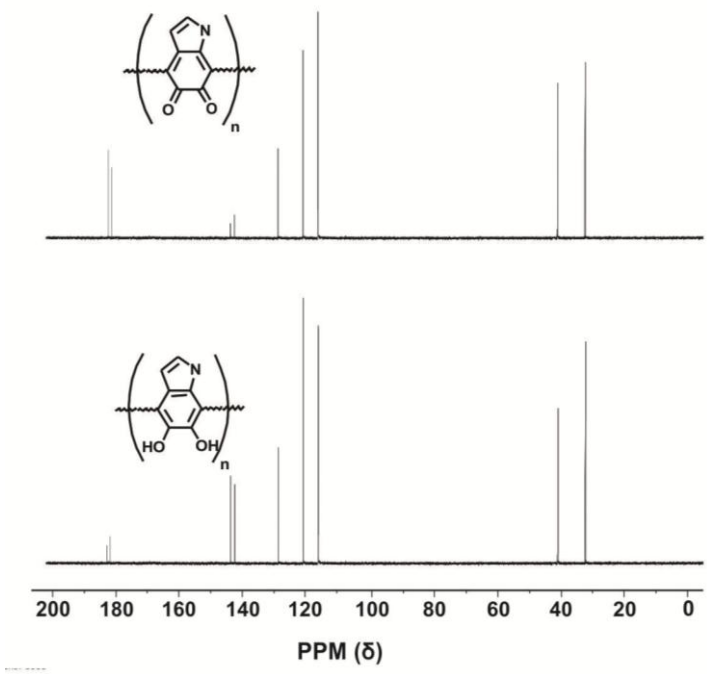

Figure 3.4. ^{13}C NMR (400 MHz in D_2O) of pdop-AuNPs before (lower spectrum) and after (upper spectrum) $HAuCl_4$ treatment.

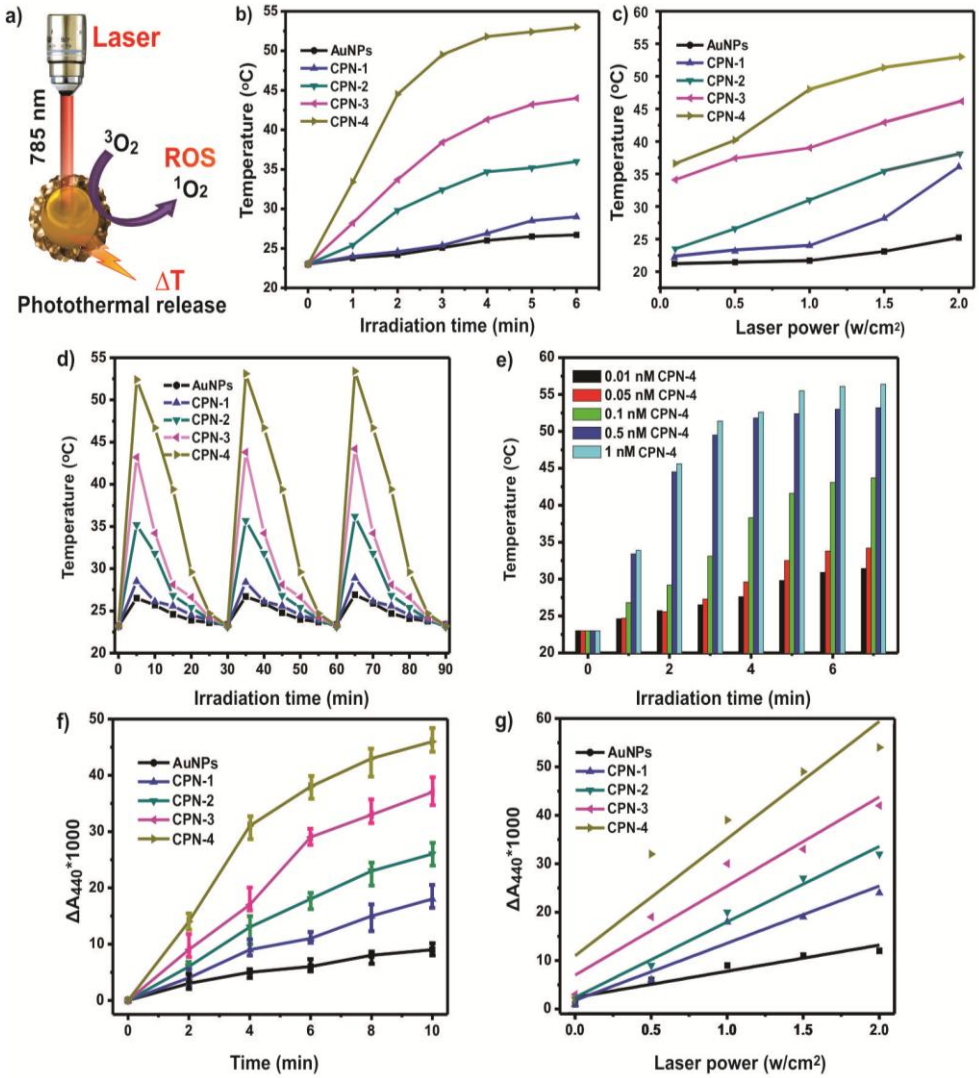

Figure 3.5. (a) Schematic representation of laser-induced photothermal effect and ROS production in CPN. (b) Rise in temperature as the function of laser irradiation time for different gold nanoprobes. (c) Rise in temperature as the function of laser power for different gold nanoprobes. (d) Studies on reproducible photothermal performance of different gold nanoprobes in three successive cycle. (e) Increase in temperature as the function of time for

different concentration of CPN-4. (f) Change in the absorbance of RNO molecules with respect to laser irradiation time as the measurement of laser-induced $^1O_2$ production for different Au nanoprobe aqueous solutions. (g) Change in the absorbance of RNO molecules with respect to laser power as the measurement of effect of laser power on $^1O_2$ production for different Au nanoprobe.

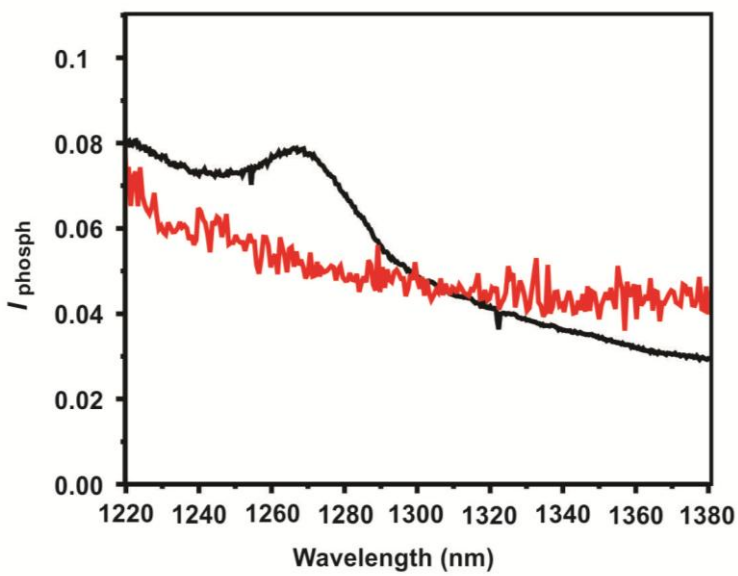

Figure 3.6. Luminescence spectra of CPN-4 solution in D_2O after laser irradiation (in black) and after N_2 gas purging (in red).

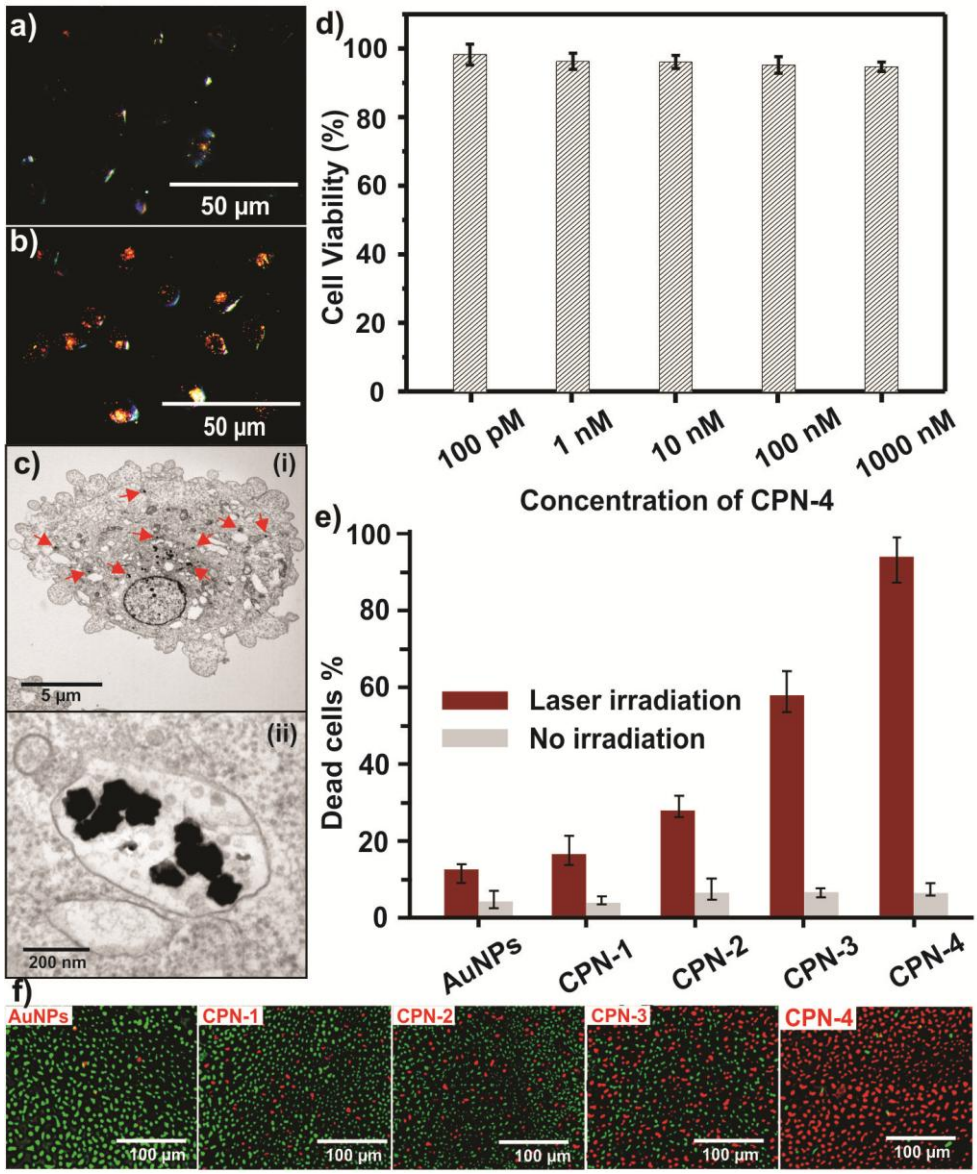

Figure 3.7. (a) Dark-field microscopy image of untreated HeLa cells. (b) Dark-field microscopy image of HeLa cells treated with CPN-4 particles. (c) Low (i) and high (ii) magnification TEM image of a section of fixed HeLa cell treated with CPN-4 probes, showing CPN-4 particles encapsulated in endosome. (d) Results of HeLa cell viability assay after treating with different amounts of

CPN-4 probes under dark conditions. (e) Quantification of cell death upon PDT-PTT treatment of HeLa cells treated with AuNPs, CPN-1, CPN-2, CPN-3, CPN-4, in the presence and absence of laser irradiation. (f) Overlapped fluorescence images obtained from Live/dead cell assay of HeLa cells treated with AuNPs, CPN-1, CPN-2, CPN-3 and CPN-4. The green and red dots indicate healthy cells and dead cells, respectively.

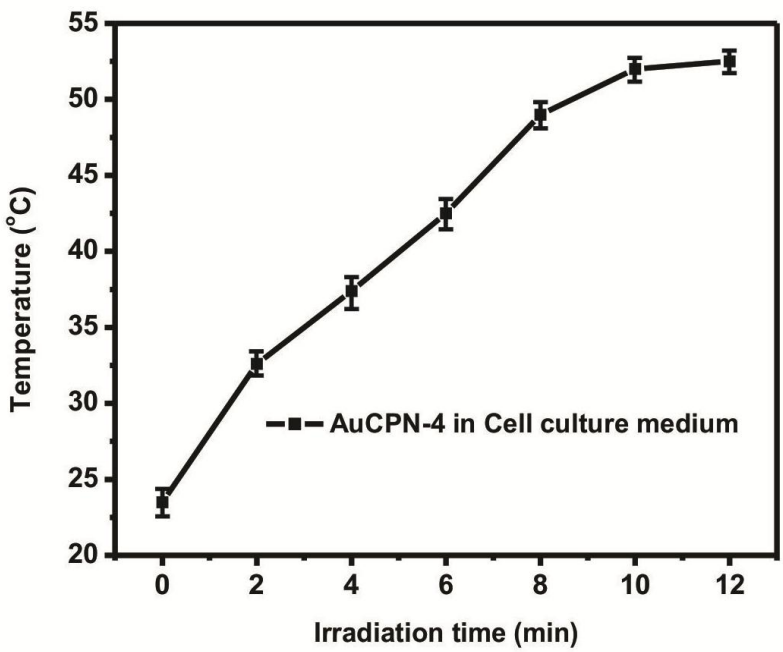

Figure 3.8. Rise in temperature of cell-culture medium as the function of laser irradiation time for CPN-4 nanoprobes.

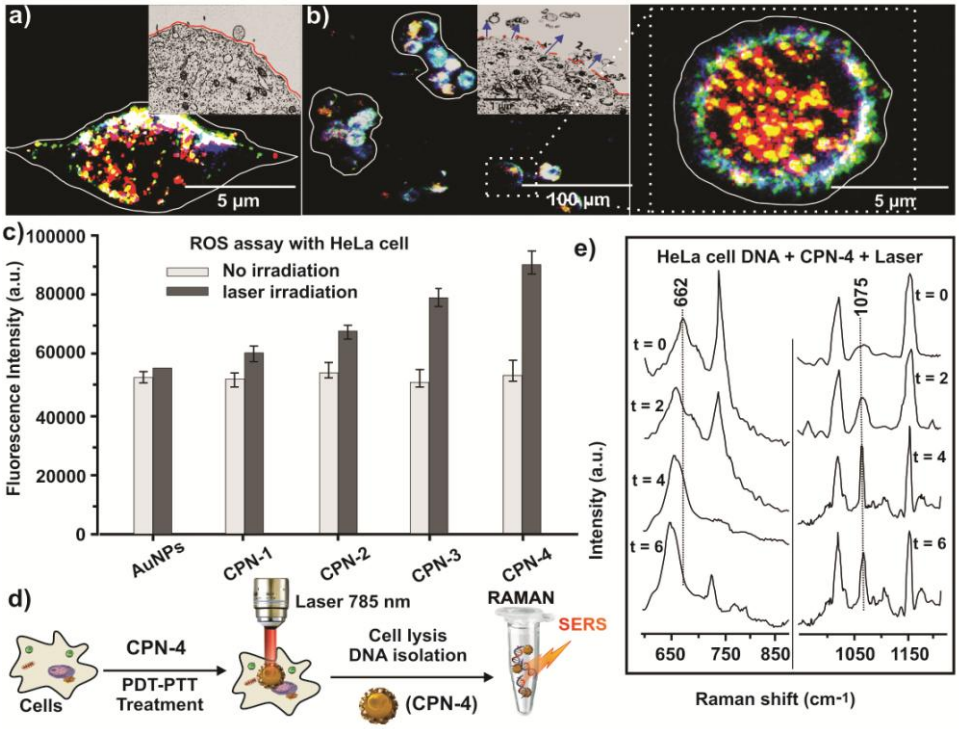

Figure 3.9. Dark-field microscopy image of healthy HeLa cell treated with CPN-4 particles (inset TEM image showing intact cellular membrane). (b) Dark-field microscopy image of dead HeLa cells treated with CPN-4 followed by PDT-PTT treatment (inset TEM image showing damaged cellular membrane). (c) Fluorescence intensities recorded from HeLa cell lysates after PDT-PTT treatment using AuNPs, CPN-1, CPN-2, CPN-3 and CPN-4 for estimation of total ROS using commercial ROS assay kit. (d) Schematic representation for genomic DNA isolation from dead HeLa cells after PDT-PTT treatment. (e) Raman spectra of DNA isolated from PDT-PTT treated HeLa cells after different time of laser irradiation in the case of CPN-4.

Chapter 4

Bioinspired Design of Glutathione-Au@Pt Core-Shell Nanosensor as Hybrid Oxidase/Peroxidase Enzyme-Mimetic Plasmonic Switch for Glucose Sensing

4.1 Introduction.

Apart from being ubiquitous fuel for metabolic pathway, carbohydrates also play pivotal and complex roles in biochemistry of life such as being essential building blocks of biomolecules, mediating cell-cell adhesion/recognition, intracellular regulation and distribution of proteins/enzymes, bacterial/viral infection of cells and many other important functions assimilated in the important field of glycobiology.[1] Recognition and accurate estimation of carbohydrates not only help in clinical diagnosis but also devise the relevant biochemical mechanistic understanding. Abundant presence of polar hydroxyl groups on peripheral positions of sugar molecules render them indistinguishable from water molecules even for the ideal protein receptors. Such notorious supramolecular interaction behaviour of sugars presents a tedious design challenge for the development of enzyme-free biosensors.[2] Nevertheless, recognition of small hydrophobic parts existing as cyclic carbon-framework on the top and bottom of the sugar molecules can be utilized for harnessing selectivity. There has been a persistent motivation for designing biosensors working on an enzyme-mimetic catalytic system matching with or even outperforming various enzymes present in biological environment possessing high substrate specificity and high efficiency in a variety of non-ideal environments.[3] However, considering the inherent delicate nature of enzymes and lack of efficient conjugation methods, it's synthetically challenging to fabricate a complex biomolecular entities performing desired catalytic task particularly in abiological environments. Among conventional glucose sensing methods involving fluorescence measurements,[4] electrochemical detection[5] and Raman spectroscopy;[6] nanomaterial based label-free colorimetric methods are attractive due to their low cost, no interference from electromagnetic fields, compatible to miniaturization, multiplexing, and easy point-of-care readout by

naked eye with high sensitivity.[7] So far, interparticle-distance dependent plasmonic properties of gold nanoparticles (AuNPs) have been useful in the development of sensitive and selective nanosensors for a variety of biomolecules.[8] Recently, nanomaterials of definite size and shape such as metal NPs, metal oxide NPs, carbon nanomaterials and others have been found to behave like redox-based enzymes.[9] Particularly, AuNPs of very small size (~3.5 nm) possess glucose oxidase (GOx) activity under controlled pH conditions; but catalyzing activity of AuNPs diminishes upon increasing the size of AuNPs.[10] Also, AuNPs of different surface charge have been found to possess peroxidase activity.[11] Interestingly, activity of bimetallic nanoparticles of Au with Pt and Pd are enhanced under ambient conditions.[12] Such oxidase/peroxidase-mimetic properties of AuNPs have been found to be extremely sensitive to surface properties, size dependent decrease in activity and gluconic acid surface passivation self-limit the catalytic process.[13] Most of the colorimetric glucose sensing methods are focused on GOx-mediated oxidation of glucose to gluconic acid and hydrogen peroxide as a primary reaction and hydrogen peroxide is detected as a result of secondary reaction catalyzed by other component mostly having peroxidase activity. However, GOx suffers several drawbacks such as decay in activity with time, short working pH range (pH = 6-8), temperature intolerance (activity abruptly ceases at temperature >37 °C), low sensitivity with small dynamic concentration range (1-20 mM), false negative readings and interference with medications.[7i] Other class of glucose sensors, working on the principle of chemical binding with synthetic boronic acid are relatively stable under various environments but they work strictly in a very narrow pH range of 7-8 and suffer from low sensitivity (1-200 mM) and rather poor specificity.[7i] In spite of the potential of metal NPs to behave like different natural enzymes, significant emergence of enzyme-free multifunctional composite probes working in synergistic fashion is

still awaited. Here, we strategically combine three enzyme-mimetic components as synergistic hybrid nanoprobe for efficient recognition and testing of glucose without the involvement of any natural enzyme. We design and synthesize Au@Pt core-shell nanoprobe consisting of plasmonic Au core and very thin and porous Pt shell interfaced with glutathione (GSH) ligand (tripeptide). In the bio-inspired design of our biochemical probe, all three components i.e. Au, Pt and tripeptide GSH contribute in a synergetic fashion in overall performance as a hybrid mimic of oxidase/peroxidase. GSH provides supramolecular coordination assisted fabrication of porous shell in desired thickness; also as a result of oxidation of glucose, coproduced H_2O_2 induces dimerization of interfacial GSH ligands to disulphide (GS-SG) allowing the plasmonic coupling among aggregated Au@Pt NPs, exhibiting a color change detectable by naked eye, or in UV/Vis spectrophotometer. Unlike conventional GOx-hybrid sensors, our enzyme-mimetic probe was functional in a wider pH range (4-9), usable even at high temperatures (up to 80 °C) with excellent dynamic concentration range for glucose detection (1 μm to 100 mM). GSH dimerization reaction during glucose sensing can also be monitored by surface enhanced Raman scattering (SERS)-based signalling in real time owing to the concentration of electromagnetic field by plasmonic probes. During the biosensing process, subnanometer sized interstitial sites in the bimetallic Au@Pt nanostructure may host sugar molecules readily due to the optimum combination of hydrophobicity provided by Au and Pt and presence of hydrogen bonding donor and acceptor atoms in GSH interfacial ligands followed by their catalytic conversion to corresponding acids. Finally, we performed clinical trials of our GSH-Au@Pt enzyme-mimetic nanoprobe for glucose monitoring in the urine samples collected from diabetic patients with excellent accuracy.

4.2 Results and discussion.

First, we synthesized GSH-AuNPs as core plasmonic building block of our nanoprobe using a known synthetic protocol, having average Au core diameter to be ~10 nm (from TEM) and hydrodynamic size to be 13 nm (Figure 4.1).[14] As synthesized GSH-AuNPs exhibited a narrow UV/Vis absorption band at 520 nm and zeta potential to be -56 eV. We chose GSH, a well-known antioxidant tripeptide molecule as capping ligand having thiol group to bind with Au core and amide bonds for sequestering $PtCl_4^{2-}$ anions on AuNP surface through supramolecular anion coordination interaction.[15] In the second step for the synthesis of GSH-Au@Pt, GSH-AuNPs were dispersed in ethylene glycol solvent followed by sequential addition of K_2PtCl_4 (20:1, Au : Pt on atomic basis) and polyvinylpyrrolidone (PVP) and the mixture was heated at 100 °C for 2 hours. As shown in Figure 4.1b, transmission electron microscopy (TEM) image of resulting GSH-Au@Pt clearly showed the formation of very thin and porous Pt shell with regular FCC crystalline pattern having typical lattice spacing of 2.3 Å corresponding to {111} lattice plane (Figure 4.1d), interestingly with noticeable tiny cavities between core and shell. Presence of thin Pt shell was confirmed through X-ray photoelectron spectroscopy (XPS), which is a surface sensitive technique. XPS survey spectrum of GSH-Au@Pt clearly contained characteristic signals corresponding to Au 4f, Pt 4f and S 2p as shown in Figure 4.1j. It is to be noted that nominal thickness of porous Pt coating does not supersede the Au signal from core and S signal from GSH ligands, which are clearly visible in XPS spectra. In the deconvulated high resolution Pt 4f region (Figure 4.1l), two pairs of doublet peaks can be identified and the ratio of the 4f7/2/4f5/2 signals was found to be 4/3, which is typical of reported high quality Pt nanoparticles.[16] The higher intensity doublet at about 71.0 and 74.3 eV is a signature of metallic Pt(0) and the other marginal doublet at

about 74.3 and 77.6 eV can be assigned to Pt(IV) species such as PtO_2 and/or $Pt(OH)_4$, which might be formed in small proportion by the surface oxidation of GSH-Au@Pt after exposure of XPS sample to air during handling. Role of ethylene glycol as mild reducing agent is crucial for guiding slow kinetics of polyol reduction of Pt(II) to Pt(0) and successive formation of porous shell.[17] UV/Vis spectrum of GSH-Au@Pt showed slight plasmon quenching and shifting of localized plasmon resonance (LSPR) band towards higher wavelength by 16 nm due to the presence of Pt. Using higher amounts of K_2PtCl_4 with respect to constant amounts of GSH-AuNPs resulted thicker Pt shells around Au core with porous morphology in all the cases (Figure 4.1f-h). Increase in the thickness of Pt shell resulted gradual plasmon quenching,[18] and the color of the solution became more and more black starting from red color. Role of amide N-H bond present in GSH in directed synthesis of Pt shell is evident from the fact that AuNP core passivated with other ligands such as citrate and L-cysteine which don't have amide functionality did not yield comparable core-shell structures when subjected to the same reaction conditions as GSH-AuNPs (Figure 4.2, Experimental section). Use of PVP was necessary to provide colloidal stability to GSH-Au@Pt during purification procedures involving centrifugation; however, morphology of synthesized Pt shell did not differ in presence or absence of PVP. For further application as colorimetric nanosensor, we chose GSH-Au@Pt prepared from using Au : Pt as 20 : 1, due to the persistence of enough apparent red wine color solution and LSPR band intensity required for plasmonic sensing. We first investigated GOx-mimetic activity of GSH-Au@Pt with known gluconic acid specific colorimetric assay (Figure 4.3).[19] When GSH-Au@Pt were incubated with glucose solution for 30 min followed by addition of Fe(III) and hydroxylamine; solution color turned to red due to the formation of Fe(III)-hydroxamate complex. Red colour of solution persisted even after centrifugation of GSH-Au@Pt particles and the

supernatant showed characteristic absorption peak at 505 nm, confirming gluconic acid was indeed produced from glucose. Absorbance at 505 nm was found to be linearly dependent on glucose concentration with an excellent correlation coefficient (R^2) value to be 0.996. As expected, in the absence of GSH-Au@Pt catalyst, there was no observable color change in the reaction solution. Also, identical diagnosis for gluconic acid production using GSH-AuNPs exhibited substantially slower kinetics of oxidation reaction, indicating the crucial synergistic catalytic role of Pt shell in the case of GSH-Au@Pt (Figure 4.3). Next, peroxidase activity of GSH-Au@Pt was investigated by 3,3′,5,5′-tetramethylbenzidine (TMB)-mediated colorimetric test (Experimental section).[20] Addition of H_2O_2 in deoxygenated aqueous solution of GSH-Au@Pt followed by addition of TMB resulted blue color of oxidized TMB (Ox-TMB) within 15 min and absorption band at 650 nm was observed due to the presence of Ox-TMB. However, same experiment in the absence of GSH-Au@Pt did not result any detectable colour change, which confirms the peroxidase-like catalyzing activity of GSH-Au@Pt probe.

After successfully establishing impressive oxidase and peroxidase dual enzyme-mimetic behaviour of GSH-Au@Pt probe by conventional colorimetric assays, we were interested to carry out direct cascade enzyme-mimetic plasmonic colorimetric detection of glucose (Figure 4.4a). A series of different concentrations of glucose (1 μM, 10 μM, 100 μM, 1 mM, 10 mM, 100 mM) were added to 0.37 nM GSH-Au@Pt in phosphate buffer (10 mM, pH = 7.4). After incubating these mixtures at 25 °C for 60 min, solution colour was monitored and UV/Vis spectra were recorded (Figure 4.4c). The absorption intensity of GSH-Au@Pt at 530 nm gradually decreased as the glucose concentration increased and the solution colour was gradually changed from wine red to blue (Figure 4.4b). As depicted in graphical representation of

Figure 4.4c, it required <20 min to reach ~90% equilibrium for glucose concentrations >1 mM and ~60 min to reach ~90% equilibrium for glucose concentration <1 mM. Conventional glucose sensors usually suffer from relatively short detection range (mM range) which necessitates either concentration or dilution of the sample before analysis, adding further chances of error.[7i] However, wide dynamic range (1 μM to 100 mM) of our plasmonic sensor makes it suitable for broad applications in various fields. In a control experiment carried out in the anaerobic condition, that prevented the H_2O_2 formation, there was no change in LSPR band observed even after 2 hours, confirming the role of metal-catalysed aerobic oxidation in colorimetric signalling. Interstitial cavities present on the interface of Au core and Pt shell in GSH-Au@Pt probe, might play important role as available catalytic sites.[21] Sugar molecule diffuses through porous Pt shell in to catalytic interstitial cavities and may establish hydrogen bonding with GSH molecules. Thereafter glucose is catalytically oxidized to gluconic acid with activated oxygen present on the Au@Pt nanocatalyst surface.[10] In this process, H_2O_2 is produced as the side product which readily reacts with GSH ligands to form GSSGs which are unable to coordinate to AuNPs because of steric hindrance caused by bulky groups around sulfur atoms of GSSGs, this process is also catalyzed by Au@Pt nanocatalyst.[22] H_2O_2-mediated formation of GSSG induces destabilization of core-satellite nanoprobes which eventually induces Au@Pt aggregation and plasmonic coupling between plasmonic Au cores for solution color change and red shift in the UV/Vis spectrum. Oxidative dimerization of GSH ligands was also monitored in real time by SERS as shown in Figure 4.4d. Constant volumes of assay reaction mixtures (100 uL) were subjected to the Raman spectroscopy using 514 nm wavelength laser source. Clearly, Au-S stretching frequency at 189 cm^{-1} was found to be gradually decreased and simultaneously S-S stretching at 504 cm^{-1} frequency was gradually increased with increasing

reaction time. We performed density functional theory (DFT) calculation to observe hydrogen bonding interactions between S-methyl-glutathione (S-methyl-GSH), a simpler analogue of GSH attached with AuNP, and D-glucose. In the minimum energy complex, three hydroxyl groups of D-glucose are involved in strong hydrogen bonding with both carboxylate terminals and middle N-H functionalities of S-methyl-GSH at very close intermolecular distances 1.836, 1.875 and 1.914 A (Figure 4.5b). Also, a strong intramolecular hydrogen bond between the imido and carbonyl groups of S-methlyl-GSH also forms, resulting in a favorable conformation to accommodate well the guest sugar molecule. In fact, ^{1}H NMR studies on interaction of glucose molecule with GSH molecule revealed clear evidence for the involvement of one of the N-H protons of GSH in hydrogen bonding with hydroxyl groups of D-glucose (Figure 4.5c. Both imido N-H protons of GSH come as broad multiplet at 8.5 ppm whereas upon addition of glucose both N-H protons distinctly separate as broad triplet at 8.51 ppm and broad doublet at 8.46 ppm with equal peak area corresponding to one proton each. Also, owing to the involvement of N-H group in hydrogen bonding, coupling constant of doublet (at 3.97 ppm) for adjacent CH_2 proton changes from 0.03 to 0.05. In the ^{1}H NMR spectrum of D-glucose, peaks in the region 3.00 ppm to 4.00 ppm correspond to the pyranose-ring protons directly attached to the carbons having hydroxyl groups and show broad coupling pattern due to the dynamic equilibrium of two anomeric forms (α and β) of D-glucose in the aqueous solution. Interestingly, in the presence of GSH, coupling pattern of ring-protons in the region 3.00 ppm to 4.00 ppm is relatively simplified which may be due to the stabilization of one of the anomers upon strong hydrogen bonding with GSH functional moieties. Carboxylate groups present on the termini of GSH ligand play crucial role in hydrogen bonding with glucose which can be precisely diagnosed by change in vibrational frequencies of carbonyl groups before and after adding

glucose. As shown in Figure 4.5d, Raman spectrum of GSH-Au@Pt contains characteristic vibrational frequency bands for carboxylate and ammonium at 1426 and 1621 cm^{-1}; interestingly, there is clear shift of 8 and 12 cm^{-1} towards higher frequency in the presence of glucose, indicating the influence of hydrogen bonding on the vibrational frequencies of these key functional groups.

Further, we tested tenability of our enzyme-mimetic plasmonic glucose sensing method at different temperatures and pH conditions. Interestingly, there was negligible effect on sensing profile for 100 mM glucose tested by GSH-Au@Pt nanoprobe within a wide pH range (4-9); whereas same trial with natural enzyme GOx (with the help of gluconic acid detection assay)[19] revealed complete deactivation of GOx at pH<4 and pH>7 (Figure 4.6a). In the next experiment, increasing the temperature of assay solution (from 10-90 °C) had lateral augmenting effect on detection reaction kinetics for a range of glucose concentrations (1 μM to 100 mM) whereas in the case of GOx assay, GOx got gradually deactivated beyond ambient temperature (>35 °C) (Figure 4.6b). Such robust behaviour of our GSH-Au@Pt nanoprobe is gratifying as most of the glucose sensing platforms involving natural enzymes are not viable at non-ambient pH and temperature conditions which limits their application scope.

After successful recognition and colorimetric detection of D-glucose, we tested our sensing probe for the detection of other common aldose sugars: ribose, xylose, galactose and mannose. A simple phenomenon of color change from red to blue with increase of sugar concentration was observed for all of the monosaccharides upon reaction. Interestingly, the reaction kinetics was found to be slightly different with highest reactivity for D-glucose (reaction rate ratio – Glucose : ribose : xylose : galactose : mannose = 1 : 0.37 : 0.50 :

0.62 : 0.73). This observed difference in reactivity could be due to different stereochemistries of tested sugars interacting differently with asymmetric environment created by chiral GSH ligand present in interstitial nanocavities of core-shell nanoprobe. Figure 4.5a shows comparison of the chiroptical properties of GSH-Au and GSH-Au@Pt, both produce a strong cirucular dichorism (CD) signature at 225 nm and 221 nm absorption band. In the ultraviolet region (below 300 nm), the glutathione-ligand should only contribute to the CD spectrum. It gives direct insight into the contribution of chiral ligand to the shape and strength of the CD spectra. This possibility is consistent with that the optical activity is decreasing after platinum shell formation; however the asymmetric environment still persists on nanoprobe surface. Interestingly, GSH-Au@Pt nanoprobe did not show any change in LSPR band intensity in the presence of keto-sugar fructose (concentrations <100 mM), probably due to its non-reducing nature and feeble reactivity as compared to aldose sugars. In contrast, well-known boronic acid based glucose sensing methods face substantial interference due to higher sensitivity and selectivity towards fructose as compared to glucose.[4e]

Glucose examination in urine sample provides abundant information about metabolism process and pathological conditions.[23] The normal excretion rate of glucose in urine (urine sugar contains mainly glucose with negligible concentrations of other sugars) ranges between 0.30-1.70 mmol/24 h.[24] An elevated urine glucose concentration signifies impaired tubular reabsorption of glucose, commonly called as condition of hyperglycemia resulting diabetes mellitus.[25] A lower than normal concentration of urine glucose is usually found in patients suffering from bacterial urinary tract infection.[26] High experimental sensitivity and wide dynamic range (1 μM to 100 mM) of our nanosensor makes it suitable for medically examine the condition of hyperglycemia,

hypoglycaemia and urine tract infections. First, we compared the performance of our GSH-Au@Pt nanoprobes with commercial clinical chemistry system (Multistix 10 SG urinalysis strips) for determination of glucose content in artificial urine (prepared by known method mentioned in Experimental section). As shown in Figure 4.7a, the results were in good agreement between both sensing platforms; our GSH-Au@Pt nanoprobe showed an improved correlation coefficient (R^2) of 0.898 as compared with commercial system (R^2 = 0.755) . We further applied our GSH-Au@Pt nanoprobe for quantitative assay of glucose content in urine samples collected from anonymous normal persons (n = 5) and diabetic patients (n = 5). In a typical assay, 10 μL of urine sample was added to 100 μL solution of GSH-Au@Pt nanoprobe (0.37 nM) and mixture was incubated at 25 °C for equilibration (~1 hour) and change in LSPR band intensity at 530 nm was recorded. As shown in Figure 4.7b, the concentration of glucose in urine samples was derived from calibration plot obtained by correlating change in absorbance at 530 nm with standard glucose concentrations present in artificial urine (Figure 4.8, for details see in Experimental section). In the case of normal persons glucose concentrations were found to be < 5 mM, whereas samples obtained from diabetic patients contained glucose in relatively higher concentrations (15-35 mM). As shown in Figure 4.7, results obtained from our nanoprobe is in good agreement with commercial system with no false negative or positive. Usually, there is a high probability for patients affected by diabetes also suffering from renal disease such as proteinuria (urokinase protein higher than 300 mg/L in urine)[27] and cystinuria (cysteine or cystine residues higher than 200 μM concentrations).[28] For investigating interference of proteins in glucose sensing, we added albumin protein in 500 mg/L concentration in urine sample as a model for proteinuria. Also, in a different urine sample we added cysteine in 300 μM concentration

as the mimic of cystinuria condition. Notably, addition of albumin protein or cysteine did not influence UV/Vis spectra or color change pattern during the glucose sensing using GSH-Au@Pt. Ascorbic acid (vitamin C) is another possible interfering ingredient present in urine especially in the case of redox-sensing methods. We added an excess amount of ascorbic acid (3 mM) in urine sample in order to probe possible redox interference; interestingly, it turned out to be no influence of the presence of ascorbic acid on UV/Vis spectral profile (Figure 4.9). Such unexpected feature of our GSH-Au@Pt probe could be due to relatively, inefficient hydrogen bonding of ascorbic acid with GSH interfacial ligands as well as distinguishable catalytic response of Au@Pt towards slightly different oxidation potentials of glucose (-0.050 V) and ascorbic acid (-0.081 V).

4.3 Experiment Section.

Materials and Instruments.

All the materials were used as received without any further purification. Reduced L-glutathione, gold chloride, potassium tetrachloroplatinate, ethylene glycol, polyvinylpyrrolidone and all used sugars were purchased from Sigma-Aldrich (USA). Hydrochloric acid and sodium hydroxide were purchased from Daejung Chemicals and Metals (Korea). The formvar/carbon-coated copper grids were purchased from Ted Pella, Inc. (USA). Nanopure water (18.0 MΩ-cm) was used for all experiments. The UV-Vis spectra were obtained from a UV-Vis spectrophotometer (Agilent 8453 spectrophotometer, USA). Elemental analysis and binding energy measurements were performed using the X-ray photoelecton spectroscope (Axis HSi, KRATOS Analytical). The dynamic light

scattering measurements were performed using Malvern Zetasizer (Nano ZS). TEM images were obtained using the Energy-Filtering Transmission Electron Microscope (LIBRA 120, Carl Zeiss) with an accelerating voltage of 120 kV. The Raman spectra were acquired using Renishaw inVia Raman Microscope equipped with 514 nm, 633 nm and 785 nm laser sources.

Methods.

Synthesis of glutathione capped gold nanoparticles.

The preparation of GSH-AuNPs was done according to the earlier described procedure with slight modification. An aqueous solution of tetrachloroauric acid ($HAuCl_4 \cdot 3H_2O$, 1 mL, 0.025 M) was added to GSH (7.8 mL, 0.019 M) dissolved in 0.1 M sodium phosphate buffer at pH 7.4 (adjusted by 1 M NaOH). Then a freshly prepared $NaBH_4$ solution (2 mg/mL in water, 10-fold molar excess) was added with vigorous stirring. The mixture was allowed to stir for overnight at rt. Excess ligands were removed from the solution by centrifugation at 14,000 rpm for 15 min.

Synthesis of GSH-Au@Pt nanprobes.

A solution of GSH-AuNPs (1 mL) prepared in previous section, was mixed with ethylene glycol solvent (1 mL) followed by sequential addition of K_2PtCl_4 (20:1, Au : Pt on atomic basis) and 100 uL polyvinylpyrrolidone solution (MW 10000, 1% w/v) and the mixture was heated at 100 °C for 2 hours. After completion of reaction, GSH-Au@Pt probes were purified through centrifugation (10,000 rpm, 10 min) and washing with DI water.

Typical assay procedure for glucose sensing using GSH-Au@Pt.

10 μL of different concentrations of glucose (1 μM, 10 μM, 100 μM, 1 mM, 10 mM, 100 mM) were added to 100 μL of GSH-Au@Pt (0.37 nM) in phosphate buffer (10 mM, pH=7.4). After incubating these mixtures at 25 °C for 60 min, solution colour was monitored and UV/Vis spectra were recorded.

Procedure for gluconic acid specific assay for diagnosing oxidase enzyme activity of GSH-Au@Pt.

After incubating 100 uL of GSH-Au@Pt (0.37 nM) with 10 uL of glucose solution (0.2 mM to 1 mM) for 30 min, mixture was centrifuged at 10,000 rpm and supernatant was taken out for next step. In the next step, 50 μL of solution A (5 $mmolL^{-1}$ EDTA and 0.15 $mmolL^{-1}$ triethylamine in water) and 6 μL of solution B (3 $mmolL^{-1}$ NH_2OH in water) were added to 100 μL of supernatant solution. After 25 min of incubation, 31 μL of solution C (1 $mmolL^{-1}$ HCl, 0.1 $mmolL^{-1}$ $FeCl_3$, and 0.25 $mmolL^{-1}$ CCl_3COOH in water) was added to the above aqueous solution, and the reaction was allowed to proceed for 5 min before spectral measurements at 505 nm.

Procedure for diagnosing peroxidase enzyme activity of GSH-Au@Pt.[29]

100 uL of GSH-Au@Pt (0.37 nM) was mixed with 100 uL of 3,3,5,5-tetramethylbenzidine (1 mM) and 10 uL of H_2O_2 (1 mM) was added to the mixture and UV/Vis spectra were recorded at 651 nm at different time intervals.

Glucose testing in urine samples.

10 μL of urine sample was directly added to 100 μL of GSH-Au@Pt (0.37 nM) in phosphate buffer (10 mM, pH = 7.4). After incubating these mixtures at 25

°C for 60 min, UV/Vis spectra were recorded. Concentration of glucose in urine sample was determined using calibration plot obtained from artificial urine containing known amounts of glucose.

Preparaton of artificial urine.[30]

Two stock solutions (500 mL) of artificial urine were prepared in the absence and presence of glucose (10.0 mM), respectively. The solutions were filtered using 0.22 μm filter. The pH of the solutions was adjusted to 7.4 using a KOH solution (1 M). The glucose containing solution was serially diluted with the glucose-free solution to obtain standard concentrations of 0.1-10.0 mmol/L of glucose with a constant ionic strength (~210 mmol/L).

4.4 Conclusion.

In conclusion, we have designed and synthesized a multi-enzyme-mimetic integrated core@shell nanoprobe sensing system consisting of gold core and Pt shell with interfacial peptide ligands. Strategically engineered porous thin Pt shell allows cognizable diffusion of glucose molecule in to interstitial sites followed by supramolecular intraction with GSH ligands and metallic surfaces. Tandem synergistic combination of oxidase and peroxidase activities of GSH-Au@Pt allows efficient conversion of glucose to gluconic acid and GSH is dimerized in the process and plasmonic Au core exhibit aggregation induced color change as the naked-eye signal for enzyme-mimetic reaction. Mechanism of sugar recognition by GSH-Au@Pt nanoprobe is also supported by DFT calculations, ^{1}H NMR and Raman spectroscopy. We performed clinical test with urine samples collected from normal persons and diabetic patients with very high degree of accuracy (compared with commercial clinical testing platform).

High experimental sensitivity and wide dynamic range (1 μM to 100 mM) of our nanosensor makes it potentially useful for medically examine the condition of hyperglycemia, hypoglycaemia and urine tract infections. Present work opens an avenue for the development of versatile hybrid nanostructures intelligently utilizing the catalytic activity of different combinations of nanometals and recognition capability of functional organic corona for useful biosensing applications.

4.5 References.

1. a) A. P. Davis, R. S. Wareham, Angew. Chem. Int. Ed. 1999, 38, 2978 -2996; b) Y. C. Lee, R. T. Lee, Acc. Chem. Res. 1995, 28, 321-327; c) R. A. Dwek, Chem. Rev. 1996, 96, 683-720; d) G. A. Rabinovich, M. A. Toscano, Nature Rev. 2009, 9, 338-352; e) J. Arnaud, A. Audfray, A. Imberty, Chem. Soc. Rev. 2013, 42, 4798-4813.

2. a) S. Striegler, Curr. Org. Chem. 2003, 7, 81–102; b) Y. Ferrand, M. P. Crump, A. P. Davis, Science 2007, 318, 619–622; c) C. Ke, H. Destecroix, M. P. Crump, A. P. Davis, Nature Chem. 2012, 4, 718-723.

3. a) R. Breslow, S. D. Dong, Chem. Rev. 1998, 98, 1997–2012; b) R. Breslow, Acc. Chem. Res. 1995, 28, 146–153. c) G. Wulff, Chem. Rev. 2002, 102, 1-28; d) L.C. Fruk, M. Niemeyer, Angew. Chem. Int. Ed. 2005, 44, 2603–2606; e) Y. Murakami, J.-I. Kikuchi, Y. Hisaeda, O. Hayashida, Chem. Rev.

1996, 96, 721–758; f) G. Mugesh, H. B. Singh Chem. Soc. Rev. 2000, 29, 347–357; g) T. Darbre, J.-L. Reymond, Acc. Chem. Res. 2006, 39, 925–934.

4. a) Y. Liu, C. Deng, L. Tang, A. Qin, R. Hu, J. Sun, B. Tang, J. Am. Chem. Soc. 2011, 133, 660–663; b) C. Zhang, Y. Yuan, S. Zhang, Y. Wang, Z. Liu, Angew. Chem. Int. Ed. 2011, 50, 6851–6854; c) H. Y. Lee, J. J. Lee, J. Park, S. B. Park, Chem. Eur. J. 2011, 17, 143–150; d) B. Tang, L. Cao, K. Xu, L. Zhuo, J. Ge, Q. Li, L. Yu, Chem. Eur. J. 2008, 14, 3637–3644; e) Y.-J. Huang, W.-J. Ouyang, X. Wu, Z. Li, J. S. Fossey, T. D. James, Y.-Bao Jiang, J. Am. Chem. Soc. 2013, 135, 1700–1703.

5. a) Y. Xiao, F. Patolsky, E. Katz, J. F. Hainfeld, I. Willner, Science 2003, 299, 1877–1881; b) K. Besteman, J. O. Lee, F. G. M. Wiertz, H. A. Heering, C. Dekker, Nano. Lett. 2003, 3, 727–730; c) S. Bao, C. Li, J. Zang, X. Cui, Y. Qiao, J. Guo, Adv. Funct. Mater. 2008, 18, 591–599; d) J. Qiu, L. Shi, R. Liang, G. Wang, X. Xia, Chem. Eur. J. 2012, 18, 7950–7959; e) D. Zhai, B. Liu, Y. Shi, L. Pan, Y. Wang, W. Li, R. Zhang, G. Yu, ACS Nano 2013, 7, 3540–3546; f) C. Guo, H. Huo, X. Han, C. Xu, H. Li, Anal. Chem. 2014, 86, 876–883

6. a) K. E. Shafer-Peltier, C. L. Haynes, M. R. Glucksberg, R. P. Van Duyne, J. Am. Chem. Soc. 2003, 125, 588–593; b) K. V. Kong, Z. Lam, W. K. O. Lau, W. K. Leong, M. Olivo, J. Am. Chem. Soc. 2013, 135, 18028–18031.

7. a) H. Wei, E. Wang, Anal. Chem. 2008, 80, 2250–2854; b) M. I. Kim, J. Shim, T. Li, J. Lee, H. G. Park, Chem. Eur. J. 2011, 17, 10700–10707; c) Y.

Song, K. Qu, C. Zhao, J. Ren, X. Qu, Adv. Mater. 2010, 22, 2206–2210; d) Y. Jiang, H. Zhao, Y. Lin, N. Zhu, Y. Ma, L. Mao, Angew. Chem. Int. Ed. 2010, 49, 4800–4804; e) C. Xu, J. Ren, L. Feng, X. Qu, Chem. Commun. 2012, 48, 3739–3741; f) B. Shlyahovsky, D. Li, E. Katz, I. Willner, Biosens. Bioelectron. 2007, 22, 2570–2576; g) W. Li, L. Feng, J. Ren, L. Wu, X. Qu Chem. Eur. J. 2012, 18, 12637–12642. h) H. He, X. Xu, H. Wu, Y. Jin, Adv. Mater. 2012, 24, 1736–1740; i) M.-S. Steiner, A. Duerkop, O. S. Wolfbeis, Chem. Soc. Rev. 2011,40, 4805–4839.

8. a) M. C. Daniel, D. Astruc, Chem. Rev. 2004, 104, 293-346; b) P. P. Edwards, J. M. Thomas, Angew. Chem., Int. Ed. 2007,46, 5480–5486; c) D. A. Giljohann, C. A. Mirkin, Nature 2009, 462, 461–464. d) N. L. Rosi, C. A. Mirkin, Chem. Rev. 2005, 105, 1547–1562; e) W. Zhao, M. A. Brook, Y. F. Li, ChemBioChem 2008, 9, 2363– 2371; f) S. Song, Y. Qin, Y. He, Q. Huang, C. Fan, H. Chen, Chem. Soc. Rev. 2010, 39, 4234–4243.

9. a) H. Wei, E. Wang, Chem. Soc. Rev. 2013, 42, 6060-6093; b) Y. Lin, J. Ren, X. Qu, Acc. Chem. Res. 2014 ASAP (DOI: 10.1021/ar400250z); c) Y. Lin, J. Ren, X. Qu, Adv. Mater. 2014 ASAP (DOI: 10.1002/adma.201400238).

10. a) M. Comotti, C. D. Pina, R. Matarrese, M. Rossi, Angew. Chem., Int. Ed. 2004, 43, 5812– 5815; b) P. Beltrame, M. Comotti, C. D. Pina, M. Rossi, Appl. Catal. 2006, 297, 1–7.

11. a) S. Wang, W. Chen, A. L. Liu, L. Hong, H. H. Deng and X. H. Lin, ChemPhysChem 2012, 13, 1199–1204. b) Y. Jv, B. X. Li and R. Cao, Chem.

Commun. 2010, 46, 8017–8019; c) Y. J. Long, Y. F. Li, Y. Liu, J. J. Zheng, J. Tang and C. Z. Huang, Chem. Commun. 2011, 47, 11939–11941.

12. a) W. W. He, Y. Liu, J. S. Yuan, J. J. Yin, X. C. Wu, X. N. Hu, K. Zhang, J. B. Liu, C. Y. Chen, Y. L. Ji and Y. T. Guo, Biomaterials 2011, 32, 1139–1147; b) J. B. Liu, X. N. Hu, S. Hou, T. Wen, W. Q. Liu, X. Zhu and X. C. Wu, Chem. Commun. 2011, 47, 10981–10983; c) K. Zhang, X. N. Hu, J. B. Liu, J. J. Yin, S. A. Hou, T. Wen, W. W. He, Y. L. Ji, Y. T. Guo, Q. Wang and X. C. Wu, Langmuir 2011, 27, 2796–2803; d) Y. Li, Q. Lu, S. Wu, L. Wang, X. Shi, Biosens. Bioelectron. 2013, 41, 576–581.

13. W. Luo, C. Zhu, S. Su, D. Li, Y. He, Q. Huang, C. Fan, ACS Nano 2010, 4, 7451–7458.

14. R. P. Briñas, M. Hu, L. Qian, E. S. Lymar, J. F. Hainfeld, J. Am. Chem. Soc. 2008, 130, 975–982.

15. C. J. Serpell, J. Cookson, D. Ozkaya, P. D Beer, Nature Chem. 2011, 3, 478-483.

16. F. Sen, G. Gökağac, J. Phys. Chem. C 2007, 111, 1467-1473.

17. a) T. Herricks , J. Chen, Y. Xia, Nano Lett. 2004, 4, 2367–2371; b) M. Lin, H. Huang, Y. Liu, C. Liang, S. Fei, X. Chen, C. Ni, Nanotechnology 2013, 24, 065501.

18. G.-R. Zhang, B.-Q. Xu, Nanoscale 2010, 2, 2798–2804.

19. E. T. Rakitzis, P. Papandreou, Chem. Biol. Interact. 1998, 113, 205–216.

20. Z. Gao, L. Hou, M. Xu, D. Tang, Sci. Rep. 2014, 4, 3966.

21. a) M. Subhramannia, V. K. Pillai, J. Mater. Chem. 2008, 18, 5858–5870; b) L. Y. Chen, T. Fujita, Y. Ding, M. W. Chen, Adv. Funct. Mater. 2010, 20, 2279-2285. c) M. Yan, T. Jin, Y. Ishikawa, T. Minato, T. Fujita, L.-Y. Chen, M. Bao, N. Asao, M.-W. Chen, Y. Yamamoto, J. Am. Chem. Soc. 2012, 134, 17536–17542.

22. S. Kumar, W.-K. Rhim, D.-K. Lim, J.-M. Nam, ACS Nano 2013, 7, 2221–2230.

23. J. A. Simerville, W. C. Maxted, J. Pahira, J. Am. Fam. Physician 2005, 71, 1153– 1162.

24. A. Kratz, M. Ferraro, P. M. Sluss, K. B. Lewandrowski, N. Engl. J. Med. 2004, 351, 1548– 1563.

25. E. Ferrannini, Diabetes 2011, 60, 695– 696.

26. B. Scherstén, A. Dahlqvist, H. Fritz, L. Köhler, L. Westlund, L. J. Am. Med. Assoc. 1968, 204, 205–208.

27. J. M. Ginsberg, B. S. Chang, R. A. Matarese, S. Garella, N. Engl. J. Med. 1983, 309, 1543-1546.

28. S. O. Thier, S. Segal, M. Fox, A. Blair, L. E. Rosenberg, J. Clin. Invest. 1965, 44, 442-448.

29. Z. Gao, L. Hou, M. Xu, D. Tang, Sci. Rep. 2014, 4, 3966.

30. A. K. Yetisen, Y. Montelongo, F. da Cruz Vasconcellos, J. L. Martinez-Hurtado, S. Neupane, H. Butt, M. M. Qasim, J. Blyth, K. Burling, J. B. Carmody, M. Evans, T. D. Wilkinson, L. T. Kubota, M. J. Monteiro, C. R. Lowe, Nano Lett. 2014, Article ASAP (DOI: 10.1021/nl5012504).

Figures.

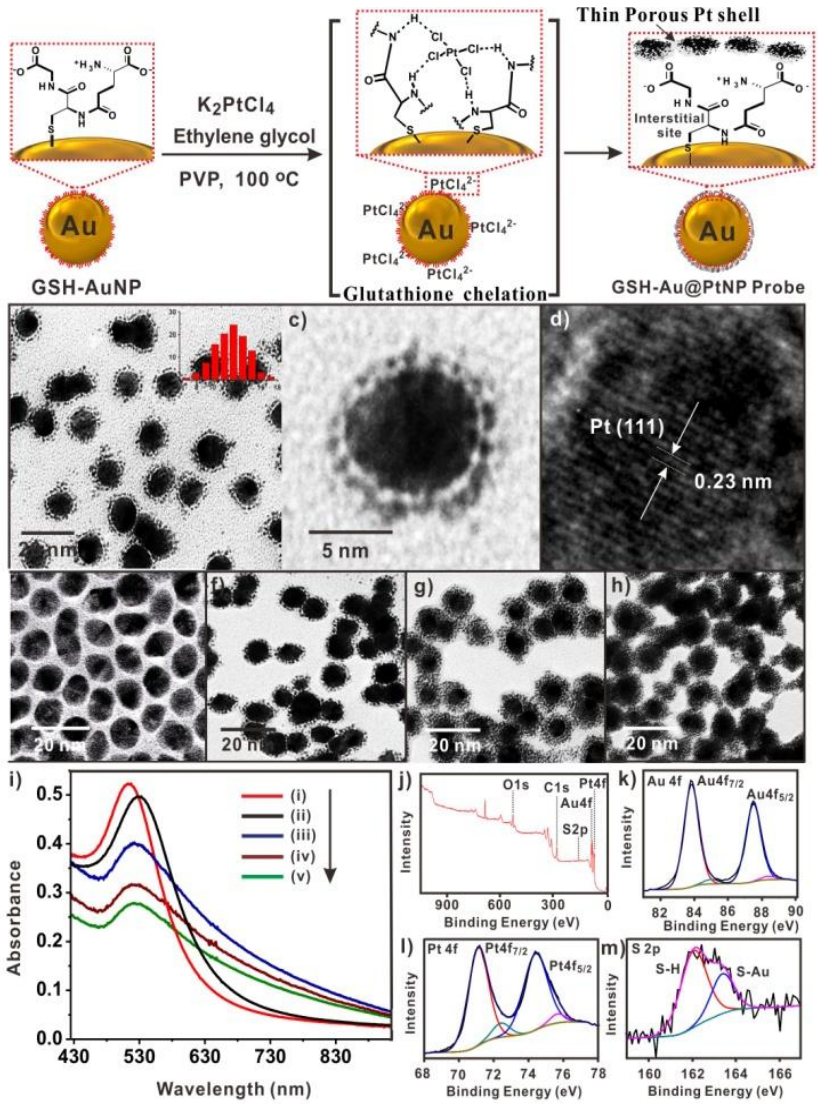

Figure 4.1. Schematic representation for synthesis of GSH-Au@Pt (a). TEM image of GSH-Au@Pt in low magnification (b). TEM image of GSH-Au@Pt in high magnification (c). HRTEM image of Pt shell in GSH-Au@Pt (d). TEM images of GSH-AuNPs and GSH-Au@Pt synthesized using increasing amounts of K_2PtCl_4 (e-h). UV/Vis spectra of (i) GSH-AuNPs and (ii-v) GSH-Au@Pt

corresponding to increasing thickness of Pt shell (i). XPS survey spectrum of GSH-Au@Pt (j). Au 4f, Pt 4f and S 2p high resolution XPS peaks for GSH-Au@Pt (j-m).

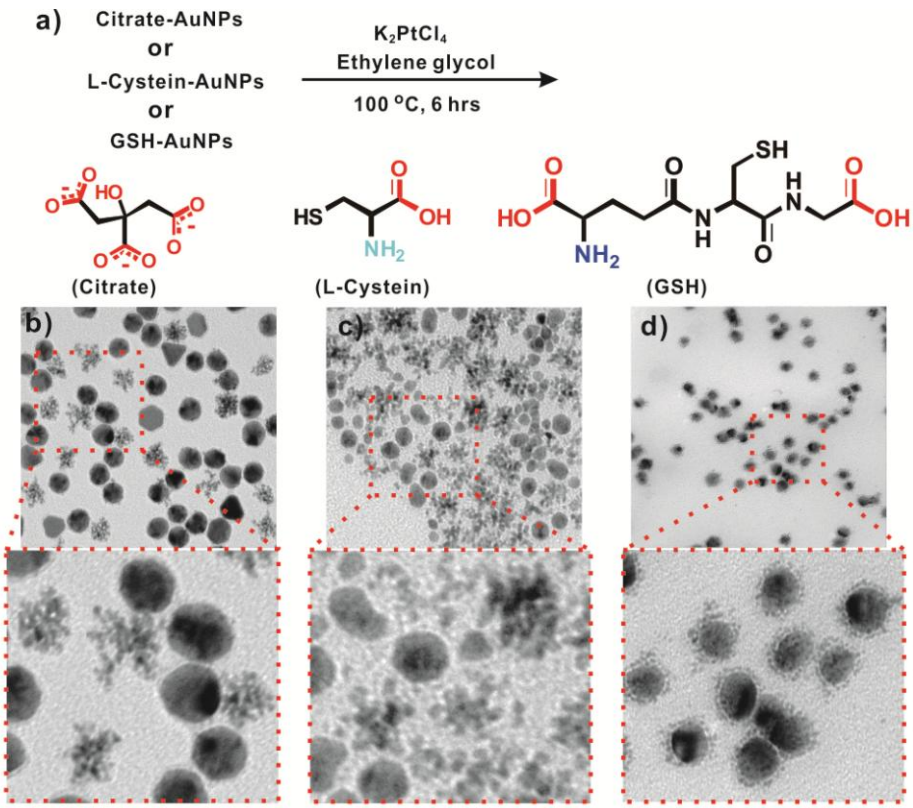

.

Figure 4.2. a) Thiolated ligands used in the control experiment for the synthesis of Au@Pt core-shell strucures and b) corresponding TEM images.

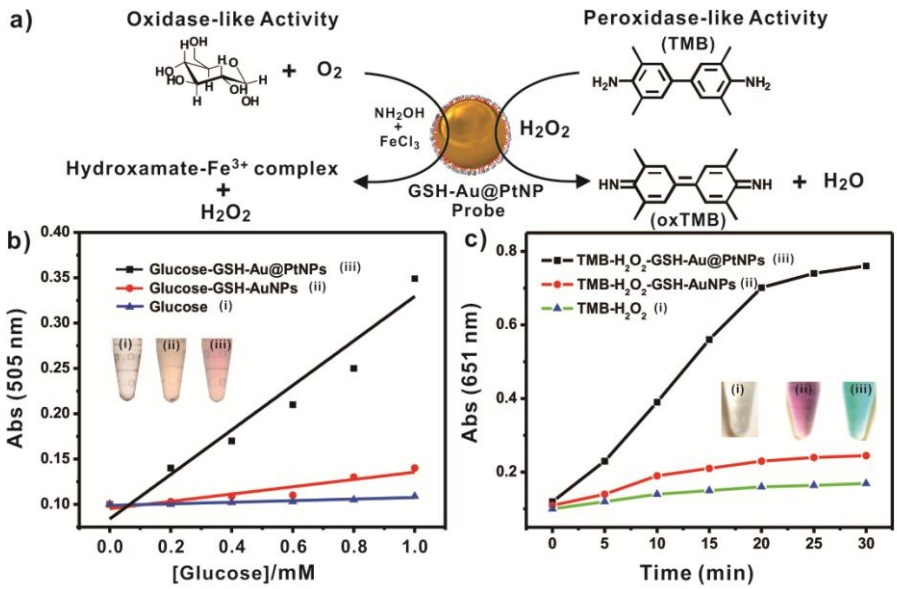

Figure 4.3. Combined schematic representation for test of GSH-Au@Pt to show oxidase/peroxidase like activity (a). Plot of absorbance at 505 nm due to the formation of Fe(III)-hydroxamate complex vs glucose concentration used for the reaction without any catalyst (i), in the presence of GSH-AuNPs (ii) and GSH-Au@Pt (iii) (b). Plot of absorbance at 651 nm due to the formation of oxidized TMB by H_2O_2 vs reaction time for the reaction without any catalyst (i), in the presence of GSH-AuNPs (ii) and GSH-Au@Pt (iii) (c).

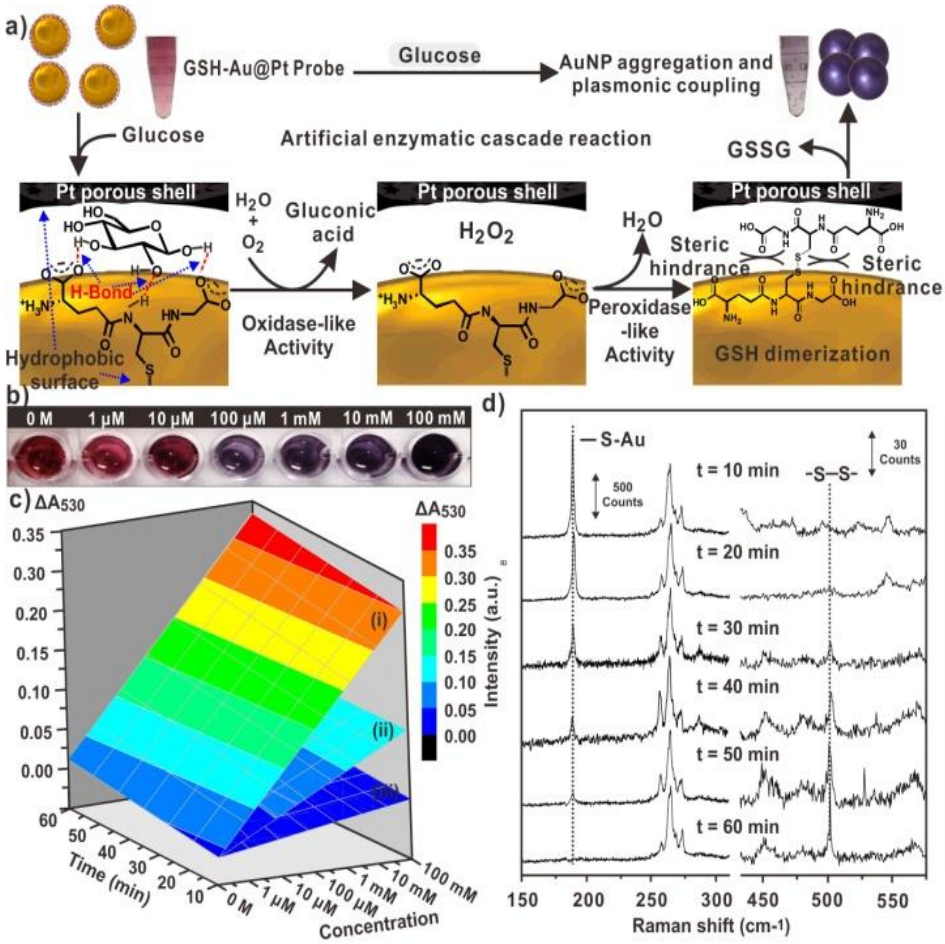

Figure 4.4. Schematic representation for colorimetric detection of D-glucose using GSH-Au@Pt nanoprobe and mechanistic proposal for cascade enzyme-mimetic recognition and conversion of glucose to gluconic acid and H_2O_2 mediated dimerization of interfacial GSH ligands (a). Solution color images of the GSH-Au@Pt after addition of different concentrations of glucose (b). 3-D graphical representation for change in absorbance at 530 nm as the function of time and concentration of glucose (c). Raman spectra obtained from GSH-Au@Pt glucose (100 mM) assay mixture at different time interval.

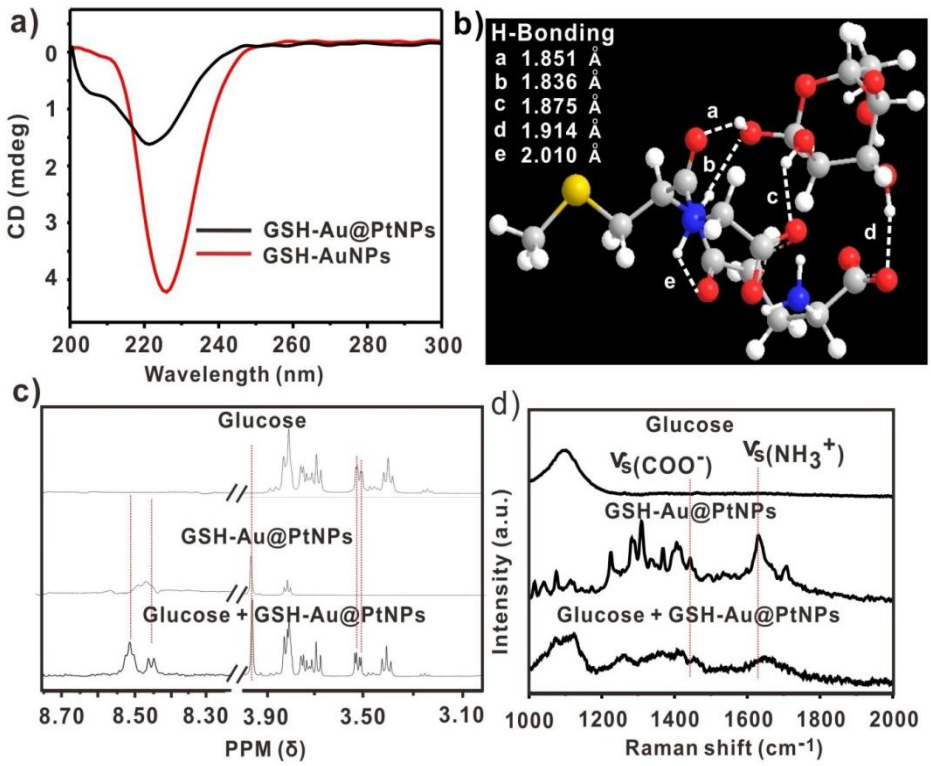

Figure 4.5. spectra of GSH-AuNPs and GSH-Au@Pt (a). Optimized minimum energy complex of S-methyl-GSH and D-glucose using DFT (B3LYP, 631-G) (b). 1H NMR spectra of D-glucose, GSH and equimolar mixture of D-glucose and GSH in D2O (c). Raman spectra of D-glucose, GSH-Au@Pt and mixture of D-glucose and GSH-Au@Pt (d).

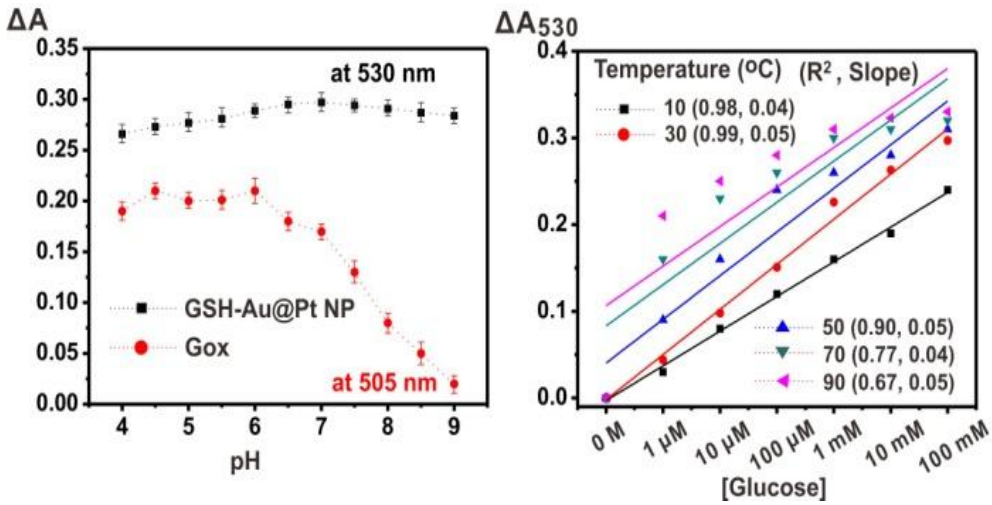

Figure 4.6. Performance of GSH-Au@Pt nanoprobe at different pH and temperature (a) Change in absorbance at 525 nm for GSH-Au@Pt and at 505 nm for GOx (in gluconic acid specific detection assay) in the presence of 100 mM glucose (b). Change in absorbance at 530 nm for GSH-Au@Pt nanoprobe at different temperatures in the presence of different concentrations of glucose.

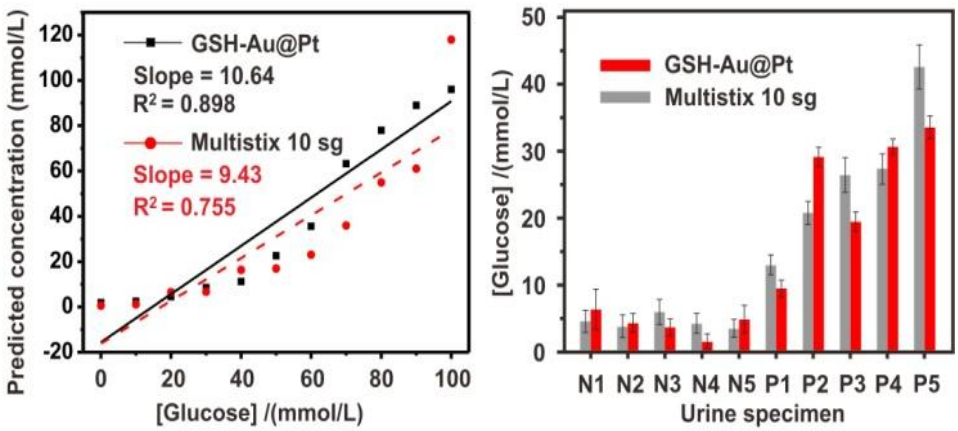

Figure 4.7. Performance of GSH-Au@Pt nanoprobe in comparison with commercial urinalysis platform (Multistix 10 SG by CLINITEK) using artificial urine samples having known concentrations of glucose (a). Measurement of glucose concentration in 10 real urine samples collected from 5 healthy persons and 5 diabetic patients using GSH-Au@Pt nanoprobe and commercial method.

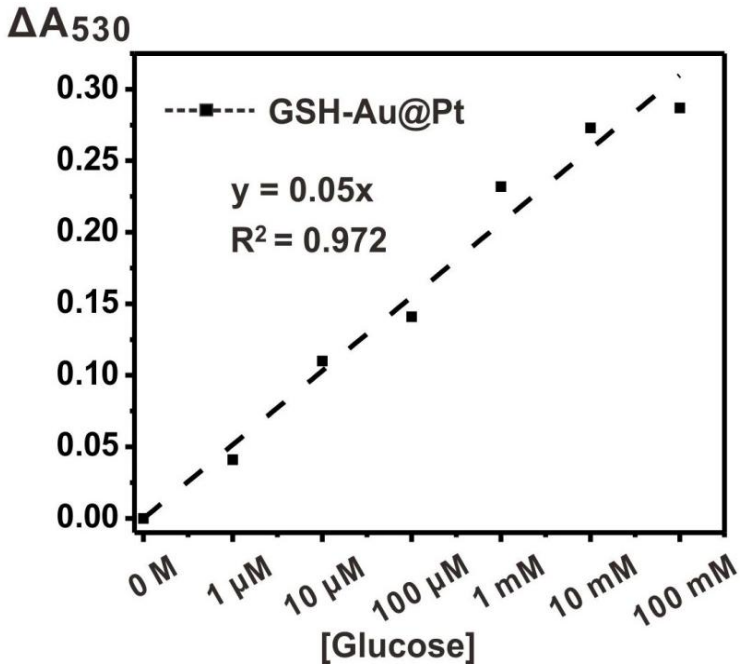

Figure 4.8. Calibration plot of GSH-Au@Pt UV/Vis spectroscopy response with different known concentrations of glucose in artificial urine.

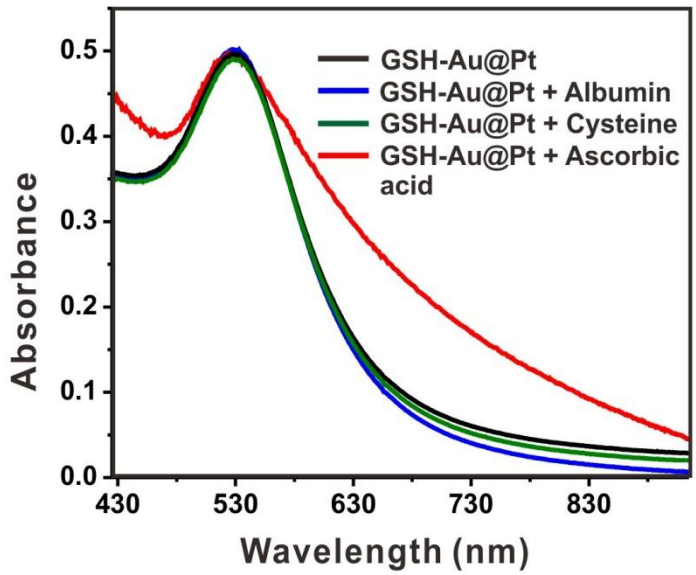

Figure 4.9. Comparison of UV/Vis spectra of GSH-Au@Pt after 2 hours of addition of albumin protein, cysteine and ascorbic acid showing inertness of GSH-Au@Pt towards these additives.

요약(국문초록)

제어 합성 및 바이오 센서, 바이오 이미징 및 플라즈몬 나노 - 바이오 하이브리드 프로브의 치료 응용 프로그램

나노물질 기반의 진단 및 치료 플랫폼은 적은 비용으로 높은 감도와 선택성을 제공한다는 면에서 기존의 시스템에 비해 상당한 이점을 제공해왔다. 다양한 나노물질 중에서도 금나노입자는 수많은 독특한 성질을 나타내는데 높은 표면적 비율, 작용기를 포함한 다양한 리간드를 이용한 표면개조의 용이성, 그리고 크기 및 모양에 따른 다양한 광학 및 전기적 성질 등을 예로 들 수 있다. 이러한 연유로 플라즈모닉 나노구조는 화학, 물리, 생명과학, 그리고 재료과학 분야를 포함한 다양한 과학 분야에서 각광받고 있다. 특히 생명의학 분야에 응용가능한 광학적 신호전달, 표면증강라만분석(SERS), 광촉매 및 광열 변환 등을 위해서는 플라즈모닉 나노구조의 획기적인 디자인과 합성 그리고 이들의 접목이 매우 중요하며, 이는 플라즈모닉 나노구조가 갖는 국부적 표면 플라즈몬 공명(LSPR) 특성에 기인한다. 지난 이십년간 나노과학의 놀라운 성장에도 불구하고 바이오센싱, 바이오이미징, 및 치료용 플라즈모닉 나노프로브가 실생활에 응용되지 못하고 있으며, 이는 생체적합성, 효율적인 나노-바이오 인터페이싱, 고감도 신호전달 반응과 같이 치료를 위해 해결되어야 할 중요한 과제들에 직면하고 있기 때문이다.

본 학위 논문에서는 조절가능한 광학적 특성 및 SERS, 광촉매 및 광열 특성을 보이는 새로운 나노플라즈모닉 나노구조/나노어셈블리를 고안하고 합성하였다. 우리의 새로운 나노바이오가 접목된 프로브는 정상세포와 암세포를 선택적이고 정량적으로 고감도 구분이 가능하도록 할 뿐만 아니라, 이 프로브는 활성산소와 활성질소로 인해 세포에 미치는 영향을 광학 및 SERS 를 통한 관찰 및 이미징이 가능하도록하며, 유기물질인 감광제 없이도 광열/광역학적 효과를

모두 나타내어 암세포 파괴가 가능하다. 더불어 임상적인 소변 검사를 통한 단당류인 포도당 검출에도 응용 가능하다.

활성산소종과 활성질소종은 화학적으로 반응성이 좋은 중간산물로서 복합적인 세포내 혹은 세포 외적 생화학적 반응으로 인하여 자연적으로 생체에서 생산되는 물질이다. 소위 산화적 스트레스의 상태라고 언급되는 활성산소종과 활성질소종의 과생산은 심장혈관계 질병, 암, 뇌신경 퇴행성 질병 등 많은 질병의 병리학적 주요 증상이라고 할 수 있다. 제 1 장에서는, 다양한 활성산소종과 활성질소종의 비색 및 분광학적 검지를 통한 고감도의 정확하고 정량적인 시험이 가능케 하는 glutathione 이 결합된 금나노입자(GSH-modified gold nanoparticles, GSH-AuNPs)에 대해 소개한다. 기본적인 원리는 다음과 같다. 활성산소종과 활성질소종으로 인해 glutathione 의 이황화결합이 형성되면 금나노입자 표면에 부착된 Glutathione 이 떨어져 나오게 되고, 따라서 불안정해진 금나노입자는 집합체를 형성하게 된다. 이런 금나노입자 집합체는 플라즈모닉 금나노입자가 플라즈모닉 커플링을 발생시켜 자외선-가시광선 분광스펙트럼에서의 적색 편이 및 용액의 색 변화를 유도한다. 비라디칼종인 과산화수소의 경우, Fenton 반응을 통해 과산화수소를 라디칼종으로 변화시켜 같은 방법으로 검지 가능하다. 활성산소종과 활성질소종 생산을 기반으로 한 암세포와 정상 세포의 빠르고 정량적인 구별이 가능할 것이다.

살아있는 세포에서의 활성산소종과 활성질소종의 정량적인 구별이 동시 가능한 모니터링은 자립적이고 상호독립적인 생물학적인 역할을 이해하는 데 매우 중요하며 생물학적 신호전달에 대한 기계적인 퍼즐을 푸는 데에 기여하게 될 것이다. 제 2 장에서는 플라즈모닉 '코어-위성' 나노어셈블리 바이오프로브를 통해 SERS 기반 살아있는 세포 내에서 발생하는 일산화질소와 과산화수소의 정량적인 다중 모니터링에 대해 소개한다. 이를 위해 금 코어-위성 나노어셈블리의 전자기적 'hot-zone' 에 polydopamine 을 계면 spacer 로 이용하여 이중 반응성의 라만 전달체인 myoglobin 을 접합시켰다. SERS 바이오프로브의 라만 신호전달체 헴-보철 그룹의 구조변화를 통해

활성산소종과 활성질소종을 검지하도록 한다. 암세포 및 살아있는 정상 세포의 세포 내 과산화수소와 일산화질소의 반응을 통해 SERS 를 측정하여 정확한 정량적인 모니터링이 가능케 하였다.

플라즈모닉 증강효과를 갖는 광학적 특성, 넓은 표면적, 촉매제의 기판 혹은 검지 프로브 및 나노수준의 장치의 기판으로서의 응용 가능성으로 인하여 표면이 울퉁불퉁한 형태의 금속 나노구조체는 매우 흥미있고 유용한 새로운 나노물질로 떠오르고 있다. 특히, 표면 플라즈몬 기반 광유도 치료효과 및 촉매는 나노구조체의 표면의 영향을 많이 받으나, 이러한 표면의 특성을 조절하는 것은 쉽지 않다. 제 3 장에서는 표면의 거칠기가 매우 높은 플라즈모닉 코어를 갖는 꽃잎 나노구조체(Core-petal nanostructures, CPNs)를 합성에 대해 소개한다. 구형의 금나노입자를 둘러싼 polydopamine 코로나를 $AuCl_4$ 로 유도한 산화적으로 분해함으로서 금나노꽃의 비등방성 성장을 통해 CPN 의 정교한 나노구조 조절이 가능하다. CPN 을 이용하여 광동역학적 효과와 광열적 효과를 모두 발생시켜 활성산소종이 발생하게 되고, 근적외선 영역의 빛을 조사하였을 때 플라즈몬 고열효과와 활성산소종으로 인한 세포내 손상의 시너지 효과에 기인하여 암세포의 효과적인 파괴를 유도한다. 또한, CPN 은 매우 강한 SERS 신호를 내보내며 이는 암세포 자살에 영향을 끼치는 DNA 구조변화에 대한 사후 측정을 가능하게 한다.

효소모방 메커니즘으로 작용하는 하이브리드 나노바이오센서는 자연적인 시스템과 인위적인 시스템을 통틀어 복합적인 최상의 특징을 갖는 것으로 받아들여지고 있다. 제 4 장에서는 세 가지 물질이 복합된 효소 모방형 GSH-Au@Pt 코어-쉘 나노프로브를 개발하고 이를 이용해 포도당의 검지 및 비색적인 방법을 통한 시그널링에 대해 설명한다. 자연에 존재하는 효소를 기반으로 한 기존의 포도당 센서와 달리, 우리의 나노프로브는 넓은 pH 범위에서 사용 가능할 뿐만 아니라 고온에서도 활용 가능하다는 장점을 갖는다. 생체모방 측면에서, 금으로 된 코어와 백금으로 이루어진 껍질 사이의

나노주머니는 glutathione 과 계면을 이루게 되는데, 이는 핵자기공명 분광학과 DFT 계산을 통한 결과 주체 당분자들의 효율적인 검지가 이루어질 수 있도록 최적화된 소수성 결합 및 수소결합 환경을 제공하는 것으로 나타난다. GSH-Au@Pt 나노프로브는 포도당의 산화작용에 촉매제로 작용하여 높은 효율성을 나타내며, 산화반응의 산물로 글루콘산과 과산화수소가 생성된다. 생성물인 과산화수소는 계면에 위치한 glutathione 의 이합화를 촉진하게 되고, 나노프로브가 모이면서 코어물질인 금나노입자의 플라즈모닉 커플링이 유도되어 가시적인 색 변화가 나타나게 된다. 따라서, 당뇨병 환자로부터 채취한 소변 샘플의 임상 테스트를 통해 놓은 정확도의 포도당 검지가 가능할 것이며, 정확한 포도당 검지에 방해를 하는 시스테인이나 아스토르브산, 단백질 등과 같은 소변 구성성분으로 인한 오진단 또한 거의 발생하지 않게 된다.

Key words: 플라즈모닉 센서, 비색적 센서, 표면증강라만산란(SERS), 바이오이미징, 바이오센싱, 활성산소종, 활성질소종, 산화적 스트레스, 암 진단, 코어-쉘, 효소 모방형, 광열 치료, 광역학적 치료, 코어-위성체, 플라즈모닉 집합체, Branched 나노구조체, polydopamine, glutathione, 포도당 검지, 소변 검사

학 번 : 2008-31095